INVESTIGATION OF THE EFFECT OF BENDING TWISTING COUPLING ON THE LOADS IN WIND TURBINES WITH SUPERELEMENT BLADE DEFINITION

A THESIS SUBMITTED TO
THE GRADUATE SCHOOL OF NATURAL AND APPLIED SCIENCES
OF
MIDDLE EAST TECHNICAL UNIVERSITY

BY

MEHMET OZAN GÖZCÜ

IN PARTIAL FULFILLMENT OF THE REQUIREMENTS
FOR
THE DEGREE OF MASTER OF SCIENCE
IN
AEROSPACE ENGINEERING

JULY 2014

Approval of the thesis:

INVESTIGATION OF THE EFFECT OF BENDING TWISTING COUPLING ON THE LOADS IN WIND TURBINES WITH SUPERELEMENT BLADE DEFINITION

submitted by **MEHMET OZAN GÖZCÜ** in partial fulfillment of the requirements for the degree of **Master of Science in Aerospace Engineering Department, Middle East Technical University** by,

Prof. Dr. Canan Özgen _____
Dean, Graduate School of **Natural and Applied Sciences**

Prof. Dr. Ozan Tekinalp _____
Head of Department, **Aerospace Engineering**

Prof. Dr. Altan Kayran _____
Supervisor, **Aerospace Engineering Dept., METU**

Examining Committee Members:

Assoc. Prof. Dr. Demirkan Çöker
Aerospace Engineering Dept., METU _____

Prof. Dr. Altan Kayran
Aerospace Engineering Dept., METU _____

Assist. Prof. Dr. Nilay Uzol
Turkish Aerospace Industries, Inc. _____

Assist. Prof. Dr. Ercan Gürses
Aerospace Engineering Dept., METU _____

Assist. Prof. Dr. Ali Türker Kutay
Aerospace Engineering Dept., METU _____

Date: _____

I hereby declare that all information in this document has been obtained and presented in accordance with academic rules and ethical conduct. I also declare that, as required by these rules and conduct, I have fully cited and referenced all material and results that are not original to this work.

Name, Last Name: MEHMET OZAN GÖZCÜ

Signature :

ABSTRACT

INVESTIGATION OF THE EFFECT OF BENDING TWISTING COUPLING ON THE LOADS IN WIND TURBINES WITH SUPERELEMENT BLADE DEFINITION

Gözcü, Mehmet Ozan
M.S., Department of Aerospace Engineering
Supervisor : Prof. Dr. Altan Kayran

July 2014, 121 pages

In this thesis study, the effect of off-axis plies in the spar caps of a wind turbine blade on the damage equivalent loads in a wind turbine system is investigated. The off-axis plies in the spar caps are exploited for load alleviation in the whole turbine system since the off-axis plies induced bending-twisting coupling into blades of wind turbine. Damage equivalent load is used to assess the effect of bend twist coupled blade on the fatigue load reduction in the whole wind turbine system. NREL's 5 MW turbine is selected as reference wind turbine system. In the initial phase of the thesis, since the sectional beam properties of reference turbine blades are known, the reference blades are utilized in a 3D inverse design process, and an inverse designed reference blade is obtained such that sectional beam properties of the 3D inverse blade design approximately match the sectional beam properties of NREL's reference turbine blade. In order to appropriately account for the effect of off-axis plies on the bending-

twisting coupling potential, dynamic super element of the blade is generated and imported into the multi-body dynamic model of the wind turbine system. Before using super element models of bend twist coupled blades, a comparative study is conducted by using super element blades and blades modelled as non-linear beam. Results show the appropriateness of the use of super element blades for transient aero-elastic analysis of the wind turbine system. The multi body dynamic model of the reference wind turbine system is created in Samcef Wind Turbine for transient aero-elastic analysis. The analysis of the wind turbine systems are performed for the power production case with constant wind load case and normal turbulent wind load case. Damage equivalent loads at critical monitor points are calculated by time history results of the analysis. Conclusions are inferred with regard to the effectiveness of the off-axis spar cap plies with different flapwise stiffness values of the blade structure in load alleviation and possible drawbacks of the use of off-axis plies in the spar caps. Results show that in the overall, with the use of off-axis plies in the main spar caps of the blade, damage equivalent loads associated with the critical force or moment components can be reduced in the wind turbine system.

Keywords: Wind turbine loads, Aeroelasticity, Bending twisting coupling, Damage equivalent load, Superelement, Composite Blade, VABS, Samcef Wind Turbine

ÖZ

BURULMA BÜKÜLME ETKİLEŞİMİNİN RÜGAR TÜRBİNİ YÜKLERİ ÜZERİNDEKİ ETKİSİNİN SÜPER ELEMAN KANAT KULLANILARAK İNCELENMESİ

Gözcü, Mehmet Ozan
Yüksek Lisans, Havacılık ve Uzay Mühendisliği Bölümü
Tez Yöneticisi : Prof. Dr. Altan Kayran

Temmuz 2014 , 121 sayfa

Bu tez çalışmasında, rüzgar türbin kanat kirişlerinin arasındaki flanş bölgelerinde kullanılan kompozit katmanların kanat eksenine göre açılı yerleştirilmelerinin, rüzgar türbin sistemindeki yorulma hasarına eşdeğer yüklerine olan etkisi incelenmiştir. Kanat kirişlerindeki açılı kompozit katmanlar tüm türbin sisteminde yük azaltılması için kullanılmıştır, çünkü açılı kompozit katmanlar rüzgar türbini kanatlarında eğilme-burulma etkileşimi yaratmaktadır. Tüm rüzgar türbini sisteminde eğilme burulma etkileşiminden kaynaklı yorulma yükü azalmasını değerlendirmek için hasar eşdeğer yükler kullanılmıştır. NREL'in 5 MW'lık türbini referans türbin olarak seçilmiştir. Tezin ilk fazında, referans türbin kanatlarının kiriş kesit özellikleri bilindiğinden, referans kanatlar üç boyutlu tersine bir tasarım işlemi için kullanılmış ve kesit kiriş özellikleri NREL'in referans kanadınkilere benzer olan üç boyulu bir tersine referans kanat tasarımı elde edilmiştir. Kanat eksenine göre açılı kompozit katmanların eğilme burulma etkileşmi po-

tansiyeline etkisini doğru bir şekilde değerlendirmek için, kanadın dinamik süper eleman modeli oluşturulmuş ve rüzgar türbin sisteminin çoklu kütleli dinamik modeline aktarılmıştır. Eğilme burulma etkileşimli kanatlarda süper eleman modelini kullanmadan önce, süper eleman kanatlar ve doğrusal olmayan kiriş olarak modellenen kanatlar kullanılarak karşılaştırmalı bir çalışma yapılmıştır. Çıktılar, süper elaman kanatların, rüzgar türbini sistemlerinin zamana bağlı aero-elastik analizlerinde kullanılmasının uygunluğunu göstermiştir. Referans türbin sisteminin çoklu kütleli dinamik modeli, zamana bağlı aero-elastik analizler için Samcef Wind Turbine ortamında yaratılmıştır. Rüzgar türbini sisteminin analizleri, güç üretimi durumunda sabit rüzgar ve normal türbülanslı rüzgar yük durumları için yapılmıştır. Kritik monitör noktalarındaki hasar eşdeğer yükler zamana bağlı analiz çıktılar kullanılarak hesaplanmıştır. Sonuçlar kanat eksenine göre açılı kompozit katmanların, farklı kelebekleme yönü rijitlik değerleri ile kanat yapılarında yük azalmasındaki etkinliliği ve açılı kompozit katman kullanımının olası dezavantajları açısından ele alınmıştır. Çıktılar genel olarak, kanat eksenine göre açılı kompozit katmanların kanat kirişlerinin arasındaki flanş bölgesinde kullanılmaları ile rüzgar türbini sistemindeki kritik yük ya da moment bileşenlerinin hasar eşdeğer yüklerinde azalma olduğunu göstermiştir.

Anahtar Kelimeler: Rüzgar türbini yükleri, Aero-elastisite, Bükülme burulma etkileşimi, Hasar eşiti yük, Süper-eleman, Kompozit Pala, VABS, Samcef Wind Turbine

Bu tez çalışmamı, insan olarak yaşama mücadelesindekilere adıyorum.

ACKNOWLEDGEMENTS

I would like to thank my supervisor Professor Altan Kayran for his constant support, guidance and friendship. It was a great honour to work with him for the last three years and our cooperation influenced my academical and engineering view highly. He also motivated and influenced me highly in scientific context.I also would like to thank Roman Braun for his support and guidance on my internship at Fraunhofer IWES. While my internship, the big initial step of the thesis was completed by his support.

A lot of people influenced and supported this work scientifically and their contribution were valuable for me. Mehmet Harun Özkanaktı is specially acknowledged for his contribution about 3D blade geometry drawings in Catia. I also appreciate my officemates from MetuWind: Bayram Mercan, Başak Zeka, Gökhan Ahmet, Touraj Fasadi and Serpil Selvi. I would like to thank my office mates during the internship in Fraunhofer IWES:Neelabh Gupta, Oliver Kranke. I also would like to acknowledge Alexandros Antoniou from Fraunhofer IWES for his advises about scientific world.

I would like to thank to all of my professors from METU. My professors Demirkan Çöker and Oğuz Uzol are specially acknowledged for their positive attitude to me in MetuWind and their support. I also would like to acknowledge to Assistant Professor Ercan Gürses for his good attitude and interest to my thesis.

I have many friends who are influenced my character and point of view from my childhood to today. I thank to all of my friends in my life but I would like to thank specially some of them: Pelin Ergen, Emre Yılmaz, Mehmet Harun Özkanaktı, Cemal İlhan, Uğur Bircan, Şerif Ertürk, Özlem İnci.

My family is the real reason to stay on my feet in the life. Although their intelligence, courage and determination are not fully transmitted to me, I obtained

enough amount of skills from them to believe my-self to be. I sincerely appreciate my mother Fatma Gözcü, my father İsmail Gözcü and my brother Oğuz Gözcü. There are also two valuable persons from my childhood to today, my grandmother Hatice Taşçıoğlu and my grandfather Mehmet Taşçıoğlu (Diken Mehmet). I have not been alone in Ankara for last six years and I sincerely acknowledge Pelin Ergen. I believe she will be a part of my family.

This work is also supported by MetuWind (Middle East Technical University Center for Wind Energy) which I am honoured to be a part of it.

TABLE OF CONTENTS

ABSTRACT v

ÖZ vii

ACKNOWLEDGEMENTS x

TABLE OF CONTENTS xii

LIST OF TABLES xv

LIST OF FIGURES xvii

LIST OF ABBREVIATIONS xxii

CHAPTERS

1 INTRODUCTION 1

1.1 Sustainable Energy and Wind Energy 1

1.2 Wind Turbines 2

1.3 Literature Survey on Aeroelastic Tailoring of Wind Turbine Blades 4

1.4 Scope of the Thesis 6

2 INVERSE DESIGN OF NREL 5 MW BLADE 11

2.1 Blade Geometry 12

2.2 Initial Spar Cap Design 15

2.3 Calculation of Extreme Operating Gust Wind 16

2.4 Calculation of Section Moment Loads by FAST 19

2.5 Stress Calculation and Failure Check 21

2.6 Results of Initial Spar Cap Design 25

2.6.1 All Glass Fiber/Epoxy Composite Spar Cap Design 25

2.6.2 Hybrid Glass Fiber/Epoxy Carbon Fiber/Epoxy Composite Spar Cap Design 26

2.6.3 All Carbon Fiber/Epoxy Composite Spar Cap Design 27
2.7 Inverse Design Methodology of the NREL Blade 29
2.7.1 VABS 30
2.7.2 Full Material Definition of Cross-Section 31
2.7.3 Inverse Design Results 33
3 SUPERELEMENT MODEL 41
3.1 Theory of Craig-Bampton Method 42
3.2 Finite Element Model of the Blade 46
3.2.1 Superelement Blade Verification 52
4 MULTIBODY SIMULATION OF THE WIND TURBINE SYSTEM AND CALCULATION OF DAMAGE EQUIVALENT LOADS 57
4.1 General Properties of Wind Turbine Model 58
4.1.1 Wind Turbine Blades 59
4.1.2 External PID Controller 64
4.1.3 Drive Train 66
4.1.4 Monitor Points on the Wind Turbine 71
4.1.5 Load Cases 71
4.1.6 Damage Equivalent Load 74
5 RESULTS 75
5.1 Constant Wind Results 76
5.1.1 Comparative study of wind turbine simulation with superelement blades and geometrically nonlinear beam blades 76
5.1.2 Effect of Off Spar Cap Plies On the Load Alleviation in the Wind Turbine System 78
5.2 Turbulent Wind Results 83
5.2.1 Results for Wind Turbine System with 15 Degree Off-Axis GFRP Spar Cap Plies 84
5.2.2 Results for Wind Turbine System with 15 Degree Off-Axis CFRP Spar cap Plies 95
5.2.3 Results for Wind Turbine System with Mixed 0 Degree and 15 Degree Off-Axis GFRP Spar cap Plies 99

5.2.4 Results for Wind Turbine System with Stiff CFRP Blades 101

6 CONCLUSION 105

REFERENCES 111

APPENDICES

A TRANSITION AIRFOILS 115

B DAMAGE EQUIVALENT LOAD 119

C SAMCEF WIND TURBINE VERIFICATION 121

LIST OF TABLES

TABLES

Table 2.1 Airfoil distribution of the NREL's 5 MW wind turbine blade . 14
Table 2.2 General Properties of the wind turbine defined in FAST . . . 19
Table 2.3 Comparision of analytical results and code results 23
Table 2.4 Material properties of GFRP and CFRP composite plies which are used in blade structure 24
Table 2.5 Example line of the input file which describes the spar cap regions by their chordwise locations 25
Table 2.6 Comparison of sectional bending and torsional stiffness values of the inverse designed and the NREL blade 34
Table 2.7 Inverse design ply numbers between section 2 - 17 39
Table 2.8 Modified inverse design ply numbers between section 2 - 17 . . 39

Table 3.1 Comparison of first five frequencies of the turbine blade clamped at the root 53

Table 4.1 Main properties of the wind turbine system defined in SWT . 60
Table 4.2 Blade configurations used in the analyses, first one is beam model and others are superelement models 61
Table 4.3 Flapwise stiffness values $[Nm^2]$ of the tip sections of the blades 63
Table 4.4 Bending twisting coupling values $[Nm^2]$ of the tip sections of the blades 63
Table 4.5 Gear ratio of the three stages of the gearbox 69

Table 5.1 Comparison of average and damage equivalent loads at blade-hub link node 77
Table 5.2 Damage equivalent load results of zero degree and fifteen degree GFRP configurations with different m values 81

Table 5.3 Damage equivalent blade root moments calculated for the turbulent wind load case 85
Table 5.4 Damage equivalent bedplate-tower link forces calculated for the turbulent wind load case 89
Table 5.5 Damage equivalent load results of zero degree and fifteen degree GFRP configurations with different m values 89
Table 5.6 Damage equivalent main shaft-bedplate connection forces at main bearing loacations 1 and 2 91
Table 5.7 Damage equivalent forces and moments at the main shaft-gearbox connection point 93
Table 5.8 Maximum, minimum peak and average values of X moment . 93
Table 5.9 Damage equivalent shear forces at the planet carrier bearings of stages 1 and 2 95
Table 5.10 Damage equivalent load results of zero degree, fifteen degree GFRP and fifteen degree CFRP configurations 97
Table 5.11 Ratio of damage equivalent load results fifteen degree GFRP and fifteen degree CFRP configurations to zero degree GFRP configuration 98
Table 5.12 Comparison of the ratio of damage equivalent loads of GFRP blades with 15^0 spar cap ply 100
Table 5.13 Comparison of the ratio of damage equivalent loads of GFRP blades with 15^0 spar cap ply 103

Table A.1 First transition airfoil coordinates 116
Table A.2 Second transition airfoil coordinates 117

Table C.1 Integrated rotor torque [N.m], power [W] and power coefficient [-] in both models 121

LIST OF FIGURES

FIGURES

Figure 1.1 Projected utility generation resources in 2015, relative cost and relative risk [8] 2
Figure 1.2 General view of horizontal axis wind turbine (left) and vertical axis wind turbine (right) [42] 3
Figure 1.3 Flow chart of the thesis which shows the main design and analysis steps 9

Figure 2.1 Thickness to chord ratio of the blade geometry 14
Figure 2.2 Up view of the blade geometry. Maximum thickness location is tried to be located near to the shear webs (spar locations) 15
Figure 2.3 Spar cap regions and projections of them on the chordwise locations of an airfoil section 15
Figure 2.4 Spar cap regions shown on 3D blade geometry, green region is middle spar caps, orange region is trailing edge spar caps and blue region is leading edge spar caps 16
Figure 2.5 Wind Velocity vs. Time for gust wind with $V_{hub} = 11.4\ m/s$. 18
Figure 2.6 Wind Velocity vs. Time for gust wind with $V_{hub} = 25\ m/s$ . . 18
Figure 2.7 Moment load distribution of the blades when maximum flapwise moment occurs 20
Figure 2.8 Moment load distribution of the blades when minimum flapwise moment occurs 20
Figure 2.9 Moment load distribution of the blades when maximum edgewise moment occurs 21
Figure 2.10 Moment load distribution of the blades when minimum edgewise moment occurs 21
Figure 2.11 Stress exposure results of GFRP spar cap design 26

Figure 2.12 Stress exposure results of mix (GFRP and CFRP) spar cap design 27
Figure 2.13 Stress exposure results of CFRP spar cap design 28
Figure 2.14 Sectional weights of three initial spar cap designs between section 4-17 28
Figure 2.15 Three dimensional design loop of a wind turbine blade with known cross-sectional beam properties 30
Figure 2.16 Calculation of the beam cross sectional properties using PreVABS and VABS 30
Figure 2.17 PreVABS mesh at a leading edge of a cross section, between shear web and spar cap, on whole cross section and at the trailing edge 32
Figure 2.18 Variation of the flapwise bending stiffness of the inverse designed blade and NREL blade between section 1 - 17 35
Figure 2.19 Variation of the flapwise bending stiffness of the inverse designed blade and NREL blade between section 9 - 17 35
Figure 2.20 Variation of the edgewise bending stiffness of the inverse designed blade and NREL blade between section 1 - 17 36
Figure 2.21 Variation of the edgewise bending stiffness of the inverse designed blade and NREL blade between section 9 - 17 36
Figure 2.22 Variation of the torsional stiffness of the inverse designed blade and NREL blade between section 1 - 17 37
Figure 2.23 Variation of the torsional stiffness of the inverse designed blade and NREL blade between bection 9 - 17 37
Figure 2.24 Variation of the torsional stiffness value of section 16 with the number of plies in the leading and trailing edge spar caps 38

Figure 3.1 Blade coordinate system defined in Samcef, y axis is along the chord, z axis is along the span 47
Figure 3.2 3D blade model in Samcef Field with highlighted middle spar-cap region 48
Figure 3.3 Definition of the properties of the GF composite material in Samcef Field 48
Figure 3.4 Layer definition of the root section of the blade in Samcef Field 49

Figure 3.5 The normal of the surfaces have to be towards inside of the blade for a correct stacking sequence 49
Figure 3.6 Spanwise locations of the retained nodes on the blade FE model 50
Figure 3.7 Generation of the dynamic superelement of the wind turbine blade **(a)** CAD model of the blade and generation of retained nodes **(b)** Assigning composite material to the faces of the blade **(c)** Connection of the retained node to faces of the related blade section by mean elements **(d)** Finite element mesh of the blade structure . . . 51
Figure 3.8 Global view of the blade structure with fine mesh 53
Figure 3.9 Fine mesh view from the root of the blade with mesh on the shear web structures 54
Figure 3.10 Fine mesh view on the spar cap region of the blade 55
Figure 3.11 First five mode shapes of the blade which are calculated for comparison of different mesh sizes 55

Figure 4.1 Global coordinate system used in wind turbine analysis . . . 59
Figure 4.2 Tower coordinate system used in wind turbine analysis . . . 59
Figure 4.3 Spar cap regions of the blades with off-axis plies 64
Figure 4.4 (a)Global view of wind turbine system (b)Tilt angle of rotor (c) Prebet of the blades 64
Figure 4.5 A simple PID scheme 65
Figure 4.6 Location of drive train components on the wind turbine system 67
Figure 4.7 Rotor shaft bearing locations on the wind turbine system . . 67
Figure 4.8 Three stages of the gearbox, yellow part is the helical stage and green parts are the planetary stages 68
Figure 4.9 Planet carrier bearings of the gearbox 68
Figure 4.10 Standard high speed coupling shaft of the wind turbine system 69
Figure 4.11 Standard tower model in SWT 70
Figure 4.12 Power production load case selection in SWT 72
Figure 4.13 Constant wind load case generation in SWT 72
Figure 4.14 Turbulent wind type selection in Turbsim meteorological boundary conditions tab 73
Figure 4.15 Seed definition in the run time options tab 73

Figure 4.16 Grid definition of TurbSim turbine/model specification tab . 73

Figure 5.1 Comparison of peak axial displacements towards downwind . 78

Figure 5.2 Comparison of sectional lift forces of zero and fifteen degree GFRP spar cap configurations 79

Figure 5.3 Flapwise root moment of blade 1 of zero degree GFRP spar cap configuration 79

Figure 5.4 Flapwise root moment of blade 1 of fifteen degree GFRP spar cap configuration 80

Figure 5.5 Generator power output of zero degree GFRP spar cap configuration 81

Figure 5.6 Generator power output of fifteen degree GFRP spar cap configuration 82

Figure 5.7 Blade tip displacement of zero degree GFRP spar cap configuration 82

Figure 5.8 Blade tip displacement of fifteen degree GFRP spar cap configuration 83

Figure 5.9 Flapwise root moment of blade 1 of zero degree GFRP spar cap configuration 84

Figure 5.10 Flapwise root moment of blade 1 of fifteen degree GFRP spar cap configuration 84

Figure 5.11 Tip displacement of zero degree GFRP spar cap configuration 86

Figure 5.12 Tip displacement of fifteen degree GRPF spar cap configuration 86

Figure 5.13 Generator power output of zero degree GFRP spar cap configuration 87

Figure 5.14 Generator power output of fifteen degree GFRP spar cap configuration 87

Figure 5.15 X , Y and Z forces acting on the bedplate-tower link for the wind turbine with blades having zero degree spar cap plies 88

Figure 5.16 X, Y and Z moments acting on the bedplate-tower link for the wind turbine with blades having 0 degree spar cap plies 90

Figure 5.17 Main shaft-bedplate connections: Main bearings 1 and 2 . . . 91

Figure 5.18 Main shaft-gearbox connection point shown in the wind turbine system 92
Figure 5.19 X moment acting on the center of the rotor hub wind turbine; blades with 0 degree spar cap plies 94
Figure 5.20 X moment acting on the center of the rotor hub wind turbine; blades with 15 degree GFRP spar cap plies 94
Figure 5.21 Two stage planetary, one stage parallel gear box 95
Figure 5.22 Blade tip displacement of CFRP spar cap configuration . . . 99
Figure 5.23 Blade tip displacement of GFRP spar cap %12 configuration 101
Figure 5.24 Blade tip displacement of GFRP spar cap %18 configuration 101
Figure 5.25 Blade tip displacement of stiff CFRP spar cap configuration . 102

LIST OF ABBREVIATIONS

1D	One Dimensional
2D	Two Dimensional
3D	Three Dimensional
BEM	Blade Element Momentum
CF	Carbon Fiber
CFRP	Carbon Fiber Reinforced Plastic
DEL	Damage Equivalent Load
fe	Stress Exposure Factor
FF	Fiber Failure
GF	Glass Fiber
GFRP	Glass Fiber Reinforced Plastic
GL	Germanischer Lloyd
IEC	International Electrotechnical Commission
IFF	Inter Fiber Failure
MW	MegaWatt
NREL	National Renewable Energy Laboratory
PHATAS	Program for Horizontal Axis Wind Turbine Analysis and Simulation
PID	Proportional-Integral-Derivative Controller
PreVABS	Preprocessor for VABS Modeling of Sophisticated Cross-Sections
rpm	Revolution per Minute
SE	Super-element
SWT	Samcef Wind Turbine
UD	Unidirectional Fabric
VABS	Variational Asymptotical Beam Sectional Analysis
VAM	Variational Asymptotic Method
WT	Wind Turbine

CHAPTER 1

INTRODUCTION

1.1 Sustainable Energy and Wind Energy

In the World, energy demand is exponentially increasing and the effort of engineers to meet this demand mostly depended on the fossil fuel. In fact, there are two main energy sources for our old world; sun and the energy stored in the hot core of the earth. In the last twenty years, mankind has learnt how to harvest the energy of sun effectively. The photovoltaic panel is a direct solution to capture the energy of sun; however as of today, the efficiency of this technology is at low level. On the other hand, wind turbines harvest the kinetic energy of wind which is a form of the sun energy. The efficiency of wind turbines is much higher than the efficiency of photovoltaic panels. It is also possible to build wind turbines on land (onshore configuration) or over the sea (off-shore configuration). Therefore, the wind energy is the number one sustainable energy type today. Countries require sustainable, independent and cheap energy solutions for the future. Specially, western countries and China have very ambitious goals about the wind energy. For instance, United States is aiming to produce 20% of its electricity by wind turbines. Figure 1.1 shows why wind energy is so popular.

Although, wind turbines have been used for over three thousand years, until the past decades they did not capture the interest of politicians, businesses and consumers. In this period, the growth level of wind energy industry and the increase of electricity production of wind energy have reached top in the list of energy industry. In 1990, the average wind turbine that was installed was around 500

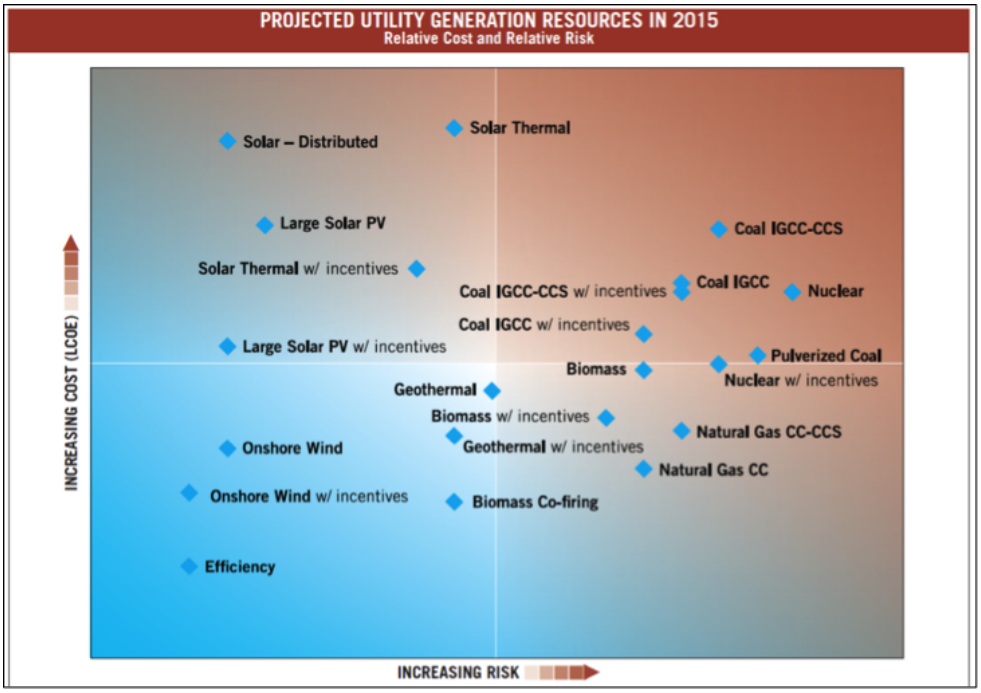

Figure 1.1: Projected utility generation resources in 2015, relative cost and relative risk [8]

kW [46], while currently the new wind turbines produce power as high as 7.5 MW. As a result of these political and technical decisions, new challenges have been appearing for engineers.

Wind turbines are the largest rotor structures in the world with exceeding 80 meter blade length. In near future, 100 meters long blades will be produced and used in wind turbines. Longer blades necessitate better optimized blade structures, which bring about challenges to the design process to develop innovative design solutions. In addition, the interaction between aerodynamic loads on the blade and blade structure (aeroelasticity) has become very crucial for large rotors.

1.2 Wind Turbines

Wind turbines are basically machines, which convert the kinetic energy of the wind to the useful mechanical energy. The history of wind turbines starts from ancient ages. In the ancient ages, the mechanical power of wind turbines was

used for grain grinding and water pump. On the other hand, today wind turbines generally have electric generator to convert the mechanical energy to the electrical energy.

There is a main classification of wind turbines that depends on the plane of the turbine's shaft axis according to wind direction. If the plane of the shaft axis is located horizontally with respect to the wind direction, then this type of wind turbine is called "horizontal axis wind turbine (HAWT)". If the shaft axis is placed vertically with respect to the wind direction, then it is called as "vertical axis wind turbine (VAWT)". Figure 1.2 shows the general view of the horizontal and the vertical axis wind turbines and their main components.

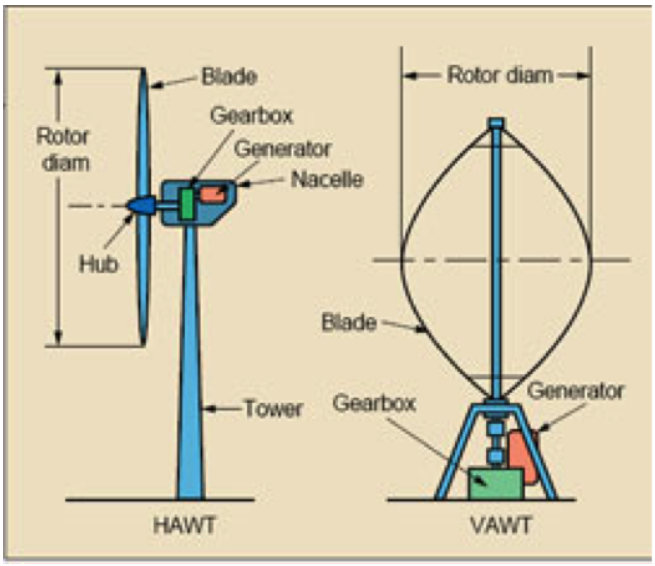

Figure 1.2: General view of horizontal axis wind turbine (left) and vertical axis wind turbine (right) [42]

Today, HAWTs are very popular due to their large power capacity. They are generally in the MW power level with the maximum power output being more than 7 MW. On the other hand, VAWTs have smaller power capacity compared to HAWTs. They are generally used for small-scale applications. They have better performance in turbulent wind and in low wind speeds compared to HAWTs. However VAWTs cannot be large as HAWTs because of the mechanical issues. Since horizontal axis wind turbines are mostly preferred in the commercial market and their power output is higher than the power output of vertical axis wind turbines, HAWTs are mostly the focus of wind energy researches. This thesis is

not an exception to the general research trend. Therefore, in the thesis, "wind turbine" means "horizontal axis wind turbine".

1.3 Literature Survey on Aeroelastic Tailoring of Wind Turbine Blades

Blades are responsible for the majority of the loads on the wind turbine systems. Although some part of these loads can be converted to electrical power, the rest of them are undesired loads. There is no way to control the atmospheric turbulence and gusts which are mostly responsible for fatigue and extreme loads. However, one can control the rotor blades by control surfacing (e.g. flaps, slats etc.) or by adjusting the pitch angle of the blades. These kinds of solutions need a feedback system and mechanical parts to move the control structures. On the other hand, one can design the blades by passive control features such as aeroelastic tailoring of the rotor blades.

Aeroelastic tailoring of the rotor blade is a passive load control mechanism which can be exploited in achieving load alleviation. Anisotropy offered by composite materials can be utilized such that aeroelastic twist induced due to bending during the operation of the wind turbine system can be alleviated, and this in turn may result in load alleviation in the entire turbine system.

Internal loads in the wind turbine system are dynamic in nature with the load cycles exceeding 10^8 in the life time of the turbine system. Therefore, especially for wind turbine systems, which have power output in the megawatt range, reducing the fatigue loads is very crucial to keep the turbine system operational for longer periods. Fatigue damage equivalent load is a sign of the degradation of the elements of the sub-structures of the wind turbine system due to material fatigue incurred under cyclic loading, and reduction in the damage equivalent loads implies increased fatigue life of the structural elements.

Bending-twisting coupling was proposed as a passive load control in wind turbines first by Karaolis [29]. After the initial work of Karaolis, exploiting bending-twisting coupling in composite blades in passive load control is considered as an alternative to the active load control strategies [37]. Although the study of Lobitz, Veers and their collegues [37] [36] [38] got important steps toward using

blade couplings for load reductions, the full potential of passive control of wind turbine blade is still to be explored. Bending- twisting coupling effects are considered to be implemented new beam models and further researches of passive load control methods depend on bending-twisting coupling can be done by fully coupled beam model [30]. In the report prepared by ECN, assessments have been made on how the bending-twisting coupling can be exploited in the wind turbine systems [31]. Finite element analysis of 9.2 m long wind turbine blades, manufactured by TPI Composites, has been performed to study the effect of using off-axis carbon plies in the spar caps of the blade by Sandia Laboratories [39]. In the report of the Sandia Laboratory, comparisons are also done with the base E-Glass blade in terms of bending and buckling loads as well as strain distribution. It has been demonstrated that with the use of off-axis carbon plies in the spar caps of the blade, similar structural behaviour as that of base E-Glass blades can be obtained but with an overall weight advantage. Another study from Sandia Laboratories was performed by Thomas D. Ashwill. He extended the research about passive load control by introducing beding twisting coupling to a 27 m STAR blade [4]. Goeji and his colleagues also create a FEM model of the wind turbine blade with off-axis plies [16]. In his study, the effective application regions of the off-axis plies on a cross-section are investigated and the results are compared to experimental results. He recommended further investigations of the fatigue properties of a glass/carbon hybrid FRP with off-axis fibre orientations. In the study of Lucas I. Lago [33], coupling between bending and twisting was suggested as the principle of adaptive blades, where the incremental loads are reduced as the blade bends.

The use of off-axis carbon plies in the spar caps of the blade has a similar effect on the structural behavior as that of the base E-Glass blade, but with an overall weight advantage. A wind turbine blade provided by Vestas has been modified with the placement of off-axis plies on the upper and lower skin of the blade, then static and dynamic characteristics of the blade obtained experimentally has been compared with the finite element results in the study of Luczak et al [40]. A reference blade is needed to study the effect of aeroelastic tailoring on blade structure and wind turbine system. NREL published a report in which beam properties of a 5 MW wind turbine blade is given. NREL's 5 MW wind turbine

blade is suitable for researchers to use it as a reference blade for their studies [27]. A sample study, which uses the blade of NREL's 5 MW wind turbine system as the baseline blade is given by Zhou et al [50]. In this study, it has been shown by finite element analysis that by using different composite material with different fiber orientations in the blades, bending-twisting coupling characteristics of the blade can be changed appreciably. A similar study is given by Lin and Lai [34]. The effect of bending-twisting coupling on the internal loads in the blades was investigated by Capellaro [11]. In his work, Capellaro used the 5 MW UpWind reference wind turbine as the baseline turbine which has been developed for research purposes [19]. The results of the study showed that with the bending-twisting coupling created by the use of off-axis plies in the spar caps of the wind turbine blade, reduction in the damage equivalent loads for the blade root bending and torsional moment is possible. It is important to note that, damage equivalent loads is used as a metric that indicates the fatigue related degradation of the material as a result of cyclic loading in his study [11]. A similar study was done by Aziz and his colleagues [5]. In their study, the process was started by a design of a baseline blade model. Then they conducted finite element analysis of the baseline blade and developed a hybrid blade design by replacing the glass fibers with carbon fibers in the spar cap regions. Lastly, they validated the feasibility of implementing bending-twisting coupling in the wind turbine blade by studying stresses, and strain behavior.

1.4 Scope of the Thesis

As the sample studies show, in the recent years, there has been increasing number of studies on exploiting the bending-twisting coupling in the wind turbine blades. However, most of the previous studies performed deal with effect of bending-twisting coupling on the loads acting on the blades rather than on the whole turbine system. Different from most of the work in the literature, in this thesis, in addition to the effect of bending twisting coupling on the external aerodynamic load, the effect of bending-twisting coupling, generated in the turbine blades on the internal loads, such as shear force and bending moment, in the

critical sub-structures of the whole wind turbine system is also investigated. For the purpose of the study, inverse design of a reference blade is performed such that sectional beam properties of the 3D blade design approximately match the sectional beam properties of NREL's 5MW turbine blade [27]. Sectional properties of the inverse designed blade are calculated by using PreVABS and VABS [14] [48] which uses on variational asymptotic beam theory. Then the 3D CAD view of the blade is created. In order to appropriately account for the bending-twisting coupling effect, dynamic superelement of the blade is created in Samcef Field [45] and introduced into the multi-body dynamic model of the wind turbine system that is generated in Samcef Wind Turbines (SWT) [2]. Dynamic superelement shows all coupling effects of the blades and is suggested in the study of [21] to capture the whole dynamic behavior of the blades. Since the blades are responsible for the majority of the loads, a good modeling of them is needed. To perform an analysis of whole system, all component properties of the wind turbine have to be defined. Again, the component properties of the NREL's 5 MW wind turbine are used for tower, bedplate, generator, gearbox, shaft and hub properties. In real time and real simulations, one needs a controller for wind turbine system. In the analysis, a PID controller is used. Since the analysis of the thesis does not include any emergency condition, the controller adjusts only the pitch angle of the blades. For all analyses, the controller and the components of the wind turbine system except the blades are same. Before the study of the effect of bending-twisting coupling on the loads acting on the wind turbine, a comparative study is conducted on the performance of wind turbines that have blades defined as superelements and geometrically nonlinear beams in SWT, and conclusions are inferred with regard to the appropriateness of the use of superelement blade definition in the transient analysis of the 5MW wind turbine system that is set up in the thesis. Multi-body dynamic simulations of the wind turbine system are performed for the power production load case with the constant wind, and the normal turbulence model as external wind loadings as specified in IEC 61400-1 [24]. Turbulent wind cases are created by using TurbSim [25] and the durations of the turbulent wind analysis which are used to calculate DEL are 600 seconds. On the other hand since the constant wind condition is a steady case, the duration of constant wind analysis are not

important if the results converge.

For the external loads, average values of the aerodynamic forces on the blades, which are determined through the unsteady blade element momentum method, are used for the assessment of the effect of bending-twisting coupling on the external load reduction. For the internal loads, fatigue damage equivalent load (DEL) (see Appendix B for definition) is used as the metric to assess the effect of bending-twisting coupling on the load alleviation in the whole wind turbine system. Time history results of aeroelastic simulations are used to calculate damage equivalent loads at the selected monitor points in the wind turbine system such as rotor-hub connection, main shaft bearings, low speed shaft-gear box connection point etc., and conclusions are inferred with regard to the effectiveness of the off-axis spar cap plies in the blade structure on the internal load alleviation. DEL are strongly related to the fluctuations of internal loads. Therefore, the strong correlation between fluctuation ranges (min and max values) of the load outputs on the monitor points and DEL is also investigated. The Figure 1.3 shows the processes of the thesis. It is a general flow chart and it does not show the details of the analysis steps.

Glass-fiber-reinforced-plastic (GFRP) and carbon-fiber-reinforced-plastic (CFRP) materials are used in off-axis configuration in the spar caps of the blade to generate the bending-twisting coupling. It is concluded that with the introduction of bending-twisting coupling, damage equivalent loads can be reduced in the critical connection points of the whole wind turbine system, and not just in the blades. Proper adjustment of the bending-twisting coupling and flapwise stiffness is also necessary to achieve load reduction in the overall wind turbine system. Although the focus of the thesis is blades of the wind turbine, since the whole wind turbine system is used in analysis, the thesis indicates where one also need modifications in wind turbine system to introduce the bending-twisting coupling for future works.

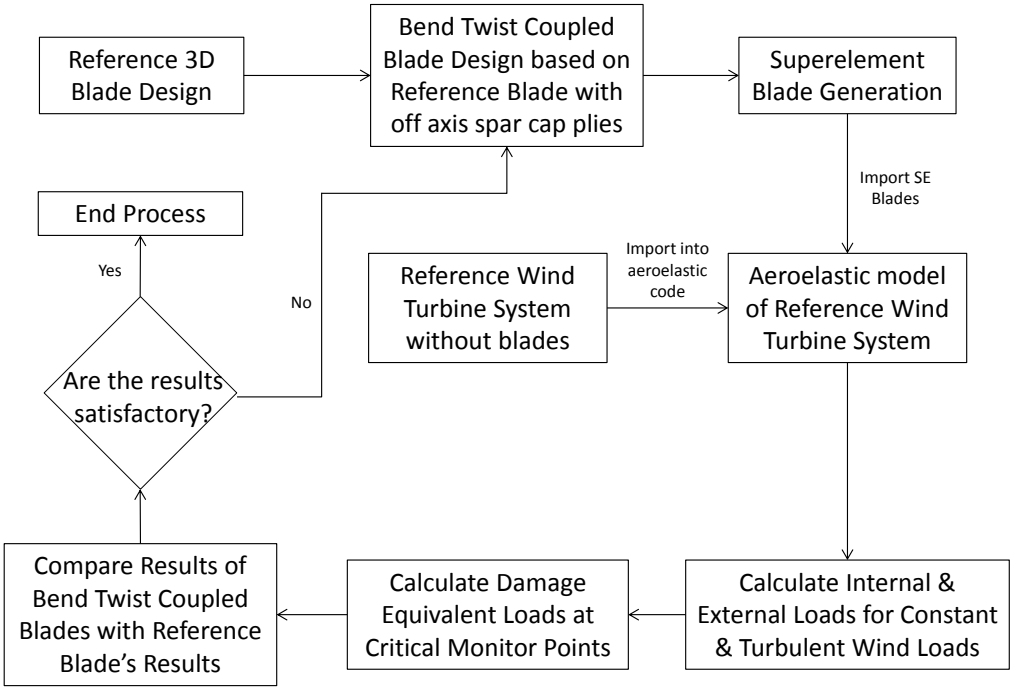

Figure 1.3: Flow chart of the thesis which shows the main design and analysis steps

CHAPTER 2

INVERSE DESIGN OF NREL 5 MW BLADE

To model the coupling effects and optimize them for the load reduction, one must know the lay-up scheme of composite blade cross-sections. Hence coupling terms in the stiffness matrix can be determined. For accurate modelling of wind turbines systems for the purpose of studying the effect of coupling stiffness on the load alleviation, beam models of wind turbine blades with the full stiffness matrix, including the coupling stiffness terms, must be used in the flexible multi-body model of the complete wind turbine system.To calculate the fully populated stiffness matrix of the beam model of the wind turbine blade, three dimensional model of the blade with the complete composite lay-up definition is needed. In the flexible multi-body model of the wind turbine system, turbine blades modelled with coupled beam elements are preferred to reduce the computation time of the transient aero-elastic analysis. Another way of representing the blades in a multi-body model of a wind turbine system is to use the dynamic superelement of the blade. The main advantage of sub structuring techniques to describe flexible multi-body systems is to allow the detailed modelling of components with complex geometry and structural function while keeping a relatively simple global dynamic model with the smallest number of degrees of freedom possible [2]. Since dynamic superelements are created from the three dimensional finite element models of the blades, superelements possess the whole coupling effects [21]. In either beam or superelement modelling approach of the turbine blade, a three dimensional reference blade is needed to construct the beam and the superelement models of the blade so that the effect of coupling stiffness, such as bending-twisting coupling, on the load alleviation in the wind

turbine system can be studied. In the literature, blade of NREL's 5MW reference turbine is used by many researchers as the reference blade [27]. In NREL's report [27] stiffness values and geometric properties of cross sections of the blade are given. However, in the report, ply lay-up of blade cross-sections and the real pitch axis location of the cross-sections are not given. To create the superelement model of the blade and to study the effect of bending-twisting coupling induced in the blades on the load alleviation in the wind turbine system, complete blade properties are needed so that beam models or superelement models of the blade can be created. It is important to note that the aim of this thesis is not to make a full three dimensional blade design with all strength, buckling and fracture analysis performed. The aim of the inverse blade design is to create realistic blade geometry and determine the ply schemes of the cross-sections, which give realistic stiffness values similar to a realistic blade such as NREL's 5 MW blade. Three dimensional blade design can then be used to generate the superelement of the blade so that it can be used in studying the effect of bending twisting coupling on load alleviation.

2.1 Blade Geometry

Turbine blade of NREL's 5 MW wind turbine system is modeled at 17 cross-sections in the spanwise direction. Based on the definitions of the airfoil sections given for the blade of NREL's 5MW turbine, blade geometry is created by adjusting the cross-sections of the blade in the chordwise direction so that shear webs contain the pitch axis which passes through the center of the circular root section. Except for the first three root sections, all other sections have leading and trailing edge spar caps and upper and lower skin spar caps. On the upper (suction side) and lower (pressure side) skins of the blade, between the two shear webs, there are unified spar caps which are connected to the shear webs. Spar caps have constant laminate widths along the blade axis except for the first three cross sections of the root part. Leading edge and trailing edge spar caps have 25 cm laminate width, while the laminate width of upper and lower skin spar caps is 60 cm. These values are common widths used in the wind turbine industry. In

locating the positions of the shear webs, attention is also given such that shear webs are as close as possible to the maximum thickness of the airfoil sections. External geometry of the blade is determined according to the definitions given in NREL's report [27]. However, in NREL's report, there is no detailed information about the transition part near the root. Therefore, the transition part of the blade is determined by adjusting the thickness to chord ratio to achieve a smooth transition along the blade axis. At the transition part of the root section, five new airfoil designs are defined by the XFOIL code [17] which is capable of mixing two airfoil shapes with respect to the given mixing ratio. However, for structural analysis purposes only two additional cross-sections are used in the transition region. All transition cross-sections are a mixture of circular cross-section and DU40 A17 profile [1] in different ratios to get the target maximum thickness to chord ratio which satisfies maximum thickness to chord ratio of a conventional wind turbine blade. Figure 2.1 shows the thickness to chord ratio of the blade along the spanwise direction with two transition cross-sections between the root and the first airfoil section. The coordinate points of two transition airfoils are given in the Appendix A. Table 2.1 shows the airfoils and chord lengths of the cross-sections along the spanwise direction. It should be noted that in the NREL's report, the transition part is given as "Circle-2", but there is no definition about the cross-sectional coordinate points of "Circle-2". Therefore, transition part of the blade is also completed in this thesis.

The chordwise locations of cross-sections with respect to the pitch axis are another issue while determining the external geometry of the blade. Although there is no reference data for the chordwise locations of cross-section, the primary goal is to get a final geometry that looks like a commercial blade with spar cap regions as close as possible to the maximum thickness location of the cross-sections. Figure 2.2 shows how the blade geometry looks from the top view. Spar caps are placed between two shear webs and the black line is the maximum thickness location of the cross-sections.

[1] the DU air foil profiles are used by the permission of the Delft University

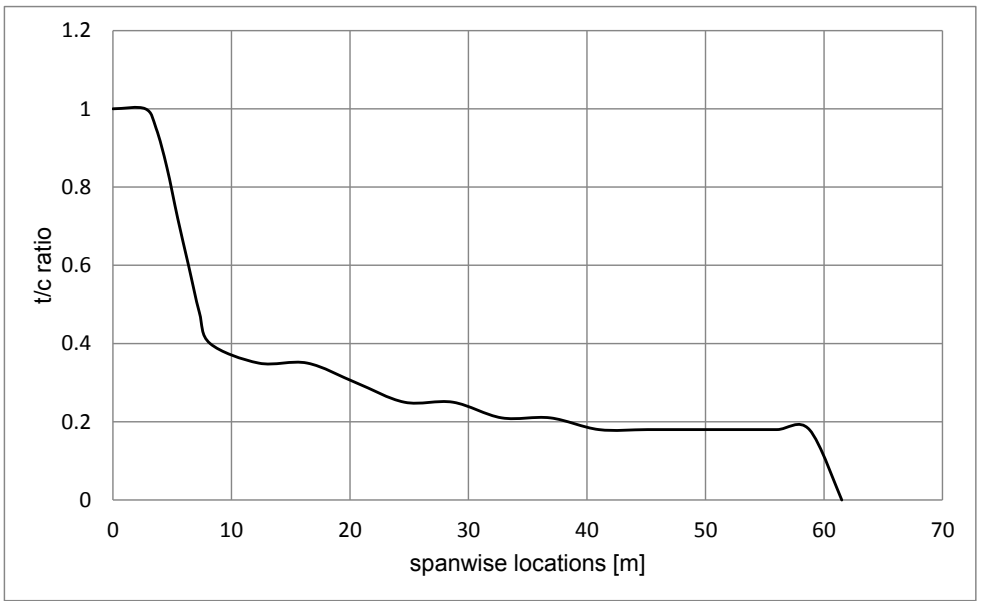

Figure 2.1: Thickness to chord ratio of the blade geometry

Table 2.1: Airfoil distribution of the NREL's 5 MW wind turbine blade

Spanwise Starting Point (m)	Chord length of cross-section	Name of airfoil
0	3.542	Circle
3.6444	3.711	Transition 1
5.4666	4.0495	Transition 2
8.1999	4.557	DU40 A17
12.2999	4.652	DU35 A17
16.3999	4.458	DU35 A17
20.4999	4.249	DU30 A17
24.5999	4.007	DU25 A17
28.6999	3.748	DU25 A17
32.7999	3.502	DU21 A19
36.8999	3.256	DU21 A20
40.9999	3.01	NACA64(3)618
45.0999	2.764	NACA64(3)618
49.1999	2.518	NACA64(3)618
53.2999	2.313	NACA64(3)618
56.0332	2.086	NACA64(3)618
58.7665	1.419	NACA64(3)618
61.4998	0.5	NACA64(3)618

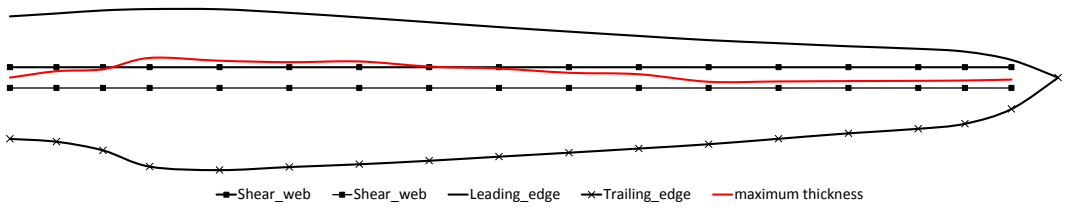

Figure 2.2: Up view of the blade geometry. Maximum thickness location is tried to be located near to the shear webs (spar locations)

2.2 Initial Spar Cap Design

The spar-cap regions are the most critical part in the inverse design process because they are the main stress carrying regions in the cross-sections. In addition, the flapwise and edgewise stiffness values mainly depend on the material and thickness of the spar cap regions. Changing the ply orientations in the mid-spar caps between the main shear webs induces the bending-twisting coupling see Figure 2.3. Therefore, the initial design step is to determine the ply numbers in the spar caps by using an in-house developed code. Three different spar cap designs are performed as part of initial spar cap design. These designs are:

- All spar caps are made of UD Glass Fiber/Epoxy composite
- Leading and trailing edge spar caps are made of UD Glass Fiber/Epoxy composite and middle spar caps are made of UD Carbon Fiber/Epoxy composite
- All spar caps are made of UD Carbon Fiber/Epoxy composite

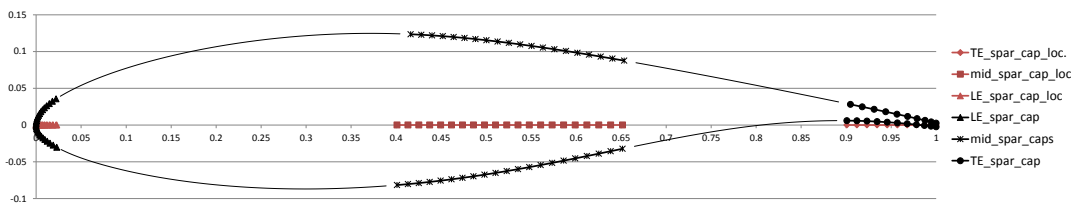

Figure 2.3: Spar cap regions and projections of them on the chordwise locations of an airfoil section

To start a structural design, geometry and loads are needed. The blade geometry is completed, now the loads on the structure are needed to be determined. Figure 2.4 shows the spar cap regions of the blade on a 3D blade geometry. In the present study, design load cases are selected as "extreme operating gust" (EOG) wind for 50 years defined in the GL standards [35]. The cross-sectional flapwise and edgewise bending moments are calculated in FAST [26] by using the NREL's 5 MW blade.

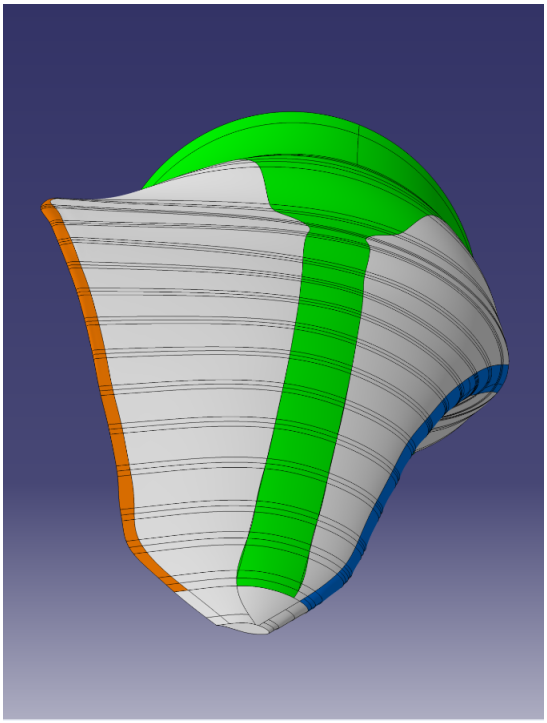

Figure 2.4: Spar cap regions shown on 3D blade geometry, green region is middle spar caps, orange region is trailing edge spar caps and blue region is leading edge spar caps

2.3 Calculation of Extreme Operating Gust Wind

The EOG wind profiles for 50 years are created for two hub wind speeds; first case is at Vhub=11.4 m/s which is the rated speed of the NREL's wind turbine [27] and second case is at Vhub=25 m/s which is the maximum operating wind speed of the wind turbine. The starting time of the gust wind is selected as 50 seconds and the duration of the gust is 14 seconds for both hub wind speeds.

Wind speed calculation with respect to time is calculated by Equation 2.1 [35]. Constants in the Equation 2.1 are selected from GL standards for the wind turbine class A due to the fact that EOG speed is higher for this wind turbine class. Because of large rotor diameter to get a realistic case, for each wind profile, normal shear constants are defined in Aerodyn [17] input file which includes wind data and can be read by FAST [26].

$$V(z,t) = \begin{cases} V(z) - 0.37 V_{gN} sin(\frac{3\pi t}{T})(1 - cos(\frac{2\pi t}{T})) & \text{for} \quad 0 \leq t \leq T \\ V(z) & \text{for} \quad t < 0 \ \& \ t > T \end{cases} \tag{2.1}$$

where:

$$V_{gN} = \beta \ \sigma_1 \ B \tag{2.2}$$

$$B = \frac{1}{1 + 0.2(\frac{D}{\Lambda_1})} \tag{2.3}$$

$$\sigma_1 = I_{15}(15m/s + aV_{hub})/(a+1) \tag{2.4}$$

$V(z,t)$ is the velocity function at hight "z" and time "t"

β = 6.4 for N = 50 years recurrence period

$I_{15} = 0.18$ for WT class A

a = 2 for WT class A

Λ_1 = 42 m turbulence scale parameter for hub height higher than 60m

D = diameter of turbine

Figure 2.5 and Figure 2.6 show gust wind velocities with respect to time. For $V_{hub} = 11.4\ m/s$, maximum wind speed reaches 18.1 m/s and for $V_{hub} = 25\ m/s$

maximum wind speed reaches 36.5 m/s.

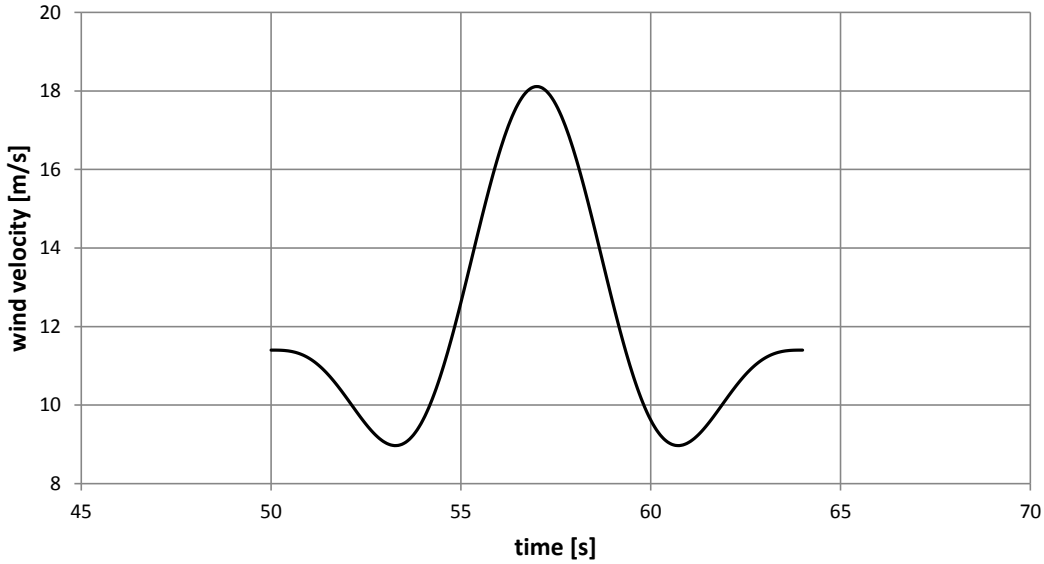

Figure 2.5: Wind Velocity vs. Time for gust wind with $V_{hub} = 11.4\ m/s$

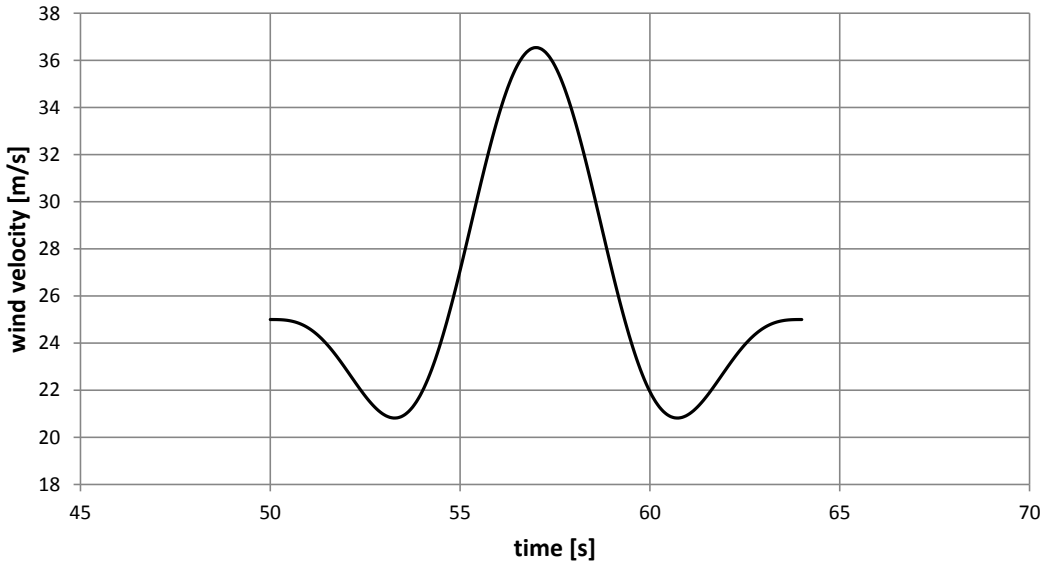

Figure 2.6: Wind Velocity vs. Time for gust wind with $V_{hub} = 25\ m/s$

2.4 Calculation of Section Moment Loads by FAST

Cross-sectional loads that are used in the design of the spar caps of the wind turbine blade, are calculated by using FAST [26]. The wind turbine model in FAST analyses is NREL's 5 MW wind turbine [27]. Table 2.2 shows the general properties of the wind turbine model. Analyses are performed for two EOG wind profiles and for normal operating wind speed which is 11.4 m/s and 25 m/s. The analysis duration is taken as 80 seconds which is enough to damp the gust effects on the structure and the file size is suitable to work with. Also, results of first 40 seconds are not written to output file to minimize the file size.
FAST can give span wise moment loads for maximum nine cross-section points, for each load case two FAST run are performed to have moment loads for all span wise locations. By means of a Fortran code, maximum and minimum flap-wise and edge-wise bending moments are selected from the Fast output files for each section. Results showed that not all of ultimate cross section loads occurred at the EOG load case for the maximum operating speed of 25 m/s. It is seen that some of the ultimate cross-section loads occurred at the EOG load case at the rated speed of 11.4 m/s. Four different ultimate load cases are considered in the design process. These load cases correspond to maximum and minimum flapwise and edgewise moments separately. Figures 2.7-2.10 show the moment load distribution for the four different ultimate load cases.

Table 2.2: General Properties of the wind turbine defined in FAST

Nominal Power	5 MW
Number of Blades	3
Control	Pitch, variable speed
Rated rotor speed	12.1 RPM
Gearbox ratio	97
Rotor/Hub Diameter	126 m / 3 m
Hub length	4 m
Blade length	61.5 m
Rotor tilt angle	5 degree
Blade cone angle	-2.5 degree
Height of tower	87.6 m
Hub mass	56.78e3 kg

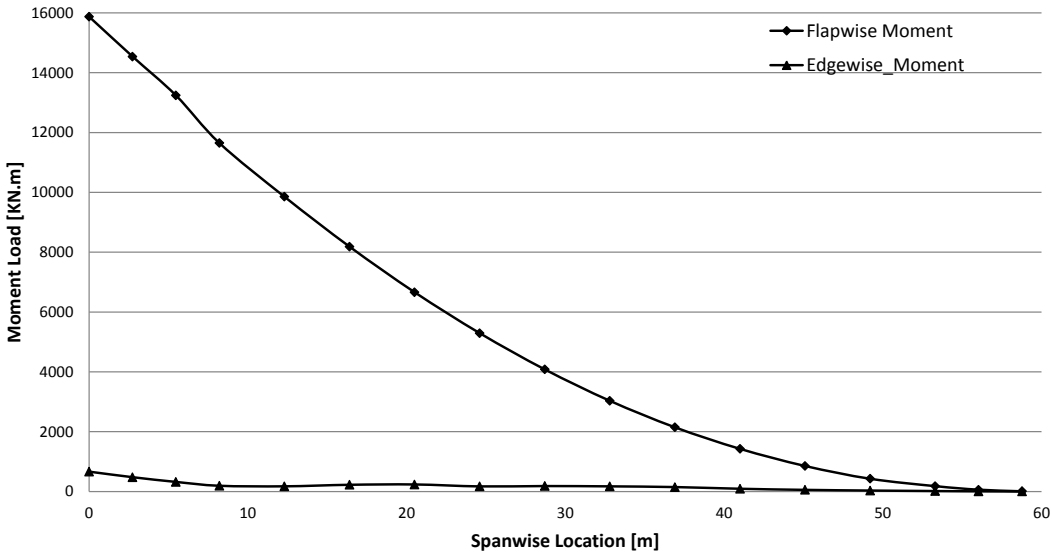

Figure 2.7: Moment load distribution of the blades when maximum flapwise moment occurs

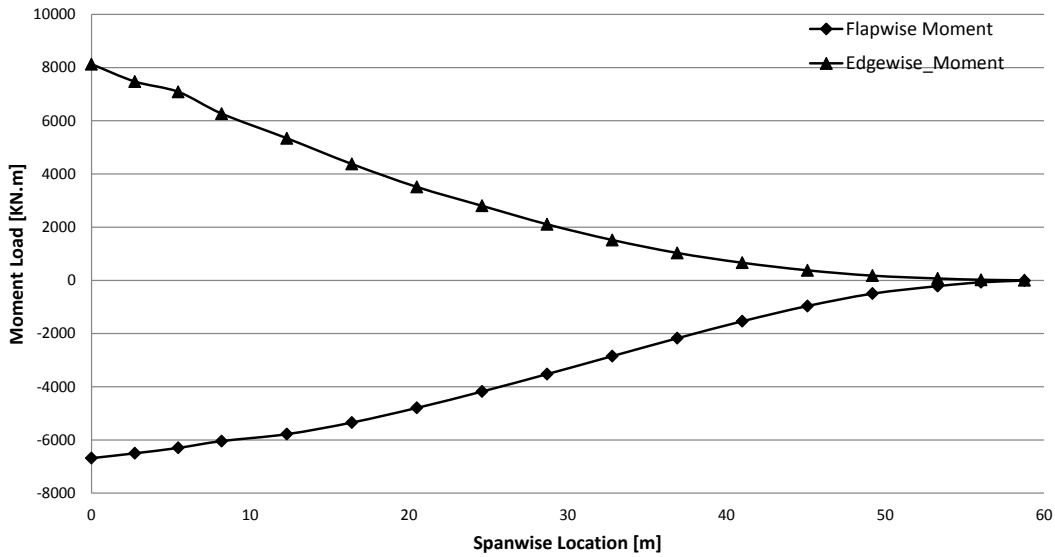

Figure 2.8: Moment load distribution of the blades when minimum flapwise moment occurs

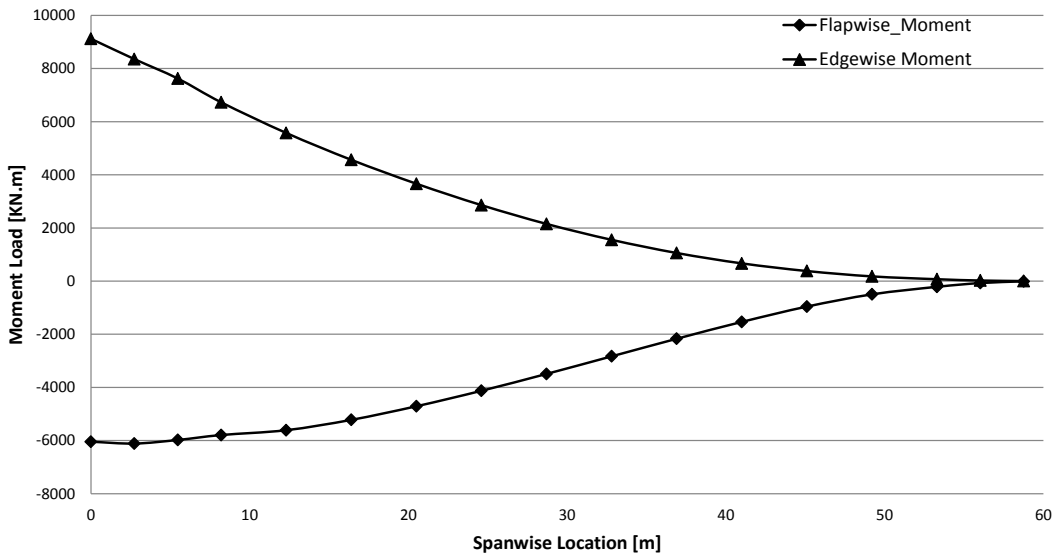

Figure 2.9: Moment load distribution of the blades when maximum edgewise moment occurs

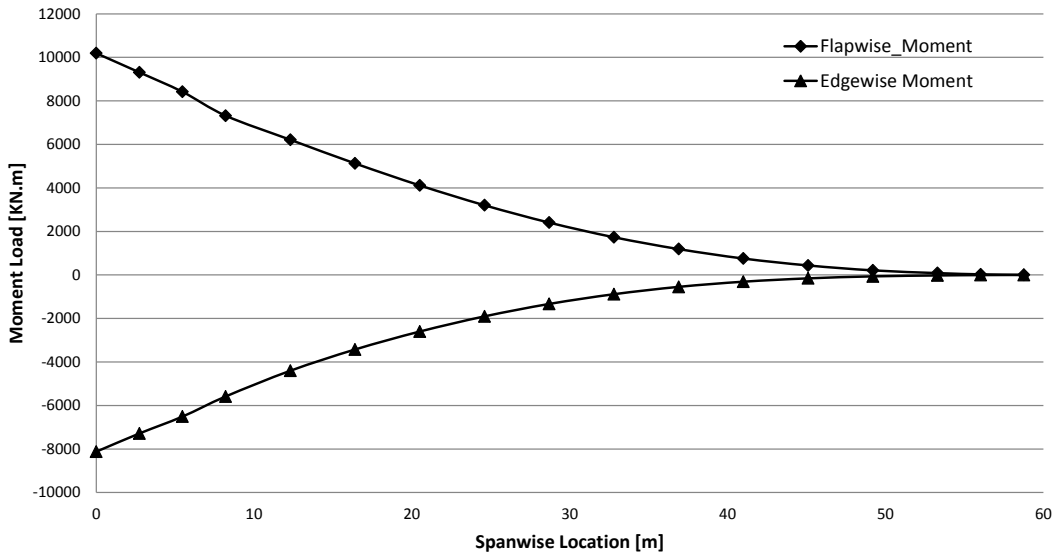

Figure 2.10: Moment load distribution of the blades when minimum edgewise moment occurs

2.5 Stress Calculation and Failure Check

Stress calculations and failure checks are performed by using an in-house code developed in Octave [18]. There are six main parts in the algorithm of the code developed;

1. Read coordinates of cross-sections and laminates
2. Determination of the coordinates of the center of the area for each cross-section
3. Calculation of cross sectional inertia: I_{xx}, I_{yy}, I_{xy}
4. Determination of the absolute maximum values of the stresses in the spar caps
5. Calculation of the strain values corresponding maximum and minimum stresses
6. Calculation of stress exposure ratios according to Puck Failure criteria [44]

For the cross-sections, which have two or more different material types, the so-called transformed section method approach described in Mechanics of Material books [6] and in the study of Philippidis [43] is used. Equation 2.5 shows the factor used in transformed section method.

$$F_n = 0.5 \times (\frac{Rt_h}{Rt_n} + \frac{Rc_h}{Rc_n}) \tag{2.5}$$

where:
F_n is the factor used in transformed section method at n^th section
Rt_h and Rc_h are tension and compression strength of the strongest material respectively.
Rt_n and Rc_n are tension and compression strength of section "n"

For each region of the cross sections the transformed section factor is calculated and it is included in the inertia calculations. The thickness of the spar cap is multiplied by the factor to determine inertia of cross sections which have glass fiber (GF) and carbon fiber (CF) plies together. Therefore, the factor directly effects the strain and stress calculations. Inertia calculations are done by Equation 2.6 and Equation 2.7.

$$I_{sect_i} = \sum_{n=1}^{k} L_n t_n d_n^2 F_n \tag{2.6}$$

$$L_n = \sqrt{(x_1 - x_2)^2 + (y_1 - y_2)^2} \tag{2.7}$$

Equation 2.8 shows the bending stress calculation formulation used in the code. Equation 2.8 is the generalized unsymmetric bending formula used to calculate the bending stress in the blade sections. Table 2.3 shows the code results and analytical results for a circular cross-section.

$$\sigma_z = (\frac{M_y I_{xx} - M_x I_{xy}}{I_{yy} I_{xx} - I_{xy}})x + (\frac{M_x I_{yy} - M_y I_{xy}}{I_{yy} I_{xx} - I_{xy}})y \tag{2.8}$$

$Outer\ diameter\ of\ circle = 1\ m$

$Inner\ diameter\ of\ circle = 0.98\ m$

$M_x = 1350\ Nm$

$Number\ of\ points\ to\ define\ circle = 161$

Table 2.3: Comparision of analytical results and code results

Property	**Analytical Results**	**Code Results**	**Relative Error [%]**
Perimeter	3.1416	3.1404	0.04
I_{xx}	$3.811e-3$	$3.852e-3$	1.08
I_{xy}	0	$-2.372e-20$	0
σ	$1.7713e5$	$1.7523e5$	1.07

For the initial spar cap design, glass-fiber reinforced plastic (GFRP) and carbon-fiber reinforced plastic (CFRP) are defined as materials of the cross-sections. Material data is given in the Table 2.4. The Poisson's ratio (ν_{12}) of GF-EP is 0.3 and CF(HT)-Ep is 0.26. The density of the GF material is $2007 kg/m^3$ and CF material is $1486 kg/m^3$. It is also possible to include new material types in the cross-sections easily. There are some safety factors used in calculations both for material properties and loads. The safety factors used in the code are;

- 4.4 for UD laminates

- 1.6875 for biax laminates
- 1.35 for moment loads

Table 2.4: Material properties of GFRP and CFRP composite plies which are used in blade structure

Material Name	E_1 (MPa)	E_2 (MPa)	G_{12} (MPa)	R^t_{fiber} (MPa)	R^c_{fiber} (MPa)	R^t_{matrix} (MPa)	R^c_{matrix} (MPa)
GF-EP	39,140	13,219	3,937	866	647	54	150
CF(HT)-EP	123,404	8,180	4,571	1,800	1,200	60	200

Equations 2.9 and 2.10 show Puck failure criteria and the stress exposure factor calculations [44, 41]. The GL standards [35] suggest using Puck Failure Criteria for failure analysis of rotor blades. Although there are only UD material definition in the spar cap regions of the cross sections, the failure checks of the bi-axial materials in the vicinity of the spar cap regions are also performed assuming that bi-axial materials have the same strain value as the UD materials. Stress exposure ratios of all material sections are calculated according to equations given in Ref. [41]. To check the structural integrity of blade sections, all stress exposures in a cross section are compared with unity. If all stress exposures are less than one then no failure is predicted in the cross section.

$$FF : \begin{cases} \dfrac{\sigma_1}{R^t_{fiber}} & \text{for} \quad \sigma_1 > 0 \\ \dfrac{\sigma_1}{-R^c_{fiber}} & \text{for} \quad \sigma_1 < 0 \end{cases} \tag{2.9}$$

$$IFF : \begin{cases} (\dfrac{\tau_{nt}}{R^A_{fiber}}) & \text{for} \quad \sigma_1 > 0 \\ \dfrac{\sigma_1}{-R^c_{fiber}} & \text{for} \quad \sigma_1 < 0 \end{cases} \tag{2.10}$$

There are five main inputs to perform the stress calculations by the Octave code. These are the airfoil geometry, spar cap locations, loads, materials and laminate numbers. First three of these input are read by the code from a data file. Other

two inputs are written in the input part of the code and changed manually in the code. Airfoil geometry data file consists of coordinate points of the airfoil. Point locations are normalized so that the chord value of the airfoil is made unity. Spar cap locations and chord length are read from another input data file. Spar cap locations are given as the ratio of chord which must be calculated beforehand. To illustrate an example, section 10 from the input file is shown Table 2.5 below.

Table 2.5: Example line of the input file which describes the spar cap regions by their chordwise locations

Chord Length	Starting Point of 60 cm Spar Cap	End Point of 60 cm Spar Cap	End point of LE Spar Cap	Start Point of TE spar Cap
3.5020	0.2943	0.4650	0.0200	0.9630

The number in the first column of Table 2.5 is the sectional chord length of the cross section and it is multiplied by the normalized coordinates in columns 2-5 to calculate the spar cap positions in the chordwise direction. Columns 2 and 3 give the location of the 60 cm spar cap in terms of the percent sectional chord. At the 29.43 percent of the chord, 60 cm spar cap starts and it ends at the 46.50 percent of the chord. Columns 3 and 4 give the end point of the leading edge spar cap and the starting point of the trailing edge spar cap, respectively. For the LE spar cap, there is no need to define a starting point since it is assumed that the starting point of the LE spar cap is at 0 percent location of the sectional chord. Figure 2.3 shows the main spar cap locations and corresponding projections of the spar cap locations on the chord of an airfoil which has unit chord length.

2.6 Results of Initial Spar Cap Design

2.6.1 All Glass Fiber/Epoxy Composite Spar Cap Design

All Glass Fiber/Epoxy composite spar cap design is the heaviest design among the three designs. In this design, lowest stress exposure ratios are obtained. The reason for low stress exposure ratios is that biax laminates cannot withstand the

tensile strains of UD glass fibers if the stress exposure value of UD glass fibers in the spar caps is higher than approximately 0.33. Biax laminates limit the stresses in the spar caps, therefore very low stresses occur in the spar caps resulting in low stress exposure values. It should again be noted that in the design process, although no biaxial material in the regions between the spar caps are used, strength checks of the biaxial material which will normally be placed in the immediate vicinity of the spar caps are also performed. For the all glass fiber/epoxy composite spar cap design, it is seen that highest stress exposure ratios are obtained for compression state of stress. Figure 2.11 shows the maximum stress exposure ratio distribution over the span of the blade for the full glass/epoxy spar cap blade. It should be noted that stress exposure ratios are only given for the spar cap material.The maximum stress exposure ratio is determined as 0.6625 at the fifth section of the upper spar cap.

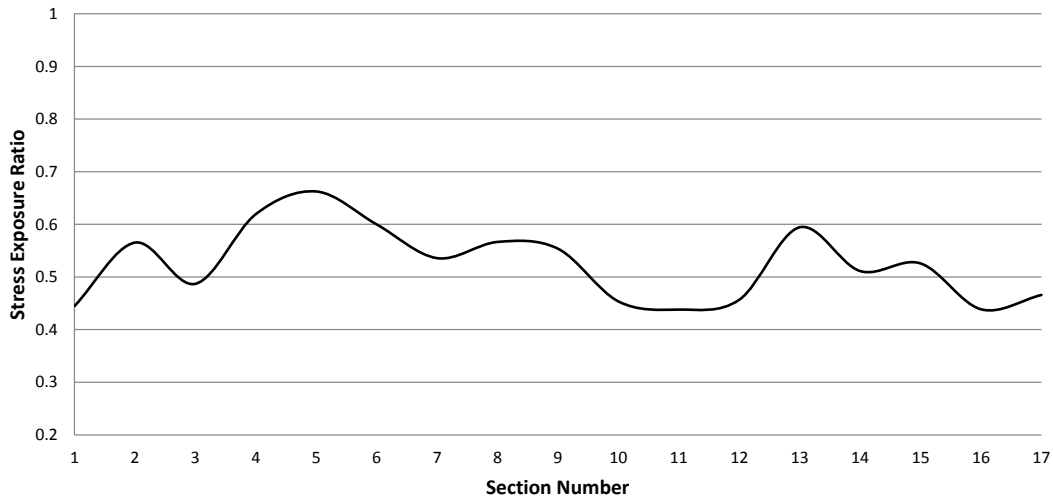

Figure 2.11: Stress exposure results of GFRP spar cap design

2.6.2 Hybrid Glass Fiber/Epoxy Carbon Fiber/Epoxy Composite Spar Cap Design

In the hybrid design, middle spar caps are made from Carbon Fiber/Epoxy laminates whereas leading edge and trailing edge spar caps are made from Glass Fiber/Epoxy laminates. In the hybrid design, carbon fibers carry more stress

than glass fibers and they have less strain due to the larger elastic modulus value. Therefore, stresses occurring in glass/epoxy biax laminates near middle spar caps also decreased because of low strain values of the spar caps. However, in this case stress exposure ratios are higher compared to the full glass/epoxy design, and maximum stress exposure ratio occurred in the carbon/epoxy. Again, almost all of the maximum stress exposure ratios occur when the stress state is compression. Figure 2.12 shows the maximum stress exposure ratio distribution over the span of the blade for the hybrid carbon/epoxy, glass/epoxy spar cap blade.The maximum stress exposure ratio is determined as 0.9849 at the second section of the upper spar cap.

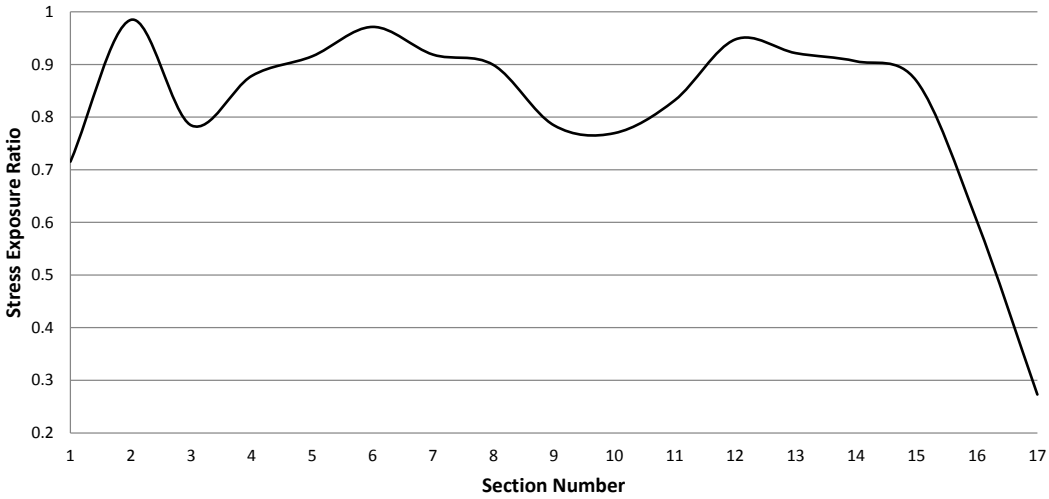

Figure 2.12: Stress exposure results of mix (GFRP and CFRP) spar cap design

2.6.3 All Carbon Fiber/Epoxy Composite Spar Cap Design

Figure 2.13 shows that all carbon/epoxy design also has high stress exposure ratios over the span of the blade similar to the hybrid design. Again, strength check of the biaxial laminates in the immediate vicinity of the spar caps plays a key role in the final stress exposure ratio distribution for the spar caps. The maximum stress exposure ratio is determined as 0.99 at second section of the upper spar cap. Figure 2.13 shows the maximum stress exposure ratio distribution over the span of the blade for the carbon/epoxy spar cap blade.

All carbon fiber/epoxy design turned out the lightest design as expected. Fig-

ure 2.14 shows the sectional weight results of the initial spar cap designs of the blades. Weight results are given from section 4 to 17 since by using only the spar cap regions the design of root sections are not reliable.

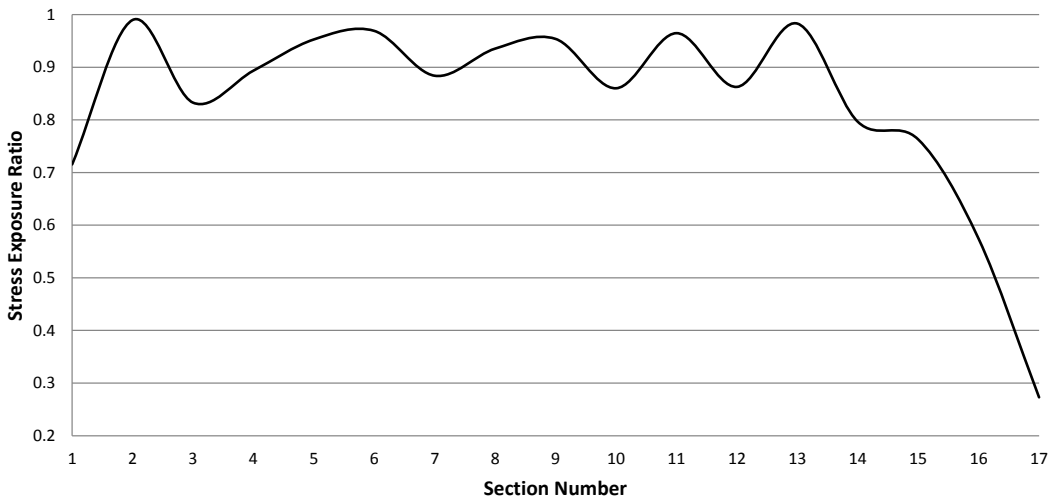

Figure 2.13: Stress exposure results of CFRP spar cap design

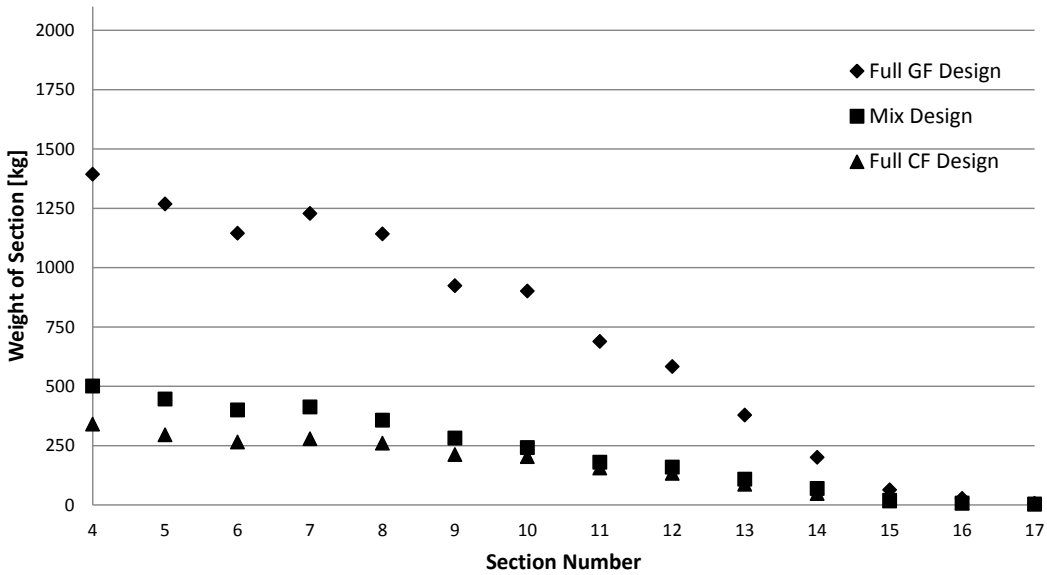

Figure 2.14: Sectional weights of three initial spar cap designs between section 4-17

2.7 Inverse Design Methodology of the NREL Blade

Inverse design of the blade is described in the flowchart given in Figure 2.15. Inverse design starts with the spar cap design performed in the previous step. Biaxial composite laminates are defined in the regions between the leading/trailing edge spar caps and shear web spar caps on the suction and pressure side of the blade. Biaxial laminates which are composed of $\pm 45^0$ layers are used in the regions between the spar caps and no core material is used in the skins. For each section of the blade, appropriate laminate definitions are made for the suction and pressure side regions between the already designed spar caps. Each section of the blade is then defined in the PreVABS program [14] which prepares input files for VABS [48]. Figure 2.16 shows the process for the calculation of beam cross sectional properties using PreVABS and VABS. PreVABS is the preprocessor of the VABS. It generates 2D meshes over the cross sections and define material properties of mesh elements. To define the cross section in PreVABS, the data points of the airfoil is written in an input file. Between two cross section point, Variational asymptotic beam section code VABS calculates the sectional beam properties of blade section which are then compared with the known beam properties of the blade of NREL's 5 MW wind turbine system [27]. Iterations continue until an acceptable difference between the sectional beam properties are obtained for each section of the blade. The goal of the inverse design methodology is to come up with full GFRP blade design without any core material so that these designs can be used as reference blades to study the effect of coupling stiffness on load alleviation. Therefore, certain design checks, such as buckling and strength check of the skins, are not made. In the inverse design process, as the first goal, it is aimed to have the same order of magnitude beam stiffness properties as the known beam properties of the blade of NREL's 5 MW wind turbine system. After matching the orders of magnitude, further design iterations are performed to reduce the differences between the beam properties of the blade designed in an inverse fashion and the blade of NREL's 5 MW turbine.

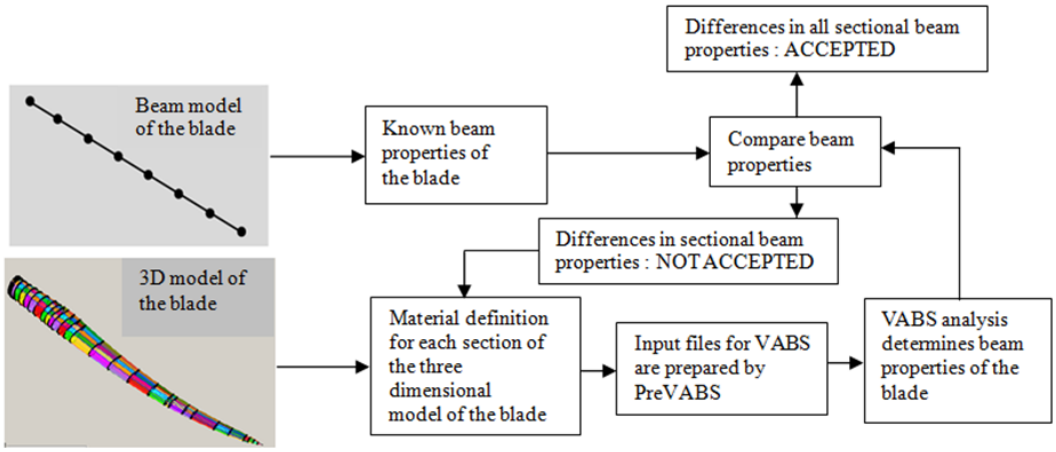

Figure 2.15: Three dimensional design loop of a wind turbine blade with known cross-sectional beam properties

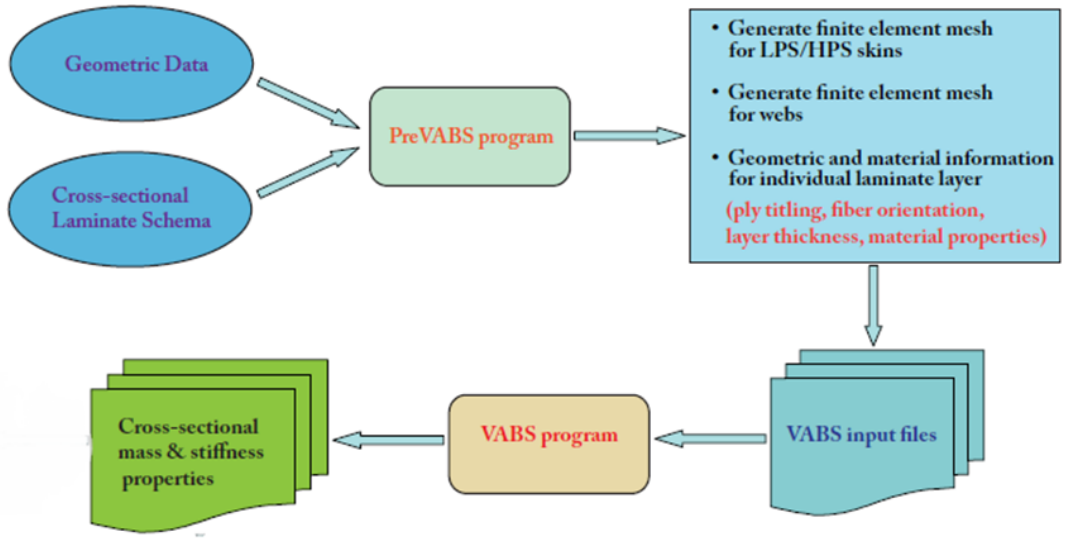

Figure 2.16: Calculation of the beam cross sectional properties using PreVABS and VABS

2.7.1 VABS

It will be useful to briefly discuss VABS. A wind turbine rotor blade has its length much greater than the other two dimensions (chord and thickness direction). Hence it has often been treated as a beam, a 1-D structure, to reduce the computational costs associated with the analysis. This reduction process needs to capture the behavior associated with the cross sectional coordinates

(two omitted dimensions) by correctly accounting for the cross sectional geometry and material distribution for analysis without loss of accuracy. VABS is a computer tool which is able to calculate the beam cross sectional stiffness constants, with transverse shear and Vlasov refinement for initially twisted and curved beams with arbitrary geometry and material properties. The mathematic basis of VABS is the Variational asymptotic method (VAM) developed by Berdichevsky [7]. VAM is used to split a general 3D nonlinear elasticity problem for a beam like structure into a 2D cross-sectional analysis and a 1D nonlinear beam analysis. The reduced order model of the 3D structural model is generated in terms of an asymptotic series of certain small parameters inherent to the structure. These small parameters are a/ξ and a/R, where a is the characteristic length of the cross-section, ξ is the characteristic wavelength of deformation along the longitudinal direction, and R is the characteristic radius of the initial curvature and twist. For a straight blade a/ξ is the main small parameter. As the mode number n increases, the characteristic wavelength of deformation (ξ) will decrease, roughly proportional to L/n where L is the length of a beam. Therefore the accuracy of the 1D theory deteriorates as a beam length becomes shorter and as high-frequency modes are considered. VABS development and comparison with other composite beam theories are described in Refs. [12, 13, 22, 23, 32, 49].

2.7.2 Full Material Definition of Cross-Section

As an example calculation, Figure 2.17 shows the details of the leading edge spar cap, suction side spar cap and trailing edge spar cap in a particular section of the full GFRP blade which is modeled by PreVABS. In the particular section, there are 79 UD plies in the spar cap region, 12 UD plies in the leading edge, 14 UD plies in the trailing edge spar cap for both lower and upper skins of the blade. In addition, in the regions between the spar caps and in the spar webs, 6 layers of biaxial E-Glass composite layers are used PreVABS generates 2D mesh on the material thickness of a cross section geometry. the minimum length of a element is equal to minimum thickness of a ply. Therefore each element is defined by one material in VABS. The initial guess on the minimum number of

biaxial layers is based on the work of Gunjit [9] who uses a minimum number of 3 biaxial layers as the default in the code that is developed.

In the inverse design process, design iterations are performed by PreVABS and VABS, and number of layers in each section is modified to obtain closer sectional beam properties as the known sectional beam properties of NREL's 5MW turbine blade. At the current state of the study, there is some arbitrariness in the inverse design process, and in the design iterations good engineering aptitude is needed to obtain closer sectional beam properties as the known sectional beam properties of NREL's 5MW turbine blade. It should be noted that without knowing the actual materials used in the blade of NREL's 5 MW turbine, it is not possible to get closer values for all the sectional beam properties through the inverse design process simultaneously. In the current study, it is aimed have blade designs which have sectional beam properties which are within 30% of the sectional beam properties of the blade of NREL's 5 MW turbine.

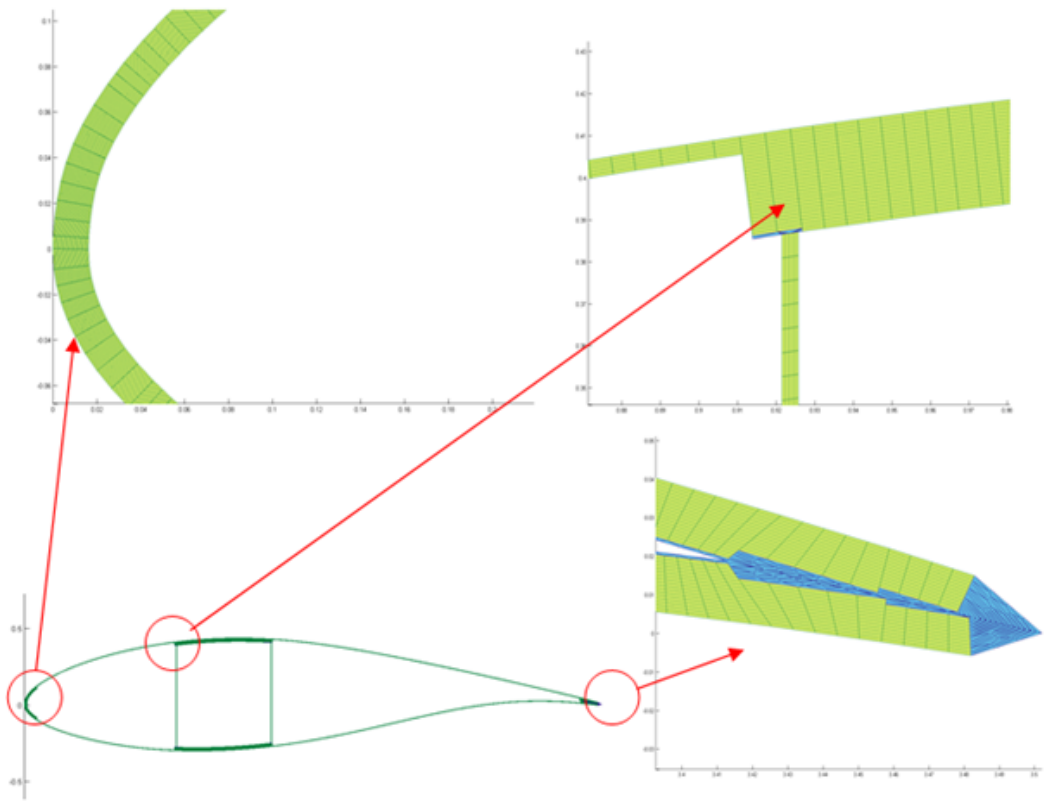

Figure 2.17: PreVABS mesh at a leading edge of a cross section, between shear web and spar cap, on whole cross section and at the trailing edge

2.7.3 Inverse Design Results

Figures 2.18 - 2.23 compare the sectional flapwise bending, edgewise bending and torsional stiffness of the inverse designed blade and the NREL blade [27], respectively, and Table 2.6 gives the numerical values of the sectional stiffness values. From Figures 2.18 - 2.23, it is seen that stiffness values of the inverse designed blade follow the trend of the sectional stiffness properties of the NREL blade. Best matching stiffness is the flapwise bending stiffness. Except for the sections near the tip of the blade, stiffness values of the inverse designed blade are within 30% of the corresponding values of the NREL blade. In the sections near the tip of the blade, such as sections 15 and 16, PreVABS had problems in meshing the leading and trailing edge spar cap regions and gave error messages when the number of plies was increased in the leading and trailing edge spar caps. Therefore, in these sections PreVABS meshes were made for cases with increasing number of layers until PreVABS could not produce any result. Then, the variation of edgewise, flapwise and torsional stiffness values with respect to number of layers are plotted and these curves are extrapolated until close stiffness values are obtained for the inverse designed blade as the NREL blade. Figure 2.24 shows how the torsional stiffness value of section 16 varies with the number of plies in the leading and trailing edge spar caps. For this section, when the number of layers in the leading and trailing edge spar caps is increased above 5, PreVABS could not succeed in meshing the leading and trailing edge spar caps. Therefore, a linear fit is used and the number of plies is increased until the stiffness values determined from the linear fits and the stiffness values of the NREL blade are close to each other. It is seen that addition of unidirectional layers in the leading and trailing edge spar caps did not have appreciable effect of the flapwise bending stiffness. On the other hand, by increasing the number of layers in the leading and trailing edge spar caps, sectional torsional stiffness also increased along with the edgewise bending stiffness. However, in sections 15 and 16 there is a major conflict between the bending stiffness and the torsional stiffness in terms of how they vary with the number of plies. In order to make the edgewise and flapwise stiffness values close to the corresponding values of the NREL blade, number of plies has to be increased. On the contrary, in order

to make the torsional stiffness of the inverse design blade close to the torsional stiffness of the NREL blade, number of plies has to be decreased. Therefore, number of plies in the leading and the trailing edge spar caps is selected by minimizing the deviation of the stiffness values of the inverse design blade and the NREL blade. It should be noted that in the inverse design process, no core material is used and it is aimed to get close to the stiffness values of the NREL blade by using only glass-epoxy material in the plies. Therefore, in some sections it was not possible to match all the stiffness values closely with the stiffness values of the NREL blade.

Table 2.6: Comparison of sectional bending and torsional stiffness values of the inverse designed and the NREL blade

Section	Edgewise Stiffness NREL Blade (Nm^2)	Edgewise Stiffness Inverse Design (Nm^2)	Flapwise Stiffness NREL Blade (Nm^2)	Flapwise Stiffness Inverse Design (Nm^2)	Torsional Stiffness NREL Blade (Nm^2)	Torsional Stiffness Inverse Design (Nm^2)
1	1.96E+10	1.92E+10	1.94E+10	1.83E+10	5.43E+09	4.47E+09
2	1.49E+10	1.17E+10	1.08E+10	1.18E+10	3.47E+09	3.39E+09
3	8.06E+09	6.70E+09	5.53E+09	5.58E+09	1.57E+09	1.43E+09
4	7.17E+09	6.26E+09	4.69E+09	5.08E+09	8.56E+08	8.99E+08
5	5.05E+09	4.97E+09	2.57E+09	2.39E+09	3.36E+08	3.16E+08
6	4.50E+09	4.21E+09	2.05E+09	2.02E+09	2.61E+08	2.75E+08
7	4.00E+09	3.27E+09	1.59E+09	1.38E+09	2.01E+08	2.38E+08
8	3.45E+09	2.80E+09	1.10E+09	1.01E+09	1.44E+08	1.51E+08
9	2.73E+09	2.29E+09	6.81E+08	6.64E+08	8.12E+07	9.07E+07
10	2.33E+09	2.05E+09	4.09E+08	4.26E+08	5.75E+07	6.34E+07
11	1.32E+09	1.07E+09	1.76E+08	1.78E+08	2.74E+07	2.82E+07
12	1.02E+09	1.01E+09	1.07E+08	1.24E+08	1.85E+07	1.73E+07
13	7.10E+08	5.97E+08	7.63E+07	7.83E+07	1.45E+07	1.34E+07
14	4.55E+08	3.45E+08	4.95E+07	3.76E+07	8.06E+06	1.01E+07
15	3.54E+08	2.40E+08	3.47E+07	2.55E+07	6.09E+06	9.51E+06
16	2.81E+08	1.57E+08	2.65E+07	1.35E+07	5.33E+06	8.83E+06
17	8.51E+07	9.02E+07	7.55E+06	6.86E+06	2.17E+06	1.78E+06

It should be noted that in the inverse design process, the primary goal was to match the sectional flapwise and edgewise bending stiffness and torsional stiffness as closely as possible with the corresponding stiffness values of the NREL

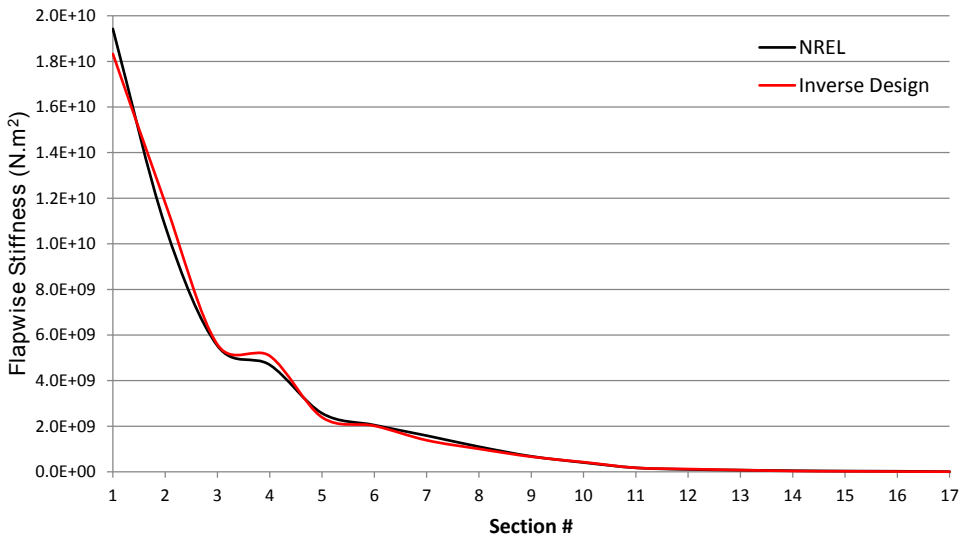

Figure 2.18: Variation of the flapwise bending stiffness of the inverse designed blade and NREL blade between section 1 - 17

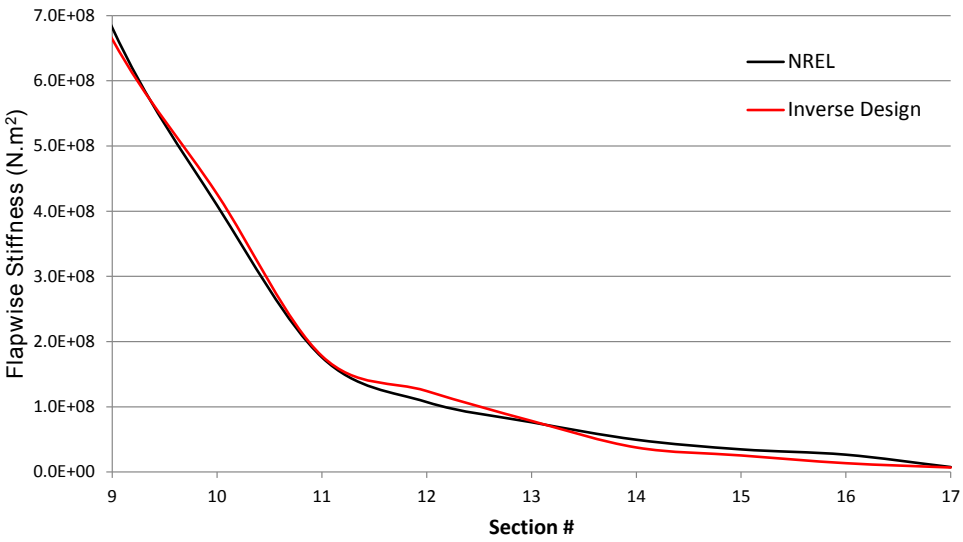

Figure 2.19: Variation of the flapwise bending stiffness of the inverse designed blade and NREL blade between section 9 - 17

blade. In the coupled PreVABS-VABS iterative design analysis, no attempt is made to match the blade mass density. Because without the actual knowledge of the complete material layout used in the blade, it would not be possible to match both the stiffness and the mass properties of the designed blade with the stiffness and mass properties of the NREL blade. Therefore, matching of the blade mass density is not done in the coupled PreVABS-VABS iterative design

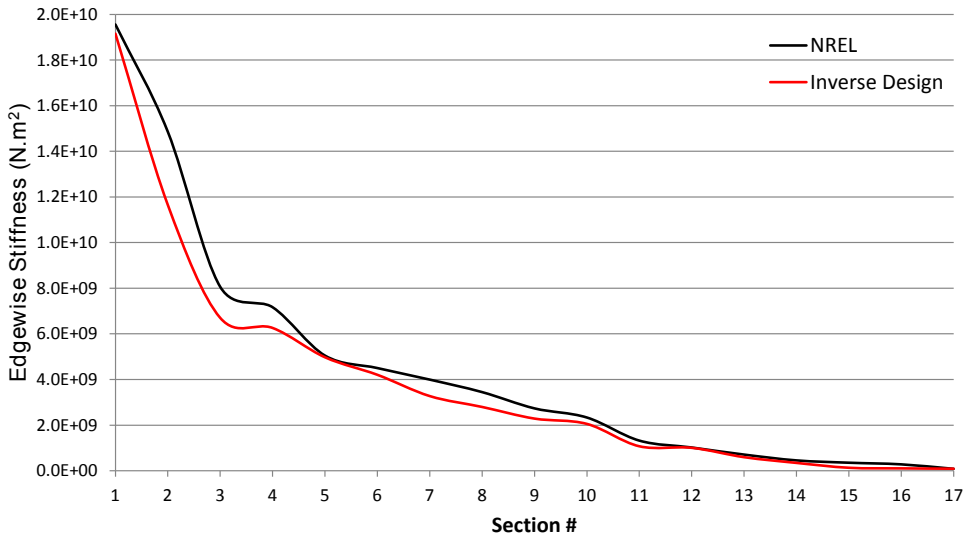

Figure 2.20: Variation of the edgewise bending stiffness of the inverse designed blade and NREL blade between section 1 - 17

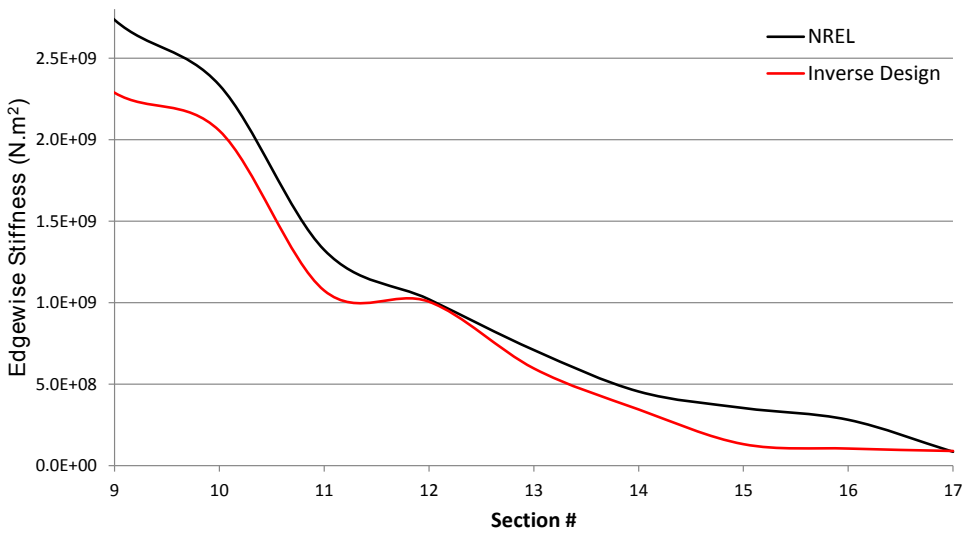

Figure 2.21: Variation of the edgewise bending stiffness of the inverse designed blade and NREL blade between section 9 - 17

analysis process. Matching of the mass density of the blade can be done either during the generation of the dynamic superelement of the blade or inside the multi-body code if beam models of the blade are used in the multi-body analysis of the wind turbine. Matching of the blade mass density can be easily accomplished by assigning appropriate mass densities to the material in each blade section so that sectional blade mass densities match the sectional blade mass

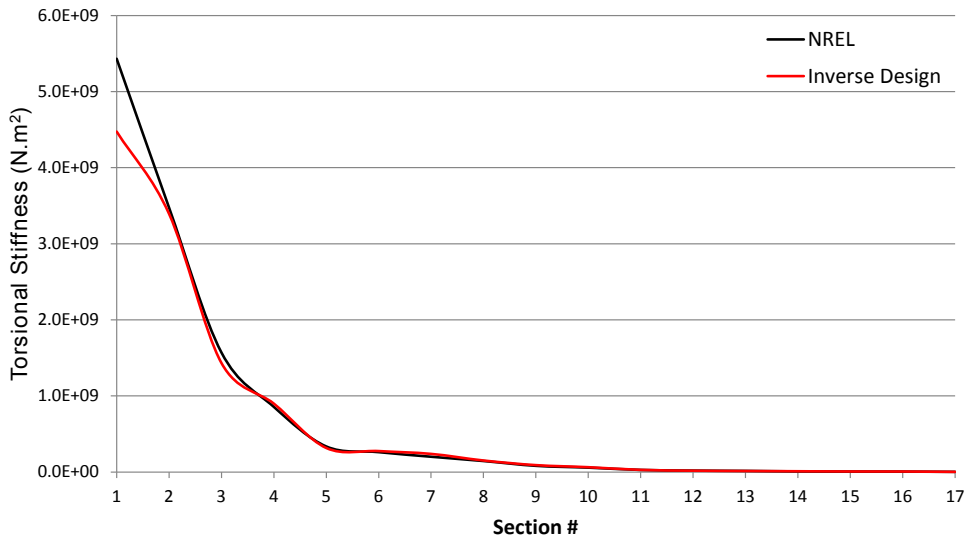

Figure 2.22: Variation of the torsional stiffness of the inverse designed blade and NREL blade between section 1 - 17

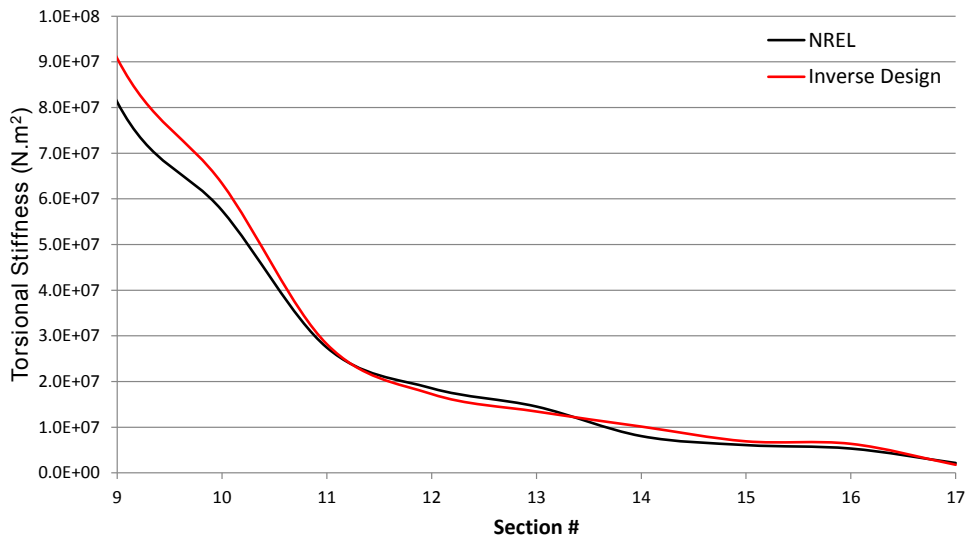

Figure 2.23: Variation of the torsional stiffness of the inverse designed blade and NREL blade between bection 9 - 17

densities of the NREL blade. Although the assigned mass densities in each section will not reflect the actual density of the material used in the inverse design, the mass property of the designed blade will match the mass property of NREL blade. Thus, after the adjustment of the blade mass density, final blade design can be used as a reference blade to study the effect of bending-twisting coupling on load alleviation.

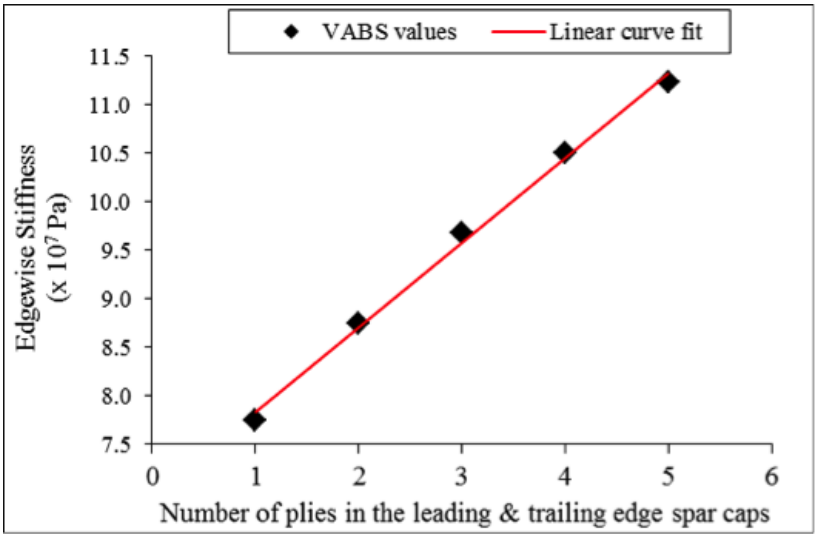

Figure 2.24: Variation of the torsional stiffness value of section 16 with the number of plies in the leading and trailing edge spar caps

Although the final baseline blade may not be a production blade, baseline blade provides a realistic stiffness and mass properties that nearly replicate the NREL's 5MW turbine blade. Following the initial inverse design of the blade, modifications are done in the ply numbers of certain sections. Ply numbers are adjusted in some sections in order to obtain decreasing number of plies in the airfoil sections from blade root to the blade tip. It should be noted that main aim of the modification of the inverse design of the blade is to obtain reasonable ply numbers in different sections of the blade. Since the inverse design blade has no core material, ply numbers are adjusted so as to obtain smooth ply drops with decreasing number of plies towards the tip of the blade. It should again be stressed that since the inverse designed blade is used as a reference blade to study the effect of bending-twisting coupling on load alleviation, exact match of the sectional beam properties of the inverse design blade and the NREL blade is not seeked for. Table 2.7 shows the sectional ply numbers of the initial inverse design blade. In the root section of the blade, total 47 plies including 31 zero degree plies and 16 ninety degree plies are used. Table 2.8 shows the sectional ply numbers of the modified inverse design blade with total 50 plies in root section including 34 zero degree plies and 16 ninety degree plies.

Table 2.7: Inverse design ply numbers between section 2 - 17

Section no	Zero Degree Plies				45/-45 Biax Plies	
	LE	Upper Spar	Lower Spar	TE	Main	Shear Web
2	90	60	60	90	16	16
3	116	32	39	85	6	6
4	40	120	120	40	10	6
5	40	125	140	40	4	6
6	37	120	125	42	4	6
7	40	130	140	40	6	6
8	49	165	182	36	6	6
9	40	119	119	45	4	6
10	33	119	115	37	4	6
11	30	50	50	36	2	4
12	18	52	52	19	2	2
13	18	40	37	14	2	2
14	9	20	20	9	2	2
15	4	17	15	3	2	2
16	20	22	22	10	2	2
17	1	4	1	1	4	2

Table 2.8: Modified inverse design ply numbers between section 2 - 17

Section no	Zero Degree Plies				45/-45 Biax Plies	
	LE	Upper Spar	Lower Spar	TE	Main	Shear Web
2	50	75	75	50	16	16
3	50	60	60	50	16	16
4	40	125	125	40	14	14
5	40	125	125	40	14	14
6	38	120	120	38	14	14
7	38	120	120	38	12	12
8	36	110	110	36	10	10
9	36	100	100	36	8	8
10	32	80	80	32	6	6
11	30	60	60	30	4	4
12	20	40	40	20	4	4
13	16	35	35	16	4	4
14	12	20	20	12	4	2
15	6	15	15	6	4	2
16	4	10	10	4	4	4
17	1	2	2	1	4	4

CHAPTER 3

SUPERELEMENT MODEL

The 3D finite element model of one blade consists of 65.000 elements. This is a quite large number for an analysis of a 3 bladed wind turbine model. Therefore, a method for reducing size of the finite element model is usually preferred in multibody simulation of wind turbine systems. The so-called reduced order models use much less elements then the 3D finite element model. There are many methods for reducing the size of a finite element. Guyan Reduction, Modal Decoupling and Craig-Bampton methods are the best known methods. Although Craig-Bampton method is similar to other methods, it accounts for both mass and stiffness (unlike Guyan Method) and it allows for different boundary conditions at interfaces (unlike modal decoupling).

The Mecano solver [3] of the Samcef Field [1] and Samcef Wind Turbine [2] is capable of creating the nonlinear super element of a 3D finite element model which is based on the Craig Bampton method (component mode method) [28]. Nonlinearities arise from the fact that its formulation allows modeling substructures undergoing large displacements/rotations in space, with the only limitation that the strains must remain infinitesimal in the body frame. Behaviour of the super element in the local frame is described as a combination of two types of modes, namely the constrained modes and the normal vibration modes of the substructure. The static deformed shapes are determined by giving a unit displacement to each boundary degree of freedom, whereas the remaining boundary degrees of freedom are fixed. The dynamic deformed shapes correspond to the vibration modes obtained by clamping the substructure on its boundary. The behaviour of the super element is assumed to be represented by superimposing to the set

of static deformed shape modes by a small number of dynamic deformed shape modes, since the lower frequency dynamic behaviour of the substructure is presented with sufficient accuracy by keeping only a few vibration modes. The resulting reduced mass and stiffness matrices of the super element are based on the above assumptions.

In the thesis study, in order to appropriately account for the effect of off-axis plies on the bending-twisting coupling potential, dynamic superelement of the blade of the5 MW NREL wind turbine is created and introduced into the multi-body dynamic model of the wind turbine system. Dynamic superelement of the turbine blade is created utilizing the finite element model of the three-dimensional blade structure, which is obtained through an inverse design process. It is considered that the final 3D blade design can be used to build higher fidelity structural finite element models to be used as reference blade models in the study of the effect of bending-twisting coupling on the load alleviation in wind turbine systems.

Dynamic superelement of the blade is created in Samcef Field [1] and introduced into the wind turbine model created in Samcef Wind Turbine [2] which is a flexible multi-body dynamic code specialized for wind turbine systems.

3.1 Theory of Craig-Bampton Method

In the Craig-Bampton method used in dynamic analysis, the first step is to split the whole structure into a certain number of substructures. There are two types of component modes to describe the behavior of each substructure: the constrained modes (static deformed shape) and the normal vibration modes of the substructure (dynamic deformed shape). These component modes are determined by means of the undamped dynamic equations of the free substructure given below. The degrees of freedom are classified either as boundary degrees of freedom, shared by several substructures or as internal degrees of freedom, belonging only to the considered substructure. When all other boundary degrees of freedom being fixed, a unit displacement is successively assigned to each boundary degree of freedom to determine the constrained modes. The normal modes

correspond to the vibration modes are obtained by clamping the substructure at its boundary. Since by retaining only the low-frequency vibration modes, the substructure's dynamic deformed shape is represented with sufficient accuracy, it is assumed that the behavior of the substructure in the global system can be represented by superimposing the constrained modes and a small number of normal vibration modes. Thus, the reduced mass matrice of the substructure can be constructed.

Considering the undamped dynamic equations of each free-free substructure, the following expression [3] [47] can be written:

$$\begin{bmatrix} M_{FF} & M_{FI} \\ M_{IF} & M_{II} \end{bmatrix} \begin{bmatrix} \ddot{q_F} \\ \ddot{q_I} \end{bmatrix} + \begin{bmatrix} K_{FF} & K_{FI} \\ K_{IF} & K_{II} \end{bmatrix} \begin{bmatrix} q_F \\ q_I \end{bmatrix} = 0 \tag{3.1}$$

where q_F represents the boundary DOFs and q_I represent the internal DOFs. The mass and stiffness matrices are symmetrical.

The constrained modes are obtained by successively producing a unit displacement of each boundary degree of freedom while maintaining all other boundary degrees of freedom fixed and the internal degrees of freedom unloaded and unconstrained. Then equation 3.1 following applies:

$$\begin{bmatrix} K_{FF} & K_{FI} \\ K_{IF} & K_{II} \end{bmatrix} \begin{bmatrix} q_F \\ q_I \end{bmatrix} = \begin{bmatrix} F_F \\ 0 \end{bmatrix} \tag{3.2}$$

where

$$q_I = K_{II}^{-1} K_{IF} q_F = \phi_c q_F \tag{3.3}$$

The constrained modes (static deformed shape) are given by:

$$\begin{bmatrix} q_F \\ q_I \end{bmatrix} = \begin{bmatrix} I \\ \phi_c \end{bmatrix} q_F \tag{3.4}$$

The normal vibration modes are obtained by giving zero values to the boundary

degrees of freedom in equation 3.1 and by solving the eigenvalue problem of the substructure which is clamped around its contour.

$$\left[K_{II} - \omega^2 M_{II}\right] q_I = 0 \tag{3.5}$$

The obtained eigenvectors are the normal modes of the substructure. The set of retained low-frequency modes constitutes the modal matrix f_N.
For the normal modes, we have:

$$\begin{bmatrix} q_F \\ q_I \end{bmatrix} = \begin{bmatrix} 0 \\ \phi_N \end{bmatrix} P \tag{3.6}$$

where P represents the intensity vector of the retained normal modes.
Combining equation 3.4 and equation 3.6, the below matrix, which allows the passage from the basis constituted by the boundary degrees of freedom of the substructure to the basis constituted by the boundary degrees of freedom and the intensities of the retained normal modes.

$$\begin{bmatrix} q_F \\ q_I \end{bmatrix} = \begin{bmatrix} I & 0 \\ \phi_c & \phi_N \end{bmatrix} \begin{bmatrix} q_F \\ P \end{bmatrix} \tag{3.7}$$

$$M\ddot{q} + Kq = F \tag{3.8}$$

where M is the mass matrix, K is the stiffness matrix, F represents the external forces applied to the substructure.
The matrices are reduced considering the expression of kinetic energies and strain energies. The kinetic energy can be written as follows:

$$T = \frac{1}{2} \begin{bmatrix} \dot{q_F} & \dot{q_I} \end{bmatrix}^T \begin{bmatrix} M_{FF} & M_{FI} \\ M_{IF} & M_{II} \end{bmatrix} \begin{bmatrix} \dot{q_F} \\ \dot{q_I} \end{bmatrix} \tag{3.9}$$

or performing the basis transformation:

$$T = \frac{1}{2}\begin{bmatrix}\dot{q_F} & \dot{P}\end{bmatrix}^T \begin{bmatrix} I & \phi_c^T \\ 0 & \phi_N^T \end{bmatrix} \begin{bmatrix} M_{FF} & M_{FI} \\ M_{IF} & M_{II} \end{bmatrix} \begin{bmatrix} I & 0 \\ \phi_c & \phi_N \end{bmatrix} \begin{bmatrix} \dot{q_F} \\ \dot{q_I} \end{bmatrix} \tag{3.10}$$

or

$$T = \frac{1}{2}\begin{bmatrix}\dot{q_F} & \dot{P}\end{bmatrix}^T \begin{bmatrix} \overline{M}_{FF} & \overline{M}_{FI} \\ \overline{M}_{IF} & \overline{M}_{II} \end{bmatrix} \begin{bmatrix} \dot{q_F} \\ \dot{P} \end{bmatrix} \tag{3.11}$$

where the components of the reduced matrices are given by:

$$\overline{M}_{FF} = M_{FF} - M_{FI}K_{II}^{-1}K_{IF} - K_{FI}K_{II}^{-1}M_{IF} + K_{FI}K_{II}^{-1}M_{II}K_{II}^{-1}K_{IF} \tag{3.12}$$

$$\overline{M}_{FI} = \overline{M}_{IF}^T = M_{FI}\phi_N - K_{FI}K_{II}^{-1}M_{II}\phi_N \tag{3.13}$$

$$\overline{M}_{II} = \phi_N^T M_{II}\phi_N \tag{3.14}$$

Likewise, the strain energy can be written as:

$$V = \frac{1}{2}\begin{bmatrix}q_F & q_I\end{bmatrix}^T \begin{bmatrix} K_{FF} & K_{FI} \\ K_{IF} & K_{II} \end{bmatrix} \begin{bmatrix} q_F \\ q_I \end{bmatrix} \tag{3.15}$$

Equation equation 3.151 can further be written as:

$$V = \frac{1}{2}\begin{bmatrix}q_F & P\end{bmatrix}^T \begin{bmatrix} \overline{K}_{FF} & 0 \\ 0 & \overline{K}_{II} \end{bmatrix} \begin{bmatrix} q_F \\ P \end{bmatrix} \tag{3.16}$$

where

$$\overline{K}_{FF} = K_{FF} - K_{FI}K_{II}^{-1}K_{IF} \tag{3.17}$$

$$\overline{K}_{II} = \phi_N^T K_{II}\phi_N \tag{3.18}$$

Finally, the forces applied to the substructure are reduced using the principle of virtual work. If dW is the variation of virtual work caused by the arbitrary virtual displacement dq, then one can express dW as :

$$\begin{bmatrix} F_F^T & F_I^T \end{bmatrix} \begin{bmatrix} dq_F \\ dq_I \end{bmatrix} = \begin{bmatrix} P_F^T & P_p^T \end{bmatrix} \begin{bmatrix} dq_F \\ dP \end{bmatrix} \tag{3.19}$$

where F_F, F_I represent the components of the force vector applied to q_F and q_I respectively.

It was previously shown that equation 3.20 applies

$$\begin{bmatrix} dq_F \\ dq_I \end{bmatrix} = \begin{bmatrix} I & \phi_c^T \\ 0 & \phi_N^T \end{bmatrix} \begin{bmatrix} dq_F \\ dP \end{bmatrix} \tag{3.20}$$

Utilizing equation 3.20, it can be deduced that equation 3.21 holds.

$$\begin{bmatrix} P_F \\ P_p \end{bmatrix} = \begin{bmatrix} I & \phi_c^T \\ 0 & \phi_N^T \end{bmatrix} \begin{bmatrix} F_F \\ F_I \end{bmatrix} \tag{3.21}$$

The substructure is thus described by the system:

$$\overline{M}\ddot{q} + \overline{K}q = \overline{F} \tag{3.22}$$

3.2 Finite Element Model of the Blade

The 3D finite element model of the blade is needed to generate the superelement model of the blade. For this purpose, first the 3D CAD drawing of the blade is imported into Samcef Field [1]. In 3D CAD model, the surfaces of the sections are split to assign different composite layers. In addition, the retained nodes are connected to the surfaces of related sections. The orientation of the model is also critical while importing superelement model to Samcef Wind Turbine. The [0,0,0] point must be at the middle of the cylindrical root section of the blade, and the span of the blade must be along the positive z axis. The y axis must

be along to chordwise direction of the zero twist cross section and its positive value must be towards to trailing edge of the cross section. Figure 3.1 shows the blade coordinate system on the blade sections.

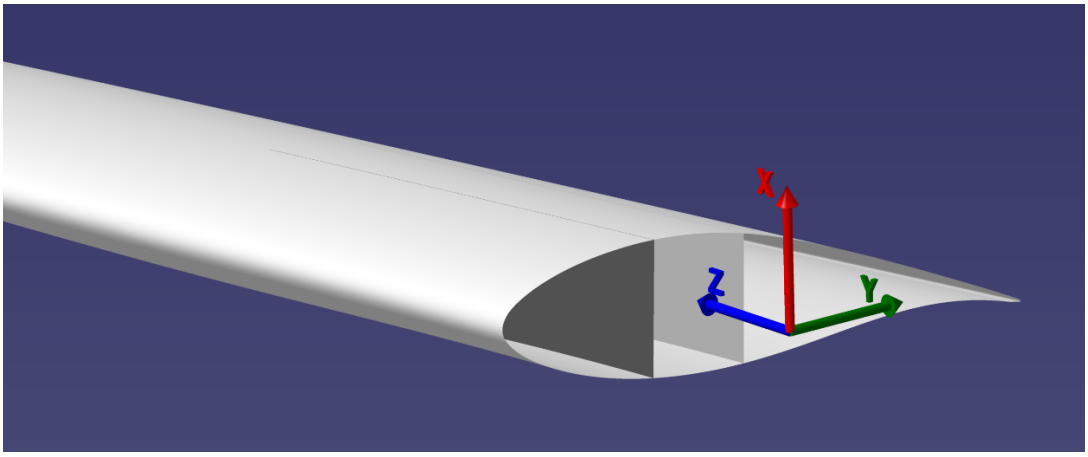

Figure 3.1: Blade coordinate system defined in Samcef, y axis is along the chord, z axis is along the span

Figure 3.2 shows the 3D CAD model of the blade in Samcef Field with the highlighted middle spar cap regions. The split surfaces can also be seen in the figure. Secondly, the composite materials and the composite layers of the sections are defined. Figure 3.3 shows the properties of the glass fiber composite material used in the blade structure and the Figure 3.4 shows the layer definition in the root section of the blade.Then, the composite layers are assigned to the structure according to the layer numbers coming from inverse design. Since the layers are defined with the definition of "at the top of the support" selection, when the layers are assigned on the surfaces of the blade, the normal of the surfaces have to be towards inside of the blade as shown in Figure 3.5.

To define the reduced structure, retained nodes are generated along the spanwise direction of the blade structure. In the present design, total of 18 retained nodes are defined for the reduced order model of the blade structure. Figure 3.6 shows the spanwise location of the retained nodes of the blade structure. First retained node is created at the root of the blade. This node is also connection point between the hub and the blade. Retained nodes are located at the aerodynamic center of the cross-sections.

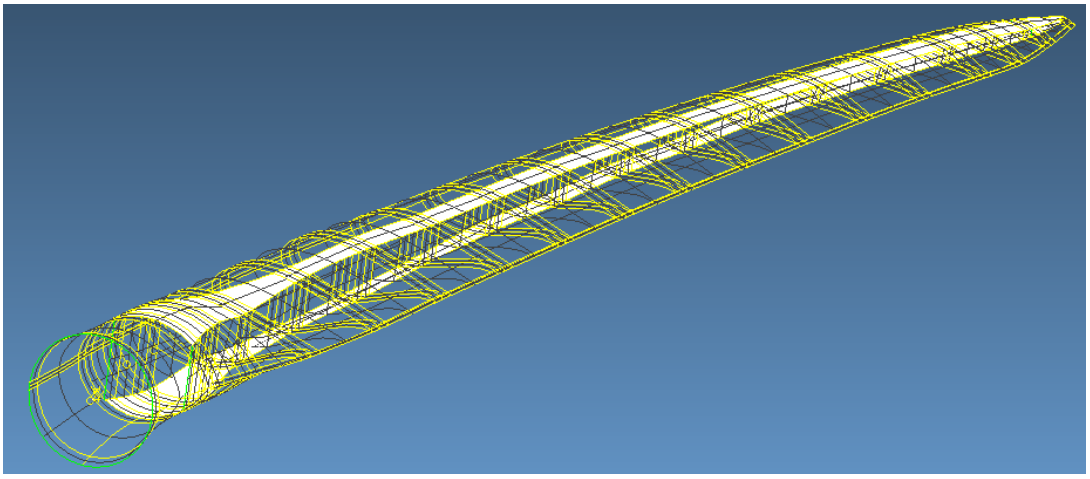

Figure 3.2: 3D blade model in Samcef Field with highlighted middle sparcap region

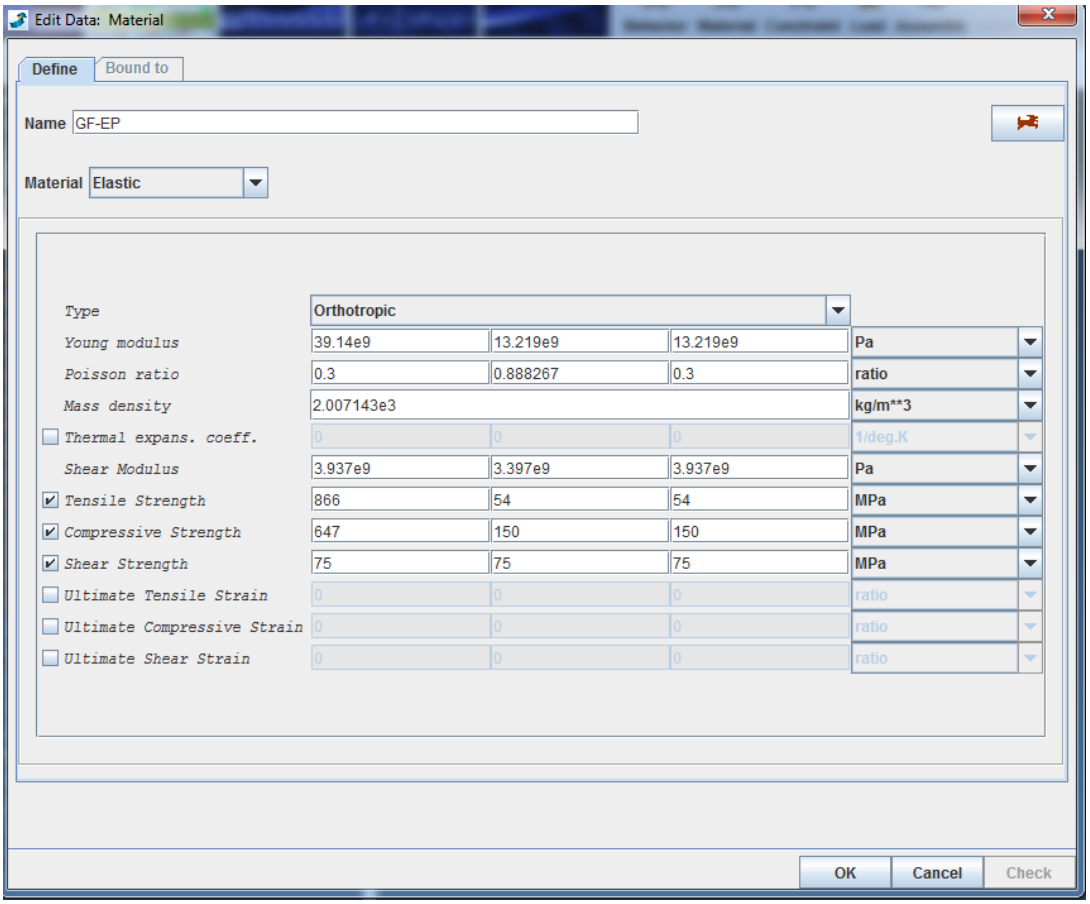

Figure 3.3: Definition of the properties of the GF composite material in Samcef Field

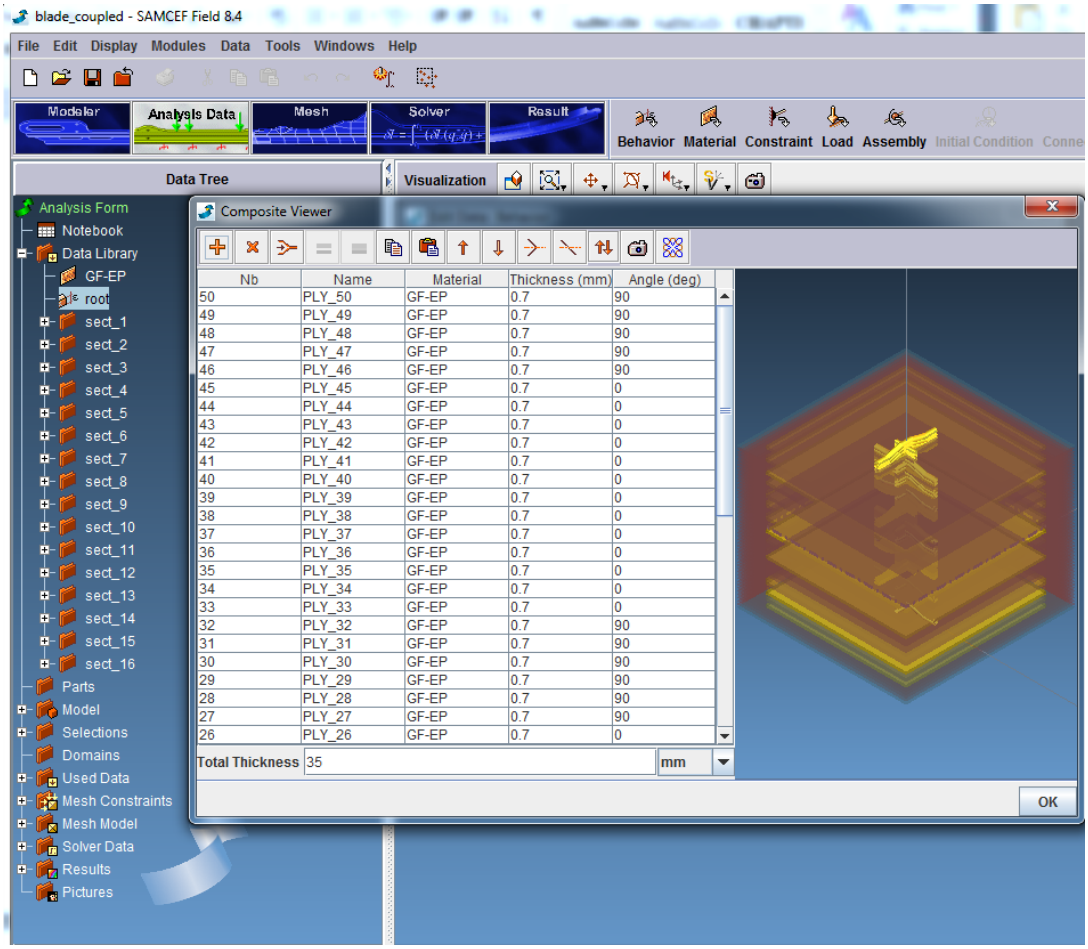

Figure 3.4: Layer definition of the root section of the blade in Samcef Field

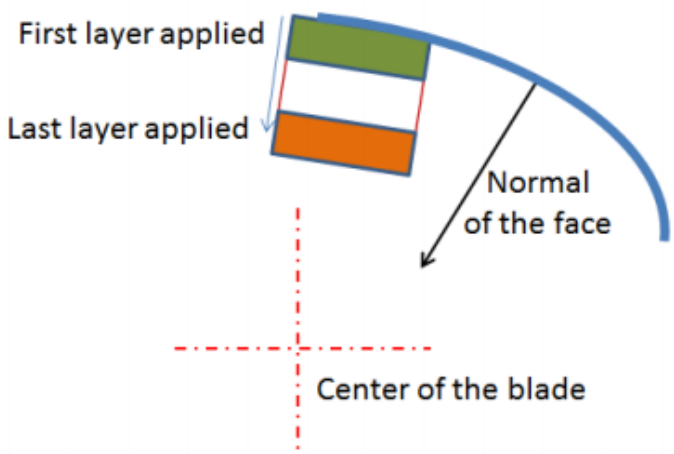

Figure 3.5: The normal of the surfaces have to be towards inside of the blade for a correct stacking sequence

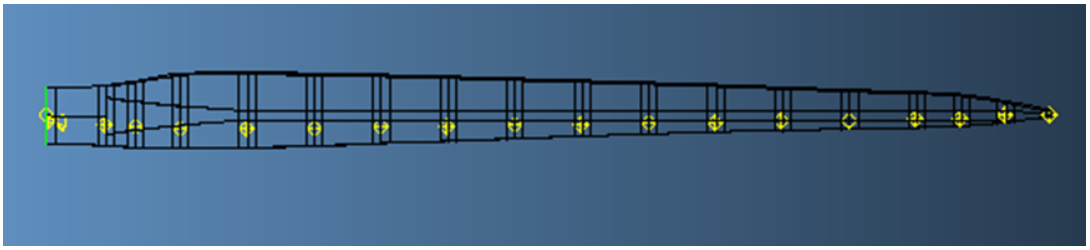

Figure 3.6: Spanwise locations of the retained nodes on the blade FE model

Figure 3.7 describes the main steps of generating the super element of the blade. The initial step in creating the super element of the blade is to import the CAD drawing of the blade as a shell structure. In the present study, the CAD model of the blade is generated in CATIA environment and then exported to Samcef Field using the Step format. For super element generation, for each selected cross section, a retained node must be created at the %25 chord of the blade measured. Once the super element of the blade is imported into the multi-body model of the wind turbine system, retained nodes are used for applying external loads on the turbine blade. Retained nodes are also used as the connector nodes of the blade to the wind turbine system through the rotor hub. Therefore, at the root section retained node is created at the center of the circular cross-section. This node is also used as the pitch axis location through which the controller in the multi-body model of the wind turbine system controls the rotation of the blade about the pitch axis. In the next step, composite materials to be used in the blade structure are defined, and composite lay-up assignments are made to each face of each section of the blade. In the example blade shown in Figure 3.7, there are 20 faces in each section of the blade. Twenty faces are composed of trailing and leading edge faces, two unified spar caps between the shear webs, two shear webs and four faces between the spar caps and the leading and the trailing edge faces. Retained node in a section is placed at the center of the section in the spanwise direction, and ten of these faces are at the inboard section of the retained node and the remaining ten faces are at the outboard of the retained node. Figure 3.7b shows the upper and lower spar cap regions along the whole span of the blade. In the third step of the superelement generation, a link must be established between the retained nodes

in each section and faces of the corresponding section, as shown in Figure 3.7c. Retained nodes are tied to nearby faces which are generated at the inboard and outboard of the retained node. In the thesis, the connection between the faces and the retained nodes is established by mean elements. By the use of mean elements, mean displacement of the structure is assigned to the retained node. A vital step in the generation of the super element is to assign the correct displacement boundary conditions to the retained node at the root of the blade which connects the blade to the rotor hub in the wind turbine system. At this node, a free rotation about pitch axis must be defined to allow for the pitch motion of the blade in the multi-body simulation of the wind turbine system. As the final step of superelement generation, the finite element mesh is generated on the all faces of the blade structure including the retaining nodes, as shown in Figure 3.7d and the dynamic superelement of the blade is generated.

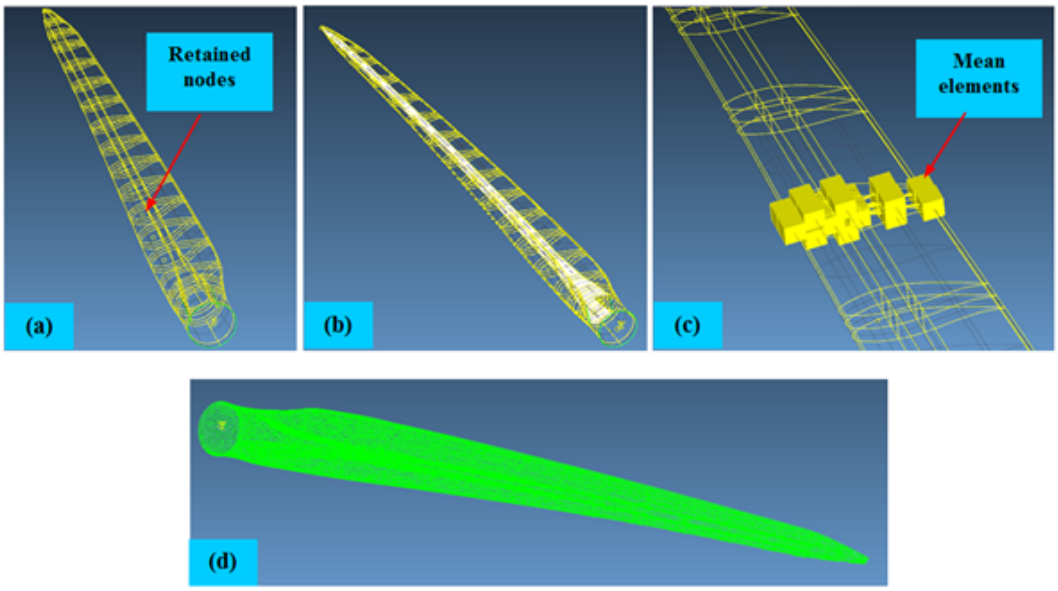

Figure 3.7: Generation of the dynamic superelement of the wind turbine blade **(a)** CAD model of the blade and generation of retained nodes **(b)** Assigning composite material to the faces of the blade **(c)** Connection of the retained node to faces of the related blade section by mean elements **(d)** Finite element mesh of the blade structure

Now, the finite element mesh of the structure can be generated. The meshes of the retained nodes are simple since they are dimensionless. On the other hand, another issue arises about element size of the mesh of the blade. The best way to

determine the optimal mesh size is trial and error method. Therefore different element sizes are compared with respect to the natural frequencies of the 3D model and the best element size is determined. Average length of one side of the element is selected as 200 mm. The comparison of the different element sizes is shown at Table 3.1.

Last step of the superelement generation process is to determine the analysis parameters. The type of the super-element is selected as "Dynamic" and the number of Eigenvalues is 20. Although only few frequencies are enough for a rotor blade, it is recommended to use 20 eigenvalues for dynamic superelement of the blades. Then the superelement generation run is started.

3.2.1 Superelement Blade Verification

The validation of the superelement blades are done by comparing the natural frequencies of the 3D blade and superelement blades. First five natural frequency of the blade is determined to be enough for comparison. The first retained node of the superelement blade is clamped in the modal analysis. Hence, for the 3D blade model, the surfaces which are assembled to the first retained node are also clamped in the modal analysis. Table 3.1 shows the results modal analysis results. The second column of the table shows the modal results of the finest mesh(element size is 150 mm) superelement blade. The third column of the table shows the results of the fine mesh results (200 mm element size) and the fourth column shows the course mesh results (300 mm element size). As seen from the Table 3.1, good agreement exists between the natural frequencies obtained by the 3D finite element model and super element of the blade with fine mesh. This indicates that the super element of the blade represents the stiffness and mass distribution of the 3D blade accurately, and it can be used in the multi-body model of the wind turbine system with confidence. It should be noted that in the present study no attempt is made to match the mass properties of the turbine blade with the mass properties of NREL blade [27].

Therefore, the superelement blade with fine mesh is selected to be used in multi-body simulation analysis of the wind turbine system. Figure 3.8 - 3.9 shows the

Table 3.1: Comparison of first five frequencies of the turbine blade clamped at the root

Modes	Finest Mesh (150 mm) [Hz]	Fine Mesh (200 mm) [Hz]	Course Mesh (300 mm) [Hz]	3D FE Model
1	0.732	0.732	0.732	0.732
2	1.134	1.134	1.141	1.134
3	1.887	1.888	1.888	1.883
4	3.469	3.488	3.538	3.474
5	3.651	3.655	3.696	3.644

fine mesh on the blade structures from different positions. Figure 3.11 shows the first five mode shapes of the blade structure.

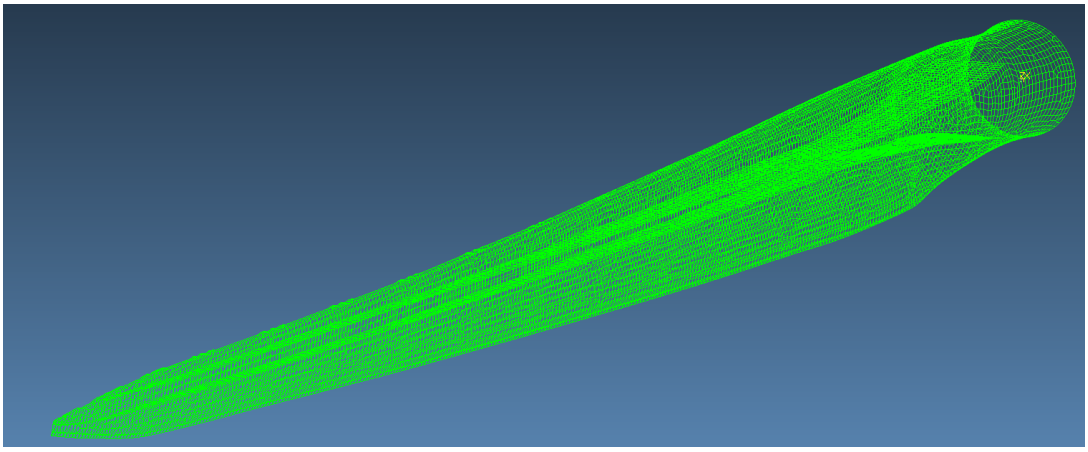

Figure 3.8: Global view of the blade structure with fine mesh

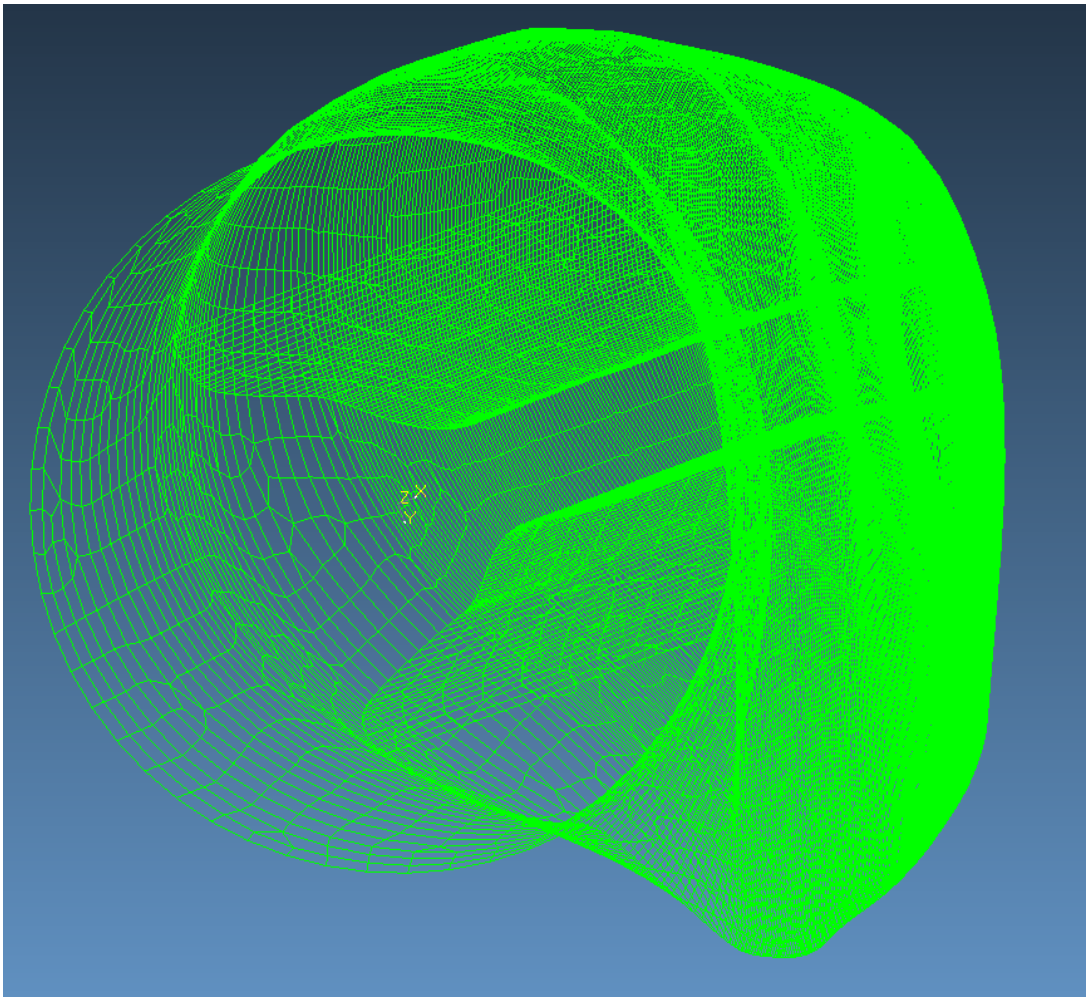

Figure 3.9: Fine mesh view from the root of the blade with mesh on the shear web structures

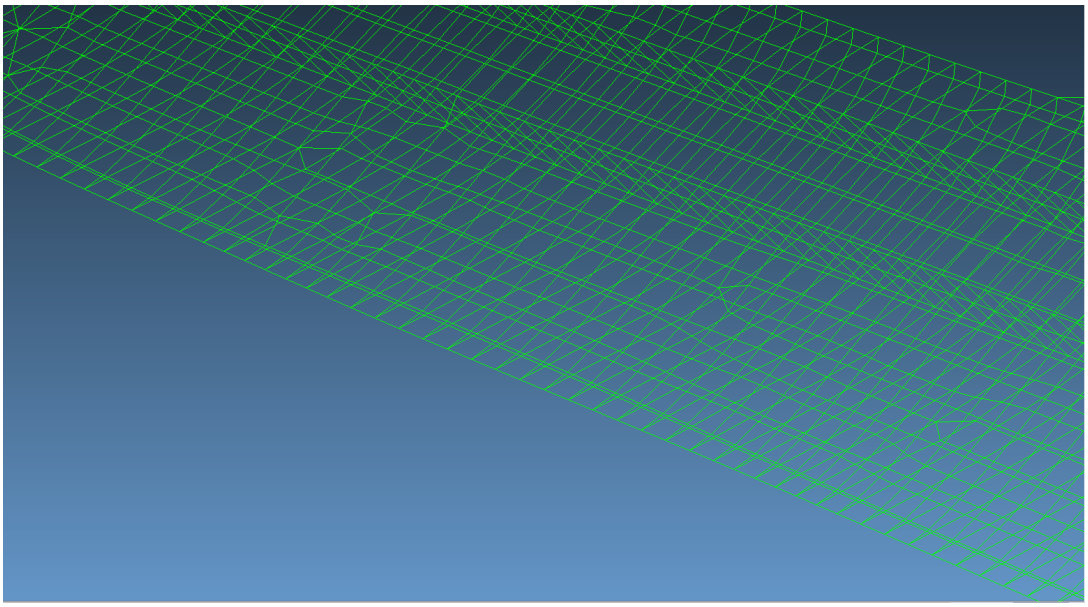

Figure 3.10: Fine mesh view on the spar cap region of the blade

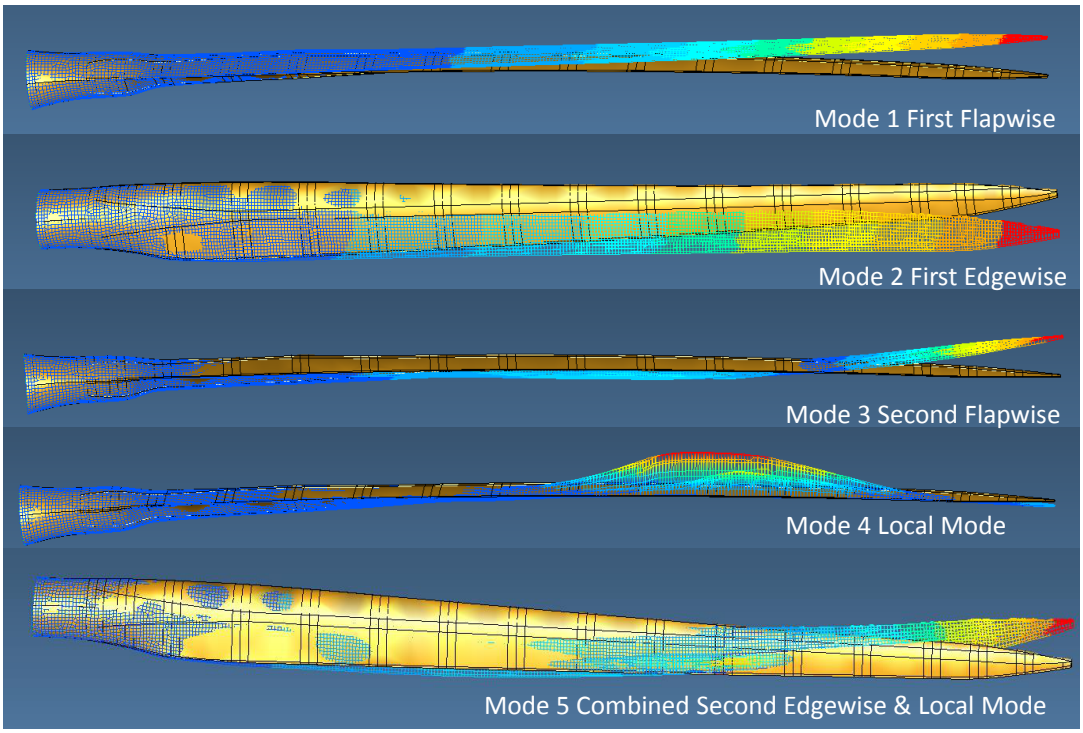

Figure 3.11: First five mode shapes of the blade which are calculated for comparison of different mesh sizes

CHAPTER 4

MULTIBODY SIMULATION OF THE WIND TURBINE SYSTEM AND CALCULATION OF DAMAGE EQUIVALENT LOADS

The multibody simulation of the wind turbine system is created in Samcef Wind Turbine (SWT) [2], which is specific software for wind turbine analysis. In Samcef Wind Turbine, it is possible to generate a realistic wind turbine model which has all components of a conventional wind turbine including the controller. A conventional wind turbine consist of a tower, a bedplate, 3 blades, a hub, a low speed shaft, main bearings of the low speed shaft, a gearbox, a high speed shaft, a generator and a controller. SWT is capable of solving transient aeroelastic equations of the wind turbine system. The aerodynamic solver of the software is based on BEM theory [10] with typical corrections such as tip and hub losses, tower shadow, and deactivation of induction factors at low tip speed ratios. It also has built-in semi-empirical sub-models to treat unsteady aerodynamics with higher accuracy. Specifically, SWT has wake sub-model, skewed flow correction sub-model and dynamic stall sub-models which is of Beddoes-Leishman type [20]. The controller is integrated to the wind turbine model in the SWT by means of dynamic link library which can be used for typical wind turbine simulations. Multi-body simulation of the wind turbine system is performed by the implicit non-linear finite element solver Samcef Mecano [3] which has the ability to allow the use of multi-body simulation features, such as kinematic joints etc., inside real finite elements models. Transient simulations are performed in time domain taking into account the structural, multibody, aerodynamic and control features

in a fully non-linear dynamic way with strong coupling. The main non-linear features are present in the aerodynamics, in the controller and in structural and multi-body elements such as non-linear stiffness, large rotations, bearing gaps etc. [2].

4.1 General Properties of Wind Turbine Model

To study the effect of bending twisting coupling on the load alleviation in the wind turbine system, a 5 MW multi-body wind turbine model is created in Samcef Wind Turbine. For realistic and reliable computation of the internal loads in the wind turbine system, several sub-structures, including the controller, must be present in the multi-body model of the turbine. For the parameters of the 5 MW wind turbine, known properties of NREL's 5 MW turbine [27] is taken as the reference. The wind turbine model that is used in the multibody simulations is composed of 3 prebent superelement blades, an external 5MW controller, simple model of tower and standard models of bedplate, gearbox, rotor shaft, coupling shaft and the generator which are available in the SWT. The rated speed of the wind turbine is 11.4 m/s and rated rotational speed of the rotor is 12 rpm. The standard gearbox selected has two planetary and one parallel gear stages. The rotor has a 5^0 tilt angle and together with the prebent in the blades, it is aimed to prevent possible blade tower collision during the operation of the wind turbine. The global coordinate frame x-y-z for the wind turbine system is shown in Figure 4.1. The origin of the fixed global coordinate frame is located at the top of the tower where tower connects to the bedplate. In the global frame, x axis is parallel to the rotor axis and points downwind, z axis is the vertical axis perpendicular to the rotor axis and points towards the sky, and y axis is perpendicular to both x and z axes.

Figure 4.2 shows the tower foundation coordinate system of the wind turbine. In this thesis, tower foundation coordinate system is used as axis system about which the forces and the moments on the yaw drive-bedplate connection are calculated. Table 4.1 shows the main wind turbine properties used in the multi-body simulation of the wind turbine system. In order to reduce the risk of

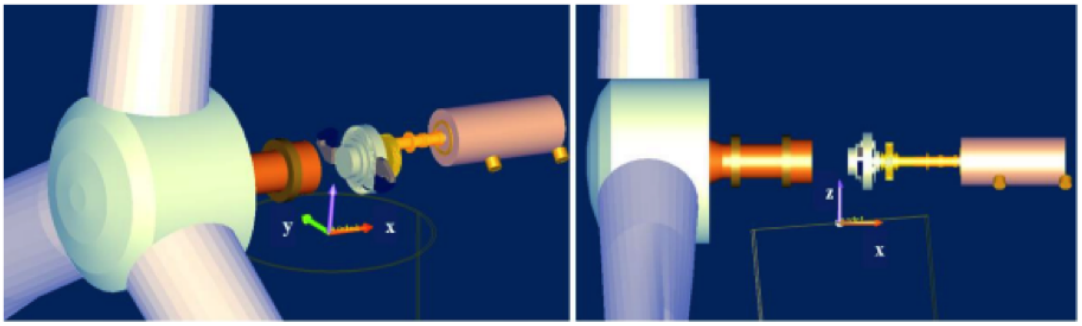

Figure 4.1: Global coordinate system used in wind turbine analysis

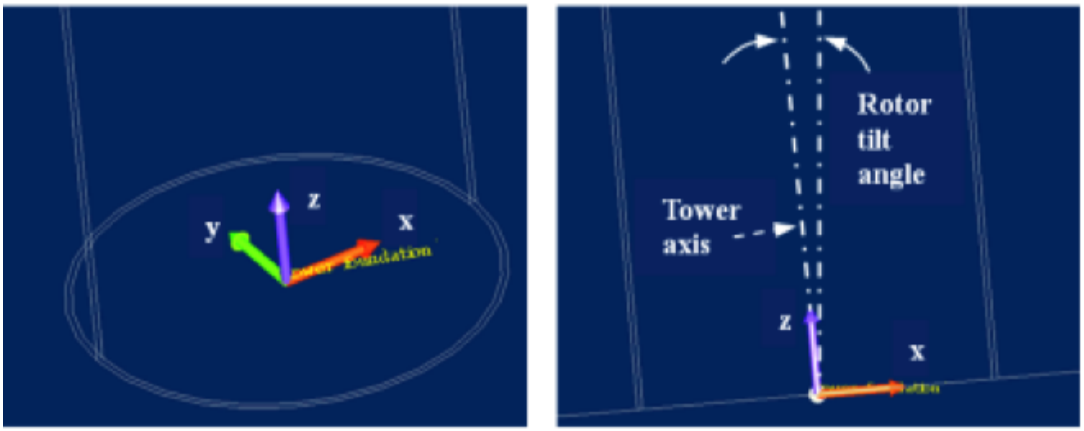

Figure 4.2: Tower coordinate system used in wind turbine analysis

blade-tower collision, a 4 meters blade tip prebent is also created in the blade solid model and superelement of the blade is created for the prebent blade.

4.1.1 Wind Turbine Blades

In the thesis study, six blade configurations are used in the multibody simulation of the wind turbine system. One of them is modeled as non-linear beam in Samcef Wind Turbine. Other blades are superelement blades which are imported to the SWT for the transient aeroelastic analysis of the wind turbine system. Table 4.2 shows the properties of the blades. All blades are geometrically same and their length is 61.5 meters. Baseline blade is taken as the superelement blade with full GFRP material with 0 degree fiber orientation in the spar caps. Zero degree orientation is defined as the axis which traverses the blade from blade

Table 4.1: Main properties of the wind turbine system defined in SWT

Nominal Power	5 MW
Number of Blades	3
Blade prebent at the tip	4 m
Control	Pitch, variable speed
Rated rotor speed	12 rpm
Gearbox ratio	105
Rotor/Hub Diameter	126 m / 4 m
Hub length	4 m
Blade length	61.5 m
Rotor conicity	0 degree
Rotor tilt angle	5 degree
Tower centerline elevation	100 m
Hub mass	50,000 kg

root to the blade tip through the middle of the spar caps. Transient aeroelastic analysis of the complete wind turbine system is performed for different spar cap configurations corresponding to the baseline zero degree and 15 degree off-axis ply angles. To induce bending-twisting coupling, GFRP and CFRP are used as the ply material in an off-axis configuration in the spar caps. Before the transient aeroelastic analysis, dynamic superelements of the blades are generated for blades with zero degree and 15 degree off-axis spar cap ply angle definitions. Off-axis plies are placed in the main spar caps in the 30 m of the blade measured from the blade tip.

Before the study of the effect of bending-twisting coupling on the loads acting on the wind turbine, a comparative study is conducted on the performance of the wind turbines which have blades defined as superelement and geometrically nonlinear beams in SWT. This study is performed in order to infer conclusions with regard to the appropriateness of the use of superelement blade definition in the transient analysis of the 5MW wind turbine system that is set up in the present study. For this purpose, two separate wind turbine models are generated in SWT. Except for the blades, both wind turbine models have the same sub-components. In both wind turbine models, blades are defined as bladed-rotor in SWT with pressure/suction side and leading/trailing edge spar caps having

Table 4.2: Blade configurations used in the analyses, first one is beam model and others are superelement models

No	Blade Model	Material and Ply Angles in the Main Spar Caps in the 30 m of the blade measured from the blade tip
1	Non-linear Beam Model	0 degree GFRP
2	Superelement Model	0 degree GFRP(Baseline blade)
3	Superelement Model	15 degree GFRP
4	Superelement Model	15 degree CFRP
5	Superelement Model	Mixed 15–0 degree GFRP
6	Superelement Model	Mixed 15–0 degree GFRP
7	Superelement Model	Stiff 15 degree CFRP

unidirectional GFRP layers all aligned with the blade axis. In this respect, blade configuration used in the comparative study has the lowest coupling stiffness. One of the wind turbine models is established by introducing the superelement of the blade, which is inverse designed, as the bladed-rotor definition in SWT. In the second wind turbine model, bladed-rotor is defined as geometrically nonlinear beam. The sectional beam properties of the beam blade are taken from the output of the variational asymptotic beam sectional analysis performed by VABS in the inverse design process of the reference blade. It should be noted that in SWT coupling stiffness are not included in the beam formulation. Therefore, blade defined as geometrically nonlinear beam only has major stiffness; flapwise, edgewise and torsional. On the other hand, superelement blade possesses the whole coupling effects with the only limitation that with respect to the local frame fixed to the blade, blade behaves geometrically linear. Inverse design of the baseline blade is described in Chapter 3. In the iterative inverse design process, sectional beam properties of the baseline blade are compared with the known beam properties of the blade of NREL's 5 MW wind turbine system [27] until an acceptable differences between the sectional beam properties of the inverse designed blade and the known properties of of the blade of NREL's 5 MW wind turbine system is obtained for each section of the blade. It should be noted that coupling stiffness of the baseline superelement blade is mainly due

to the blade geometry, because baseline blade has all spar plies aligned along the blade span. Therefore, coupling stiffness values of the baseline superelement blade are much smaller than the coupling stiffness values of superelement blades that have off-axis spar cap plies.

In the design of blade number 3, all the ply orientations in the mid-spar cap regions of the 30 meters of the tip regions are changed to 15 degree. The fourth blade has carbon fiber in the main spar caps in the 30 m of the blade measured from the blade tip. For the fourth blade flapwise stiffness values are 5% higher than the flapwise stiffness of the third blade. Compared to the baseline blade 2 and the bend-twist coupled blade 3, the number of CFRP layers are reduced. Because the fourth blade has all of its main spar caps made of CFRP and the number of layers is less than the number of layers of the baseline blade 2 and bend-twist coupled GFRP blade 3,it is the lightest blade. Blades 5 and 6 have mixed 15 and 0 degree GFRP plies in their mid-spar caps of in the last 30 m of the span of the blade. Blade 5 has approximately 13% higher flapwise stiffness values in the blade sections of the last 30 m of the blade span compared to blade 3. On the other hand, blade 6 has approximately 18% higher flapwise stiffness values in the blade sections of the last 30 m of the blade span compared to blade 3. Main spar caps of the seventh blade in the last 30 m of the blade span are made of off-axis full carbon-epoxy material at 15 degree fiber orientation angle with respect to the blade axis. For the seventh blade number of off-axis CFRP layers is increased such that flapwise stiffness values of blade sections in the last 30 m of the blade span are approximately same as the flapwise stiffness values of the baseline blade. In this respect, the weight of blade 7 is higher than the weight of blades 4 due to the higher number of CFRP plies required to match the flapwise bending stiffness values of the baseline GFRP blade. Table 4.3 shows the flapwise stiffness values of the seven blades. Stiffness values are given for the blade sections in the last 30 meter of the blade span. Table 4.4 shows the bending-twisting coupling terms of the seven blades for tip sections in the last 30 m of the blade span.

Figure 4.3 shows the tip regions of the blades where the ply orientations of the mid spar cap sections are modified. As shown in the Figure 4.3, zero degree

Table 4.3: Flapwise stiffness values $[Nm^2]$ of the tip sections of the blades

Section No	Blade 1 and 2	Blade 3	Blade 4	Blade 5	Blade 6	Blade 7
10	3.22E8	2.34E8	2.50E8	2.62E8	2.88E8	3.22E8
11	2.12E8	1.52E8	1.59E8	1.71E8	1.79E8	2.11E8
12	1.02E8	7.58E7	7.94E7	8.42E7	8.90E7	1.03E8
13	7.28E7	5.42E7	5.56E7	6.08E7	6.39E7	7.27E7
14	3.90E7	2.97E7	3.08E7	3.34E7	3.50E7	3.78E7
15	2.41E7	1.86E7	1.73E7	2.10E7	2.18E7	2.36E7
16	1.33E7	1.09E7	1.17E7	1.21E7	1.26E7	1.38E7
17	4.36E6	3.85E6	5.12E6	4.13E6	4.13E6	5.12E6

Table 4.4: Bending twisting coupling values $[Nm^2]$ of the tip sections of the blades

Section No	Blade 1 and 2	Blade 3	Blade 4	Blade 5	Blade 6	Blade 7
10	-5.23E3	-2.18E7	-4.37E7	-1.62E7	-1.07E7	-4.52E7
11	-3.36E3	-1.29E7	-2.56E7	-9.86E6	-8.33E6	-2.66E7
12	-2.58E3	-9.43E6	-1.85E7	-7.37E6	-6.02E6	-1.97E7
13	-2.61E3	-7.31E6	-1.42E7	-5.51E6	-4.51E6	-1.53E7
14	-1.72E3	-5.17E6	-9.85E6	-3.76E6	-3.02E6	-1.07E7
15	-1.41E3	-3.59E6	-6.73E6	-2.51E6	-2.06E6	-8.15E6
16	-3.81E1	-2.80E6	-4.61E6	-1.74E6	-1.19E6	-5.31E6
17	-3.26E2	-1.09E6	-2.01E6	-5.51E5	-5.51E5	-2.01E6

plies are along span wise direction and modification of the off-axis ply angle configuration is done by turning the 0 degree spar cap plies towards to the leading edge.

Figure 4.4 (a) shows the blades on in the wind turbine model in the global view. Figure 4.4 (b)-(c) shows the tilt angle of the rotor and the prebent of the blades, respectively. All seven blades look same in the global model because there is no difference in their geometrical shape. In the present study, 4 meters pre-bent is given at the blade tips. Pre-bent and the tilt angle protect the blades from any

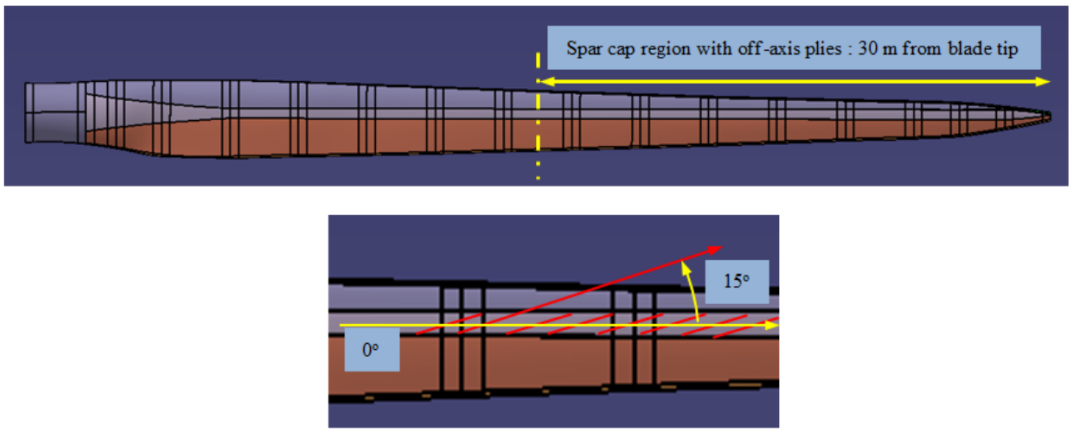

Figure 4.3: Spar cap regions of the blades with off-axis plies

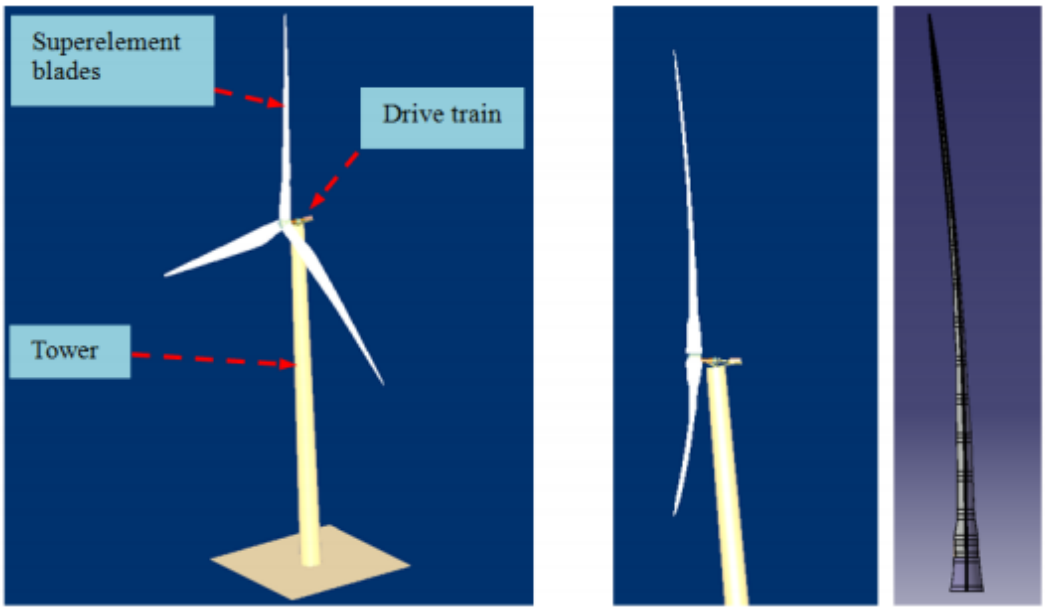

Figure 4.4: (a)Global view of wind turbine system (b)Tilt angle of rotor (c) Prebet of the blades

possibility of of the blades coming into contact with the tower.

4.1.2 External PID Controller

There is an external PID controller in the wind turbine system which is in "dll" format and run with a "dat" file which includes system properties and controller constatns. Since the main objective of the thesis is not developing a

controller for a wind turbine system with passive load control, the same controller is used for all blade configurations. The PID system involves three separate parameters: the proportional, the integral and the derivative gain, denoted as K_P, K_I, and K_D. They are considering an error signal, which is defined here as the difference between the measured speed and the rated speed of the rotor. Basically, the proportional gain determines the reaction to the current error, whereas the integral gain determines the reaction based on the sum of recent errors, finally the derivative gain determines the reaction based on the rate at which the error has been changing.
Thus, the inputs for the PID block definition are:

- K_P: proportional gain
- K_I: integrative gain
- K_D: derivative gain

The three different signals are then added together to give the instruction of the pitch angle that the pitch mechanism need to achieve. Figure 4.5 shows a simple model of PID, which is used in the control model of the wind turbine system.

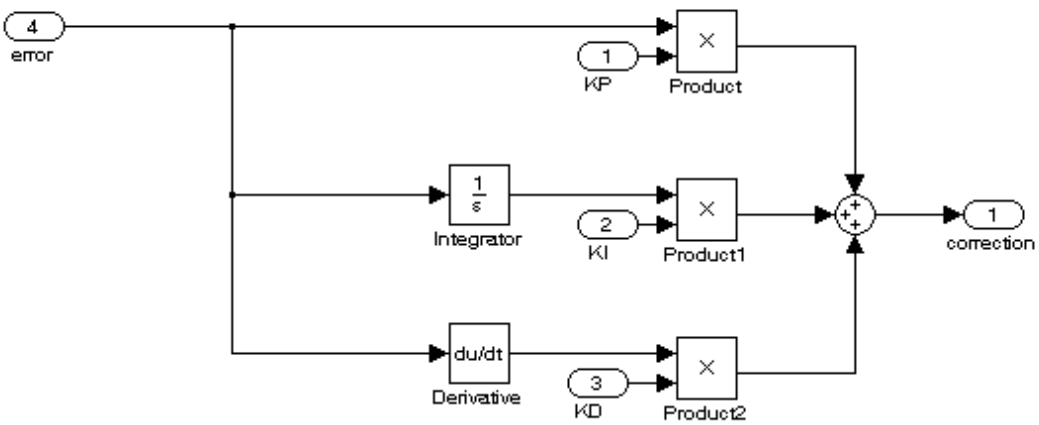

Figure 4.5: A simple PID scheme

Although a wind turbine system is a complex dynamic system, controllers do not have many variables as input and controlled variables. The controlled variables are:

- Blade pitch angles
- Yaw angle
- Generator torque
- Brake activation

4.1.3 Drive Train

Drive train includes most of the parts of the wind turbine system at the top of the tower. Connection of the drive train parts is very crucial for analysis. Figure 4.6 shows the drive train components and their location on the wind turbine system. Blades are attached to the rotor hub and rotate with it. The generator side of the rotor hub is connected to rotor shaft. It has 50 tons of mass and 4 m length. The rotor shaft transfers the torque and rotational speed coming from the hub to the gear box. There are two main bearings on the rotor shaft. These bearings support the shaft and also protect the gear box from undesired forces and moments. Bearings have 200e6 N/mm radial stiffness, 4e6 N/mm axial stiffness and 10 N/mm radial bending stiffness. The damping value of the bearings is 1e6 N/(m/s). These values are the default values used in SWT for the 5 MW wind turbine. Figure 4.7 shows the location of the two main bearings and their purpose. The rotor shaft is made from steel.

The gearbox increases the rotor speed coming from the low speed rotor shaft and transfers it to the high speed coupling shaft. The gearbox of the wind turbine system consists of two planetary stages and one helical stage. Figure 4.8 shows the three stages of it. The green one is the first planetary stage and on the rotor shaft side. The white planetary stage is at the middle and the yellow parallel helical stage is on the coupling shaft side. Each planetary stage has 3 planets, 1 sun and 1 fixed ring. As shown in Figure 4.9, planet carrier bearings are

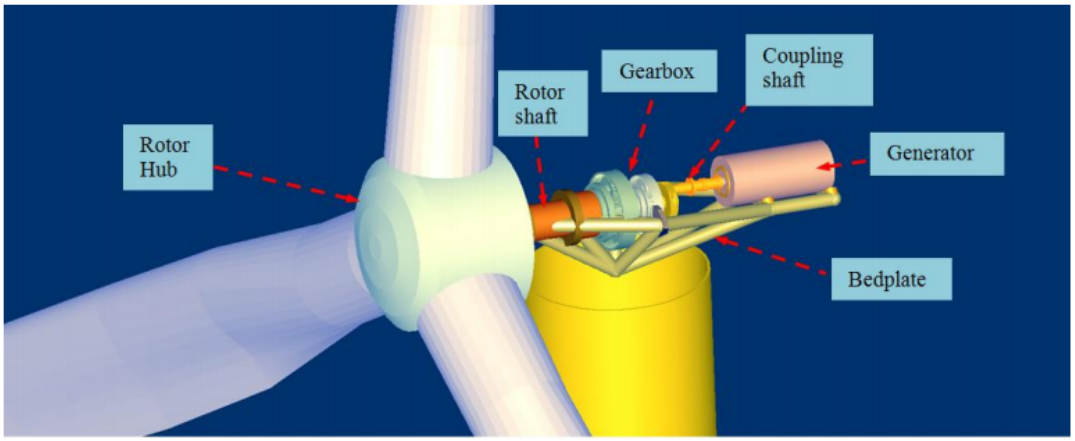

Figure 4.6: Location of drive train components on the wind turbine system

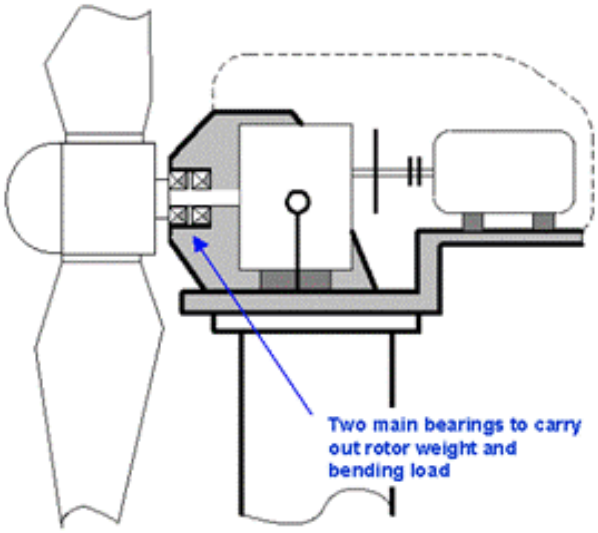

Figure 4.7: Rotor shaft bearing locations on the wind turbine system

the main bearings which support the two stages of planetary gears on the main shaft. The gearbox ratio is defined by entering the teeth number of the each stage. The Equation 4.1 shows the gear ratio calculation of planetary stages for a gear box which has "sun" as input, "planet carrier" as output and the "ring" as stationary part. The gear ratio of the helical stage is calculated by dividing the input teeth number to the output teeth number. For the gearbox selected for wind turbine simulations, Table 4.5 shows the gearbox ratio of the each stage and the total gearbox ratio is 105.

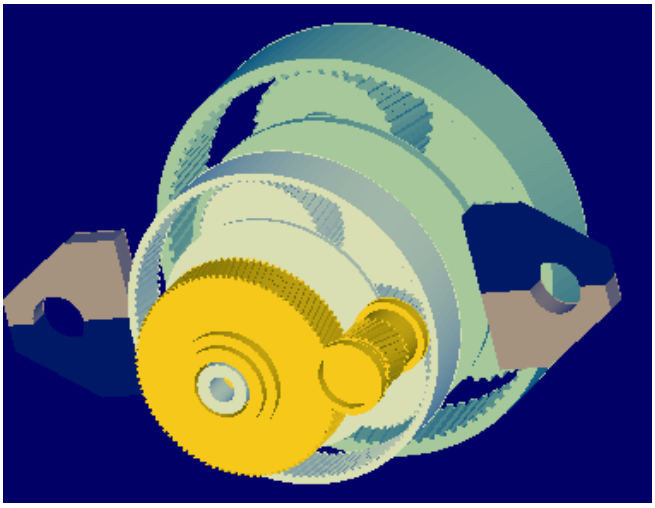

Figure 4.8: Three stages of the gearbox, yellow part is the helical stage and green parts are the planetary stages

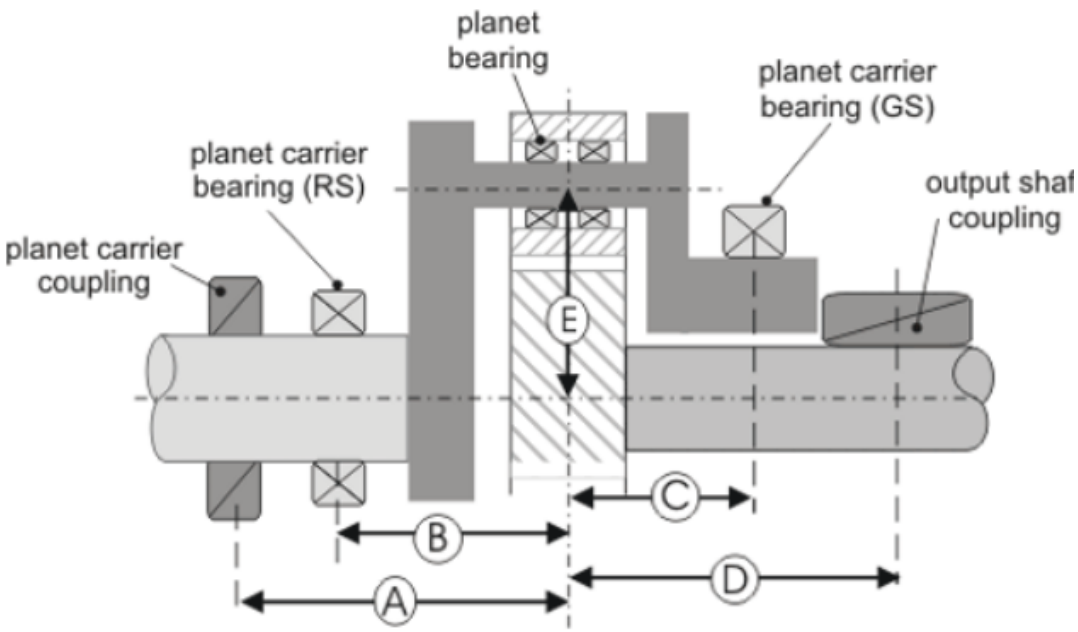

Figure 4.9: Planet carrier bearings of the gearbox

$$Gear\ Ratio = 1 + \frac{R}{S} \tag{4.1}$$

where:

R : ring teeth number

S : sun teeth number

Table 4.5: Gear ratio of the three stages of the gearbox

Stage	Input or Sun Teeth Number	Output or Ring Teeth Number	Gear Ratio
Stage 1 planetary	23	91	4.96
Stage 2 planetary	23	121	6.26
Stage 3 helical	98	29	3.38
Total gear ratio			105

The Standard High Speed Coupling Shaft extends from the gearbox to the generator. It consists of the brake, the slip coupling, the elastic coupling and the shaft itself. Figure 4.10 shows the main parts of the standard high speed coupling shaft. Generator is located after the high speed coupling shaft and converts the mechanical power to electrical power. It consists of the rotor, stator, bearings and generator support bushings. The rotor of the generator used in the multi body simulations has 2000 kg mass and the stator has a mass of 5500 kg.

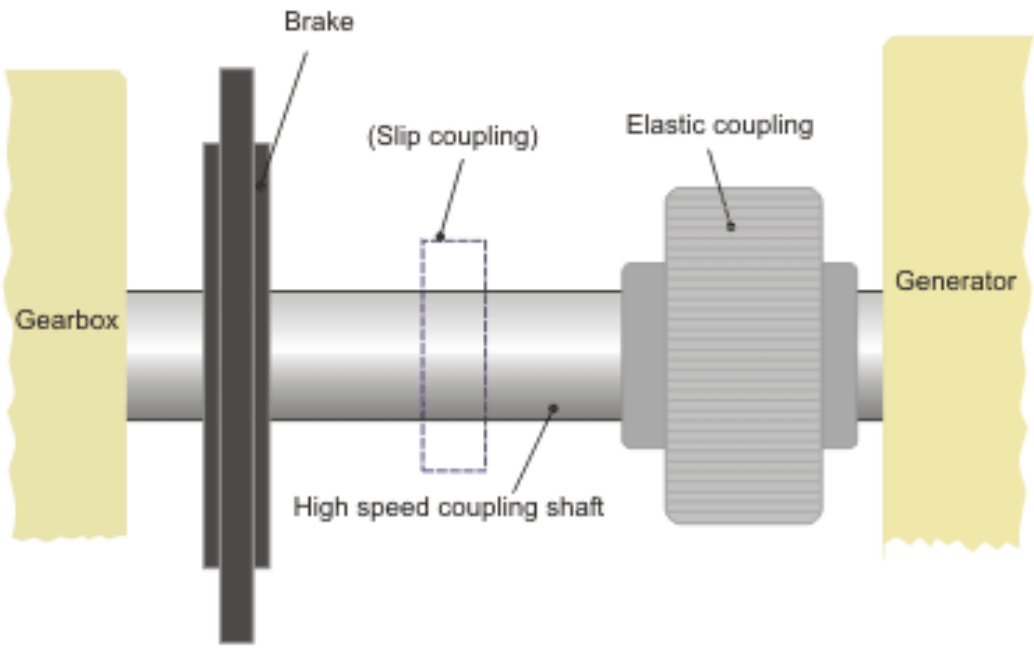

Figure 4.10: Standard high speed coupling shaft of the wind turbine system

All the parts of the drive train are located on the bed plate which is at the top of the tower. This bedplate is modelled as a set of beams. The bedplate supports the hub, the gearbox and the generator frame. In SWT, the Standard Beam bedplate is defined by two main parts: the bedplate and the yokes supporting the gearbox torque arms. The tower of the wind turbine system is selected simple tower in SWT. It is composed of single component tower itself. Figure 4.11 shows the main dimensions of the tower which are defined in the SWT. In the multibody simulations, the tower height is taken as 100 meters in the wind turbine model. The upper external and upper internal diameters are 3.87 and 3.49 meters, respectively. The lower external and lower internal diameters are 6 and 5.946 meters, respectively. The material of the tower is steel. Young modulus of the tower material is 210 GPa, Poisson's ratio is 0.3 and material damping is taken as 0.01 second. The density of steel is 7800 kg/m^3. Since, there are extra structures inside the tower (stairs, cables, connection parts etc.) the density of material is defined as 8500 kg/m^3.

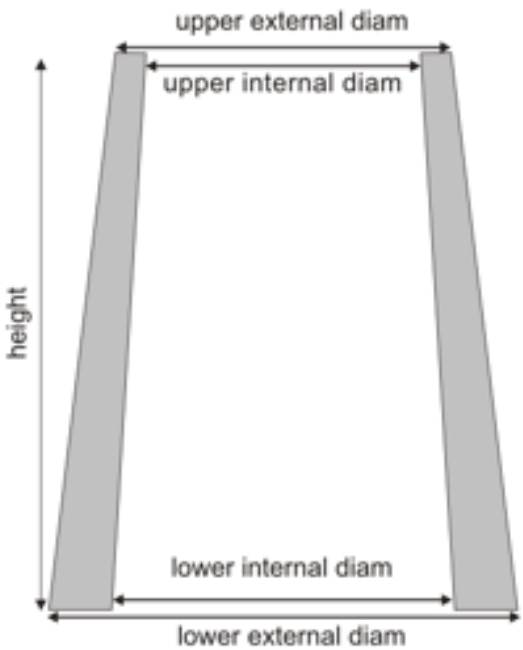

Figure 4.11: Standard tower model in SWT

4.1.4 Monitor Points on the Wind Turbine

Since the main objective of the thesis is to investigate the effect of off-axis ply placement in the spar caps of the wind turbine blade on the damage equivalent loads in the wind turbine system, damage equivalent loads are calculated at the critical monitor points which are selected in the wind turbine system. The load monitor points are selected as:

- Connection point between blades and the hub
- Connection point between the yaw drive and the bedplate (at the top of the tower)
- Connection point between the bedplate and the rotor shaft at the 1st and the 2nd main bearing locations (at the rotorshaft-side node)
- Connection point between the main shaft and the gearbox
- Rotor side and generator side planet carrier bearings of stages 1 and 2 in the gearbox

4.1.5 Load Cases

Multi-body simulation of the wind turbine system with superelement blade definition is performed in Samcef Wind Turbine for the power production load case using constant wind and the normal turbulence model as the external wind loadings, as specified in IEC 61400-1. Wind speed at the reference height is taken as 15 m/s with a wind shear exponent of 0.2, and in case of normal turbulence wind condition, Kaimal turbulence model is used for the generation of aerodynamic loading. In the turbulent wind analyses, IEC wind turbine class is taken as 1 and turbulence class is selected as B. Samcef Wind Turbine uses Turbsim [25] stochastic inflow turbulence tool developed by NREL to generate the turbulent wind data.

For the constant wind case, 120 second run is performed and for the turbulent wind condition, transient analysis is performed for 600 seconds as specified by

IEC-61400-1. In both cases, aerodynamic load is applied after 15 seconds of rotation of the turbine blades during which only the gravitational and centrifugal forces act on the blade. Fifteen seconds of rotation corresponds to three revolutions after which aerodynamic loading associated with constant wind and normal turbulence model is invoke. Figure 4.12 shows the load case type and the load case start and the end time defined in SWT.

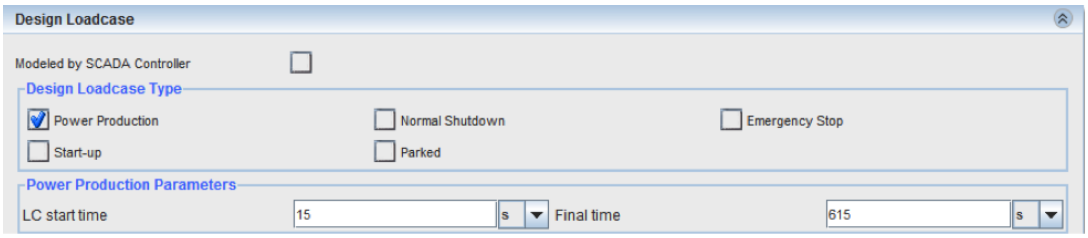

Figure 4.12: Power production load case selection in SWT

Constant wind data with wind shear is generated in SWT by defining wind velocity in x-y-z directions at the hub height, wind shear constant and the air density. Figure 4.13 shows the constant wind definition in SWT.

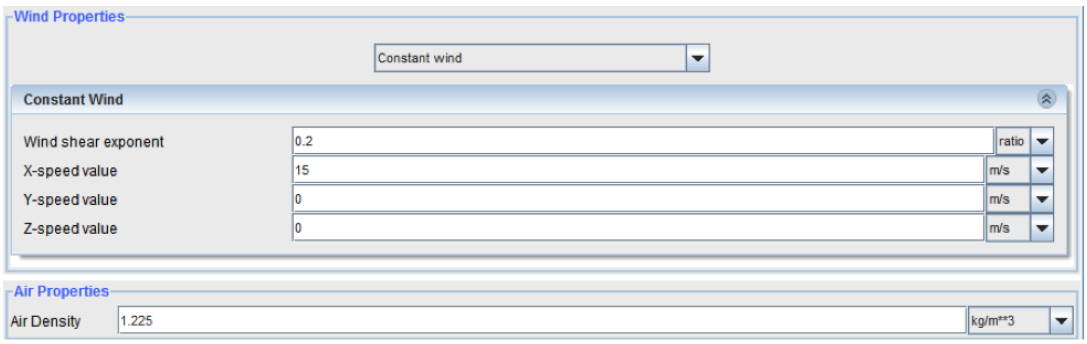

Figure 4.13: Constant wind load case generation in SWT

TurbSim is called by SWT to generate the turbulent wind data. To define turbulent wind case, one must define three types of data; TurbSim Meteorological Boundary Conditions, TurbSim Run Time Options and TurbSim Turbine/Model Specification. As seen in Figure 4.14, for wind turbine simulations under turbulent wind conditions, Kaimal turbulence model is selected, wind speed at the reference height is taken as 15 m/s, height of reference wind speed is 100 m (it is the height of the tower), wind shear exponent is 0.2, IEC turbulence type

is normal turbulence, IEC wind turbine class is 1 and IEC turbulence class is selected as B. There are four turbine class in IEC standards and class 1 is high wind class wind turbine. Two type of turbulence class is defined in IEC, "A" is higher turbulence class and "B" is lower turbulence class. Figure 4.15 shows the Run Time Options in which two random seeds are defined for Turbsim and clockwise rotation is selected when looking at the wind turbine in the downwind direction. Seeds are random number for Turbsim and different seeds give different turbulent wind data and same seed numbers give same turbulent wind data from Turbsim. In the Turbine/Model Specification menu, the grid definition, time definition and dimensions are defined as seen in Figure 4.16.

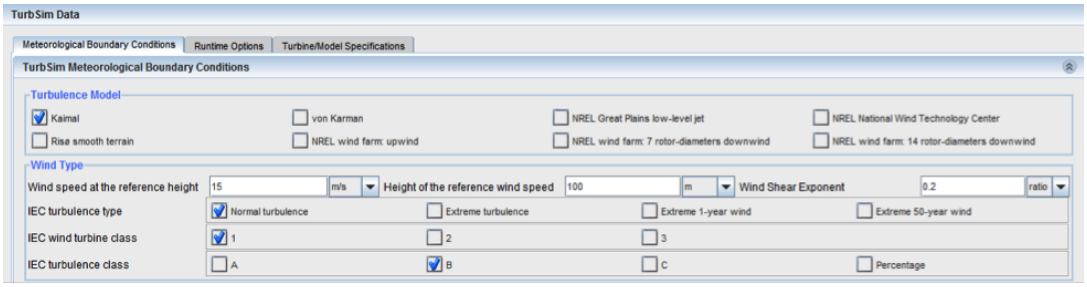

Figure 4.14: Turbulent wind type selection in Turbsim meteorological boundary conditions tab

Figure 4.15: Seed definition in the run time options tab

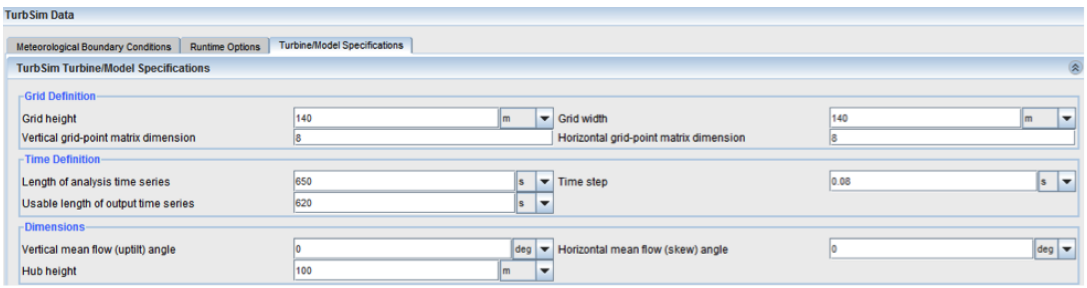

Figure 4.16: Grid definition of TurbSim turbine/model specification tab

4.1.6 Damage Equivalent Load

In the present study, for both constant wind and normal turbulence model wind condition, the analysis type is selected as fatigue analysis. To assess the material degradation associated with the cyclic loading, damage equivalent load is used as the metric instead of performing a complete fatigue analysis. Damage equivalent loads are calculated using Equation 4.2 which is derived based on the assumption that fatigue loads (F) are related with number of load cycles (N) such that the product $F^m N$ is constant, and in the Miner's rule, damage term is taken as 1 which indicates the occurrence of the fatigue failure. In Equation 4.2, N_{ref} is the reference number of cycles with typical reference number of cycles being 10^8 for wind turbine systems, m is the fatigue exponent with typical values in the range 3-10 depending on the material system, and F_i is the internal load corresponding to i^{th} bin with n_i being the number of fatigue load cycles corresponding to i^{th} bin. If damage equivalent loads are calculated using Equation 4.2 for two different load spectra, then the ratio of the damage equivalent loads, calculated for two different load spectra, become independent of the reference number of cycles N_{ref}.

$$F_{ref} = \left(\sum_{i=1}^{n} (F_i^m n_i)/N_{ref} \right)^{1/m} \tag{4.2}$$

CHAPTER 5

RESULTS

In the multi-body analysis of the wind turbine system, two load cases are considered; constant and turbulent wind load case. First, the results of the non-linear beam model of the zero degree blade (blade number 1 in Section 4) and superelement model of the zero degree blade (blade number 2 in Section 4) are compared for the constant wind load case. This study is performed in order to infer conclusions with regard to the appropriateness of the use of superelement blade definition in the transient analysis of the 5MW wind turbine system that is set up in the thesis. Damage equivalent loads for the wind turbine system having the superelement model of the all GFRPblade with zero degree spar cap plies (blade number 2 in Section 4) are taken as benchmark to compare with the damage equivalent loads obtained for wind turbine systems which havesuperelement blade models with off-axis spar cap plies. For the turbulent wind load case, damage equivalent loads at the monitor points of the wind turbine system with superelement blades are compared with the damage equivalent loads of the wind turbine system which has the baseline all GFRP superelement blade with zero degree spar cap plies.

5.1 Constant Wind Results

5.1.1 Comparative study of wind turbine simulation with superelement blades and geometrically nonlinear beam blades

Before the study of the effect of bending-twisting coupling on the loads acting on the wind turbine, a comparative study is conducted on the performance of the wind turbines which have blades defined as superelement and geometrically nonlinear beams in SWT. This study is performed in order to infer conclusions with regard to the appropriateness of the use of superelement blade definition in the transient analysis of the 5MW wind turbine system that is set up in the thesis. In wind turbine models, blades are defined as bladed-rotor in SWT with pressure/suction side and leading/trailing edge spar caps having unidirectional GFRP layers all aligned with the blade axis. In this respect, blade configuration used in the comparative study has the lowest coupling stiffness. One of the wind turbine models is established by introducing the superelement of the blade, which is inverse designed, as the bladed-rotor definition in SWT. In the second wind turbine model, bladed-rotor is defined as geometrically nonlinear beam. It should be noted that in SWT coupling stiffness are not included in the beam formulation. Therefore, blade defined as geometrically nonlinear beam only has major stiffness; flapwise, edgewise and torsional. On the other hand, superelement blade possesses the whole coupling effects with the only limitation that with respect to the local frame fixed to the blade, blade behaves geometrically linear. Multi-body simulation of the wind turbine is performed for constant wind speed that is taken as 15 m/s at the tower height with a wind shear factor of 0.2, and rated rotor speed is taken as 12 rpm. Multi-body simulations are performed for 240 seconds, and aerodynamic load is applied after 15 seconds of rotation of the turbine blades during which only the gravitational and centrifugal forces act on the blade. Fifteen seconds of rotation corresponds to three revolutions after which aerodynamic loading associated with the constant wind model is invoked. Figure 5.1 compares the peak axial displacements towards downwind at each section of blade calculated by the transient analysis of the wind turbine having superelement and geometrically nonlinear beam blade definitions. Peak

displacements at each blade section are compared in the 20m-61.5m range. As expected, nonlinear beam blade has higher lower displacement towards downwind due to the geometric stiffening of the blade. Peak tip displacement of the superelement blade is 65 cm higher than the nonlinear beam blade. Table 2 gives the average and damage equivalent loads calculated at the at blade-hub link node of the superelement and nonlinear beam blade, respectively. Average and damage equivalent loads are calculated for the duration 25s-240s of the transient analysis and for the damage equivalent load calculation fatigue exponent and reference number of cycles are taken as 4 and 108, respectively. Table 5.1 shows that average and damage equivalent loads calculated at the blade-hub link for the superelement and nonlinear beam blades are close to each other. The main differences are due to the nonlinear effects taken into account in the nonlinear beam blade, and coupling stiffness of the superelement blade which is mainly due to the blade geometry since the baseline blade has all spar plies aligned along the blade span. It should be noted that in the study of the effect of bending-twisting coupling on the load alleviation, percent difference of damage equivalent loads are used. Therefore, results of the preliminary analysis suggest that superelement blade can be used in the multi-body dynamic model of the wind turbine system for the study of the effect of bending-twisting coupling on the load alleviation in the wind turbine system.

Table 5.1: Comparison of average and damage equivalent loads at blade-hub link node

	Fx:Leadwise Force(N)	**Fz:Spanwise Force(N)**	**Mx:Leadwise Moment(Nm)**	**My:Flapwise Moment(Nm)**
SE blade				
Average Loads	151,293	579,688	1,241,145	4,945,262
DE Loads	1,505	8,835	175,525	52,653
Nonlinear blade				
Average loads	146,363	535,043	1,243,720	5,034,572
DE Loads	2,004	8,377	162,217	73,518

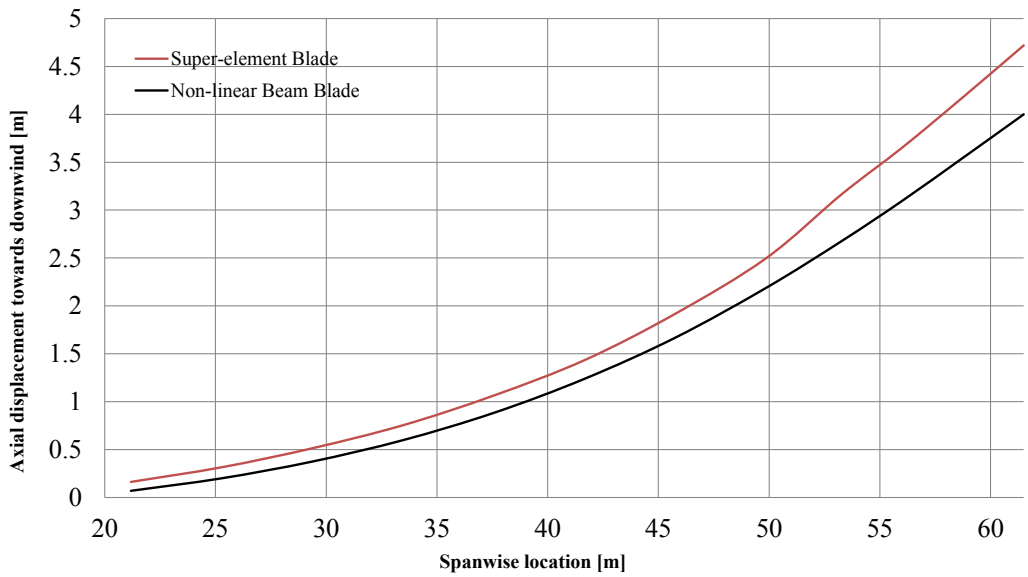

Figure 5.1: Comparison of peak axial displacements towards downwind

5.1.2 Effect of Off Spar Cap Plies On the Load Alleviation in the Wind Turbine System

After the comparison study of superelement blade and non-linear beam model blade, the effect of load alleviation is invastigated for the constant wind load case. For the constant wind load case, the transient analysis duration of the multibody model of the wind turbine models is taken as 120 seconds for each model. Figure 5.2 shows the effects of bending twisting coupling on the lift force of the blade sections. Figures 5.3 and 5.4 show the flapwise bending moment time history at the blade root for 120 seconds of transient aeroelastic simulation of the wind turbine system in SWT for the zero and fifteen degree spar cap ply orientation cases, respectively. In this section, loads at the blade root are calculated with respect to blade root reference system which rotates with the blade-hub link node. Blade root coordinate system is commonly known as rotor (flapwise, leadwise) coordinate system which is also preferred for test purposes.

From the time plots shown in Figures 5.3 and 5.4, it is seen that there is a slight reduction in the range of the flapwise bending moment for the blade with fifteen degree spar caps plies. To compare the fatigue damage that these load spectrums

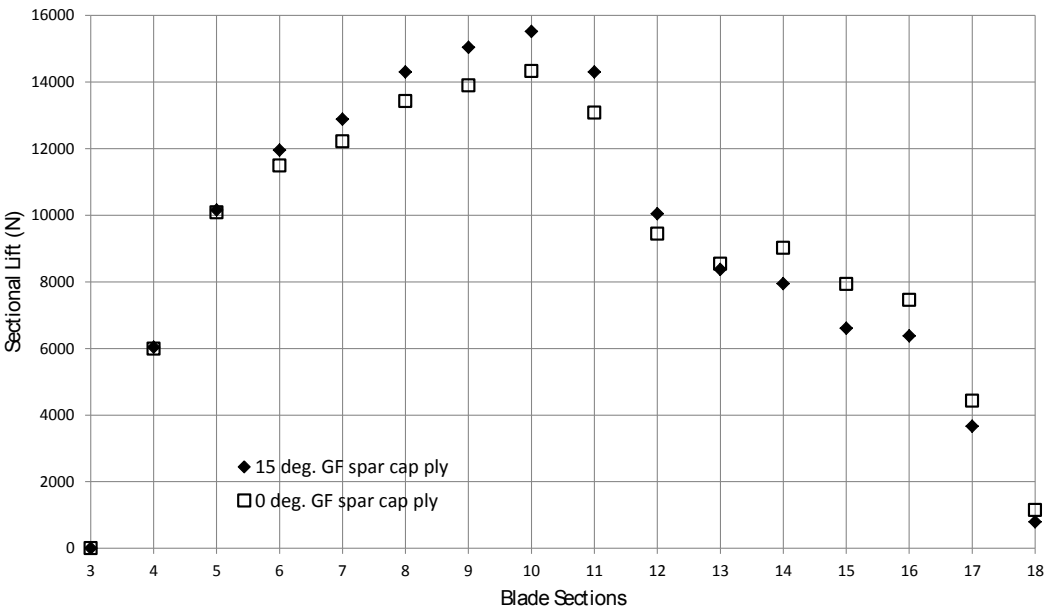

Figure 5.2: Comparison of sectional lift forces of zero and fifteen degree GFRP spar cap configurations

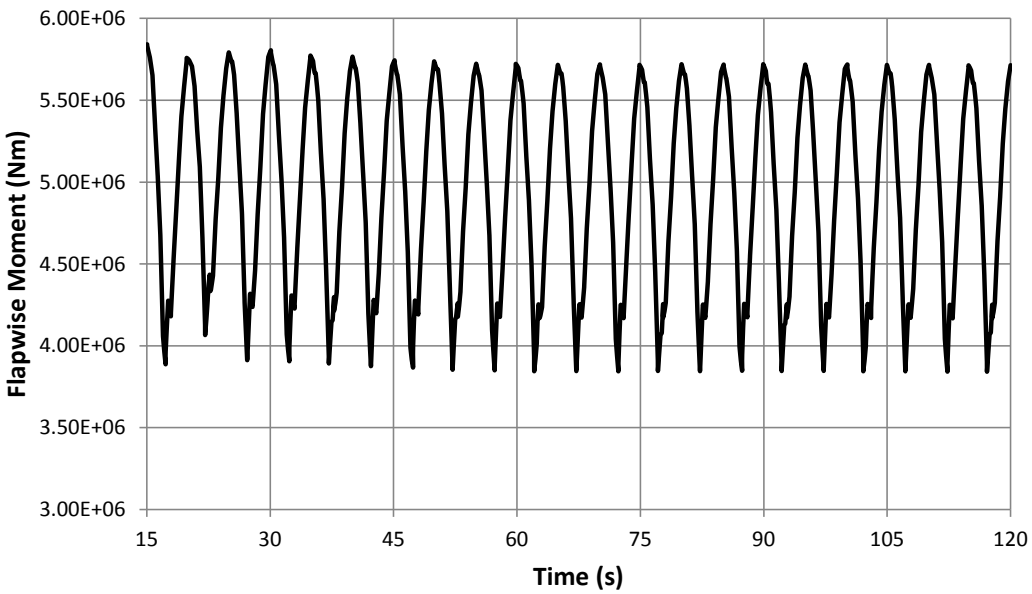

Figure 5.3: Flapwise root moment of blade 1 of zero degree GFRP spar cap configuration

cause, damage equivalent flapwise root bending moments are calculated utilizing two different fatigue exponents m in Eq. 4.2. A low value of fatigue exponent such as 4 is used for metal structures whereas an m value of 10 is a typical

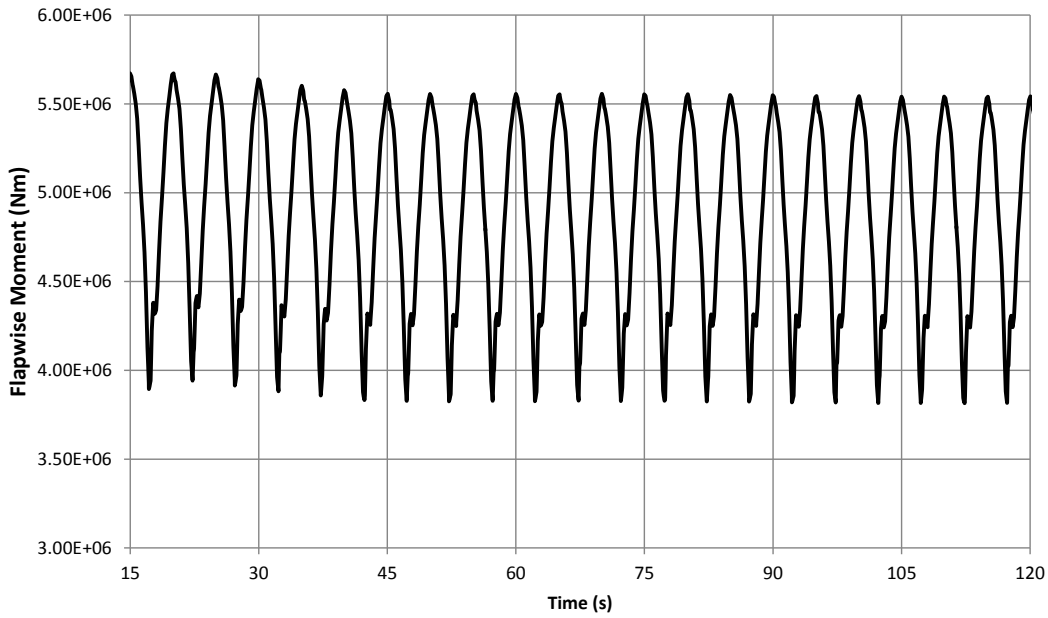

Figure 5.4: Flapwise root moment of blade 1 of fifteen degree GFRP spar cap configuration

value that is used for fiberglass composites [15]. However, in terms of ratio of the damage equivalent root flapwise bending moment, the use of any exponent gives the same result. Table 5.2 summarizes the damage equivalent moments calculated at the root of the blade for two different fatigue exponents 4 and 10. Damage equivalent moments are calculated for the time period 15-120 seconds after the constant wind load case is invoked, and they correspond to the range value. It is seen that although there is %5 increase in the torsional moment for the fifteen degree spar cap ply case, there is %8 reduction in the flapwise bending moment in favor of the fifteen degree spar cap ply case. More importantly, absolute value of the damage equivalent torsional moment is very low compared to the flapwise and leadwise moment. Therefore, it can be concluded that the blade root for the 15 degree spar cap ply case is more durable compared to the zero degree spar cap case. It should be noted that the blade root moments calculated can be considered as moments acting on the composite blade and also on the blade-hub connection points which are metallic. Thus, damage equivalent moments calculated for the fatigue exponent of 4 are associated with the metallic blade-hub connection points, whereas damage equivalent moments calculated for

the fatigue exponent of 10 are associated with the fiberglass composite blade.

Table 5.2: Damage equivalent load results of zero degree and fifteen degree GFRP configurations with different m values

DE Root Moments (Nm)	m=4 15 degree spar cap	m=4 0 degree spar cap	m=10 15 degree spar cap	m=10 0 degree spar cap	Ratio of DE root moments
Leadwise moment	126,464	127,571	1,380,670	1,392,760	0.99
Flapwise moment	35,117	38,156	383, 387	416,571	0.92
Torsional moment	1,949	1,844	21,275	20,137	1.05

Figures 5.5 and 5.6 compare the generated power of the wind turbines having superelement blades with zero and fifteen degree spar cap plies.In both cases,the generated power approaches to 5MW and there is almost no difference in the generated powers for the wind turbines with zero and fifteen degree spar cap plies.

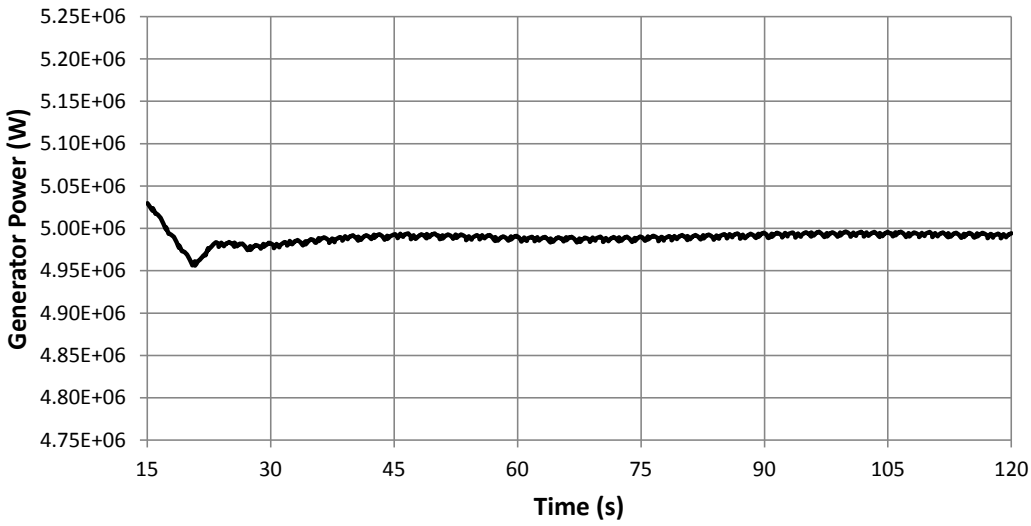

Figure 5.5: Generator power output of zero degree GFRP spar cap configuration

Figures 5.7 and 5.8 give the downwind tip displacement of the blades having 0 degree and 15 degree spar cap ply orientations, respectively. No major difference is observed in the tip displacements for the two blade configurations. It is seen that peak displacement converges to a value of about 4.62-4.63 meter in both cases. On the other hand, the converged value ofthe lowest displacement is

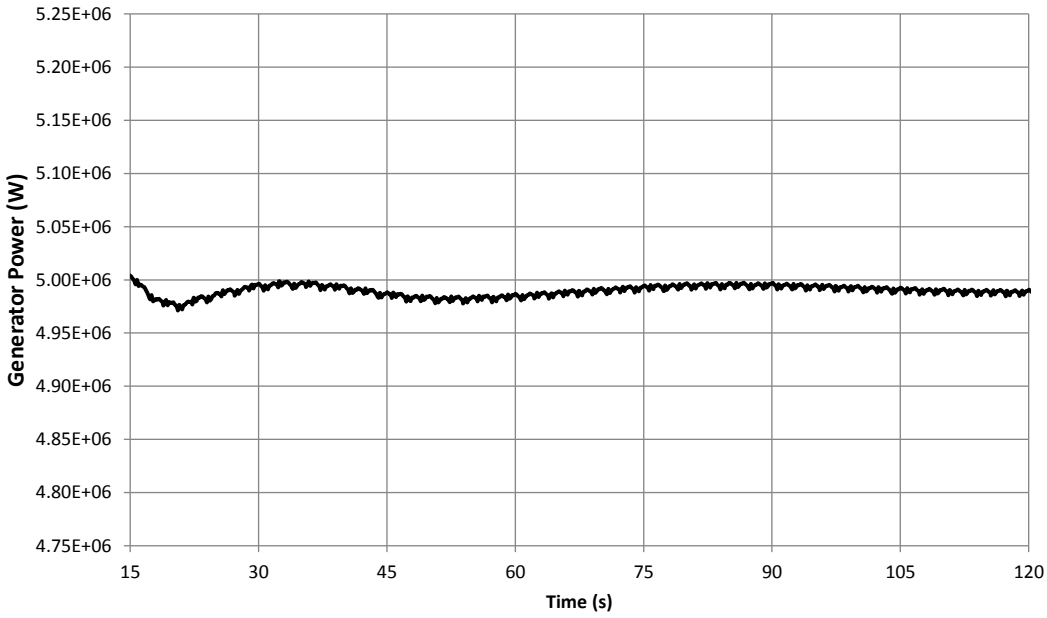

Figure 5.6: Generator power output of fifteen degree GFRP spar cap configuration

2.84m for the 0 degree spar cap ply case and for the 15 degree spar cap ply case, lowest displacement is about 3 m. It should be noted that the main reason for the large oscillation in the tip displacements is due to the wind shear effect.

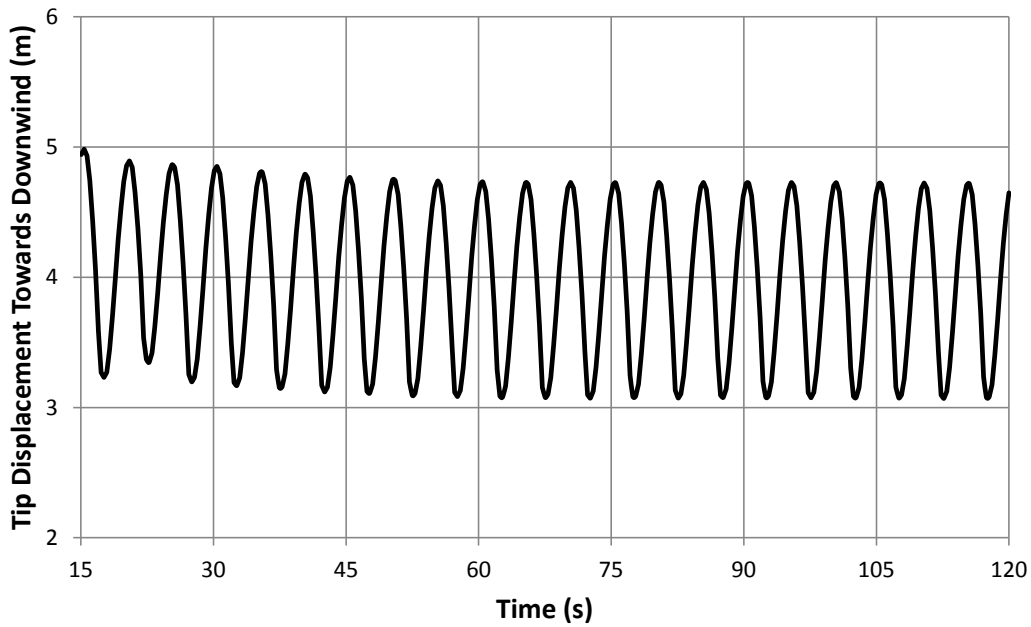

Figure 5.7: Blade tip displacement of zero degree GFRP spar cap configuration

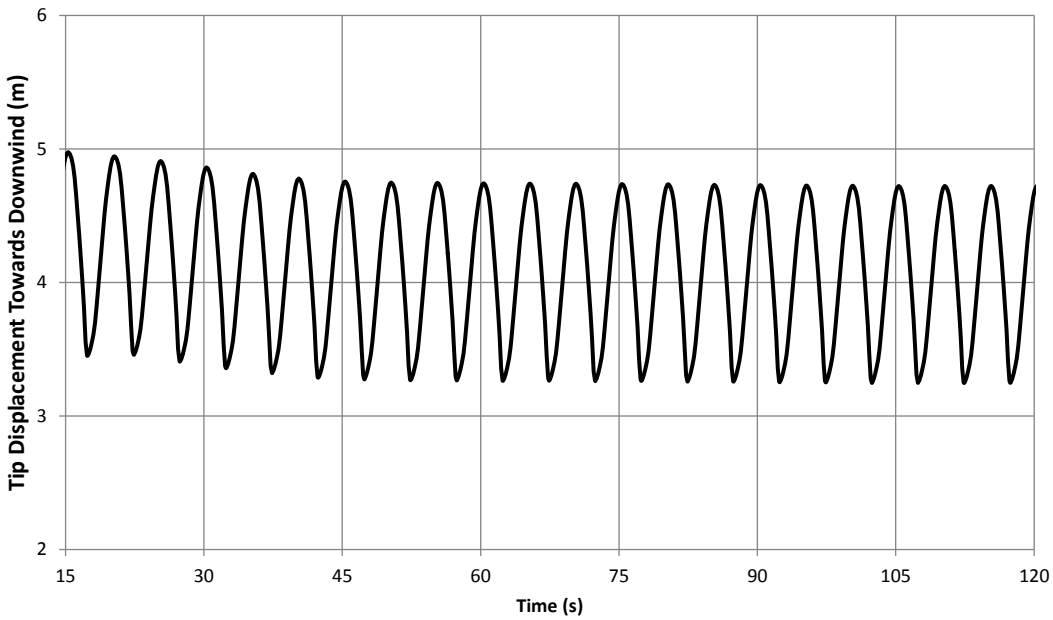

Figure 5.8: Blade tip displacement of fifteen degree GFRP spar cap configuration

In order to evaluate the effect of off-axis spar cap plies on the load alleviation in the wind turbine system better, turbulent wind loading is a more realistic load case because in real operating conditions there is seldom constant wind condition. Therefore, in the remaining part of the thesis emphasis is given to turbulent wind load case.

5.2 Turbulent Wind Results

For the turbulent wind load case, the duration of the transient analysis is taken as 615 seconds, but damage equivalent loads are calculated for a duration of 600 seconds in accordance with IEC-61400-1. Since in all analyses, wind turbine is let to rotate freely for three revolutions before applying the load case, calculation of the damage equivalent loads is started after 15 seconds which corresponds to the rotation of the wind turbine for three revolutions, and the calculation of the damage equivalent loads is stopped at the 615th second.

5.2.1 Results for Wind Turbine System with 15 Degree Off-Axis GFRP Spar Cap Plies

Figures 5.9 and 5.10 show the flapwise bending moment time history at the blade root for 615 seconds of transient aeroelastic simulation of the wind turbine system for the zero and fifteen degree spar cap ply orientation cases, respectively.

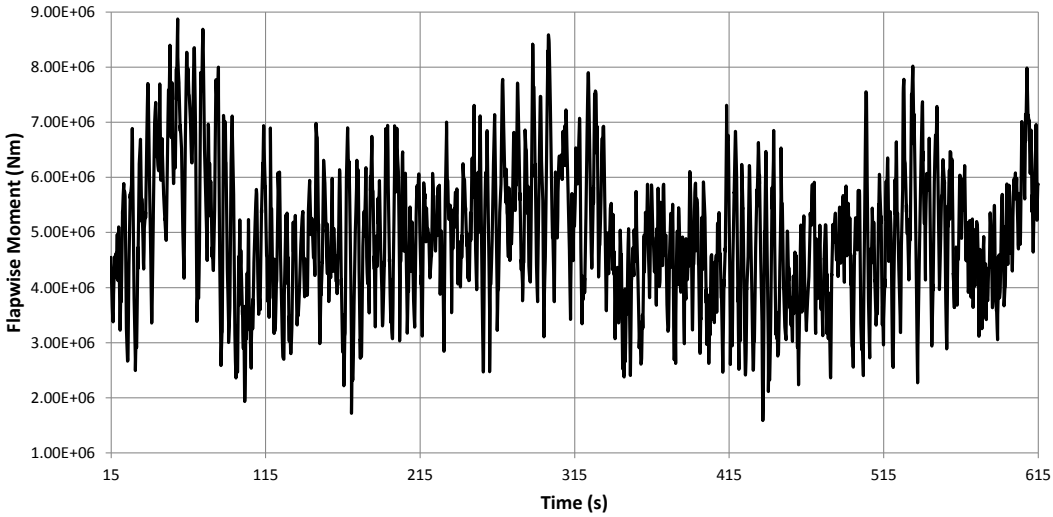

Figure 5.9: Flapwise root moment of blade 1 of zero degree GFRP spar cap configuration

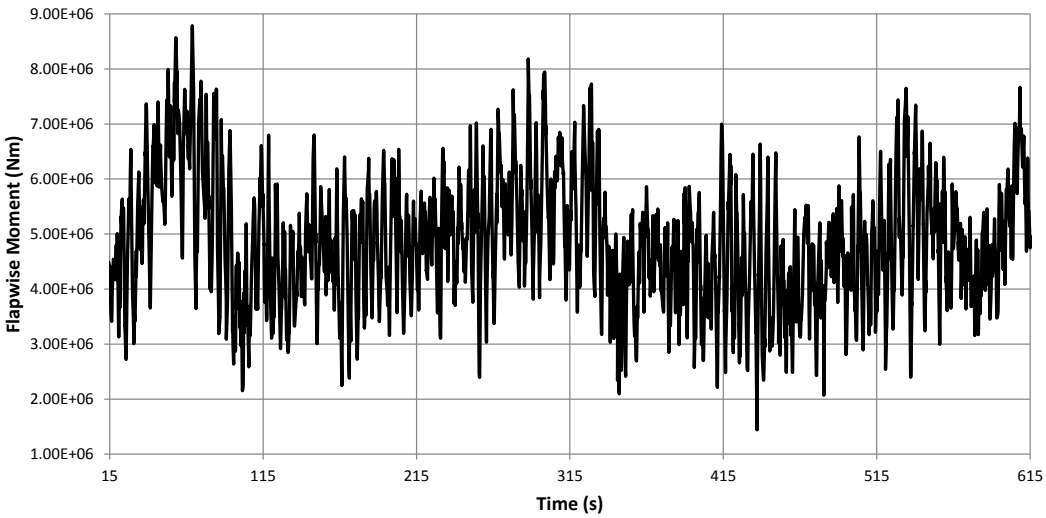

Figure 5.10: Flapwise root moment of blade 1 of fifteen degree GFRP spar cap configuration

From the time plots shown in Figures 5.9 and 5.10, a slight reduction in the range of the flapwise bending moment for the blade having fifteen degree spar cap plies is evident.To compare the fatigue damage that these load spectrums cause, damage equivalent flapwise root bending moments are calculated utilizing a fatigue exponent of 4 in Eq. (DEL). Table 5.3 summarizes the damage equivalent moments calculated at the root of the blade. From Table 5.3, it is seen that for the fifteen degree spar cap ply case, there is %9 reduction in the damage equivalent flapwise bending moment compared to the zero degree spar cap ply case. On the other hand, for the 15 degree spar cap ply case, damage equivalent leadwise and torsional moments are almost same as the 0 degree spar cap ply case. However, if one looks at the overall picture, it can be concluded that for the turbulent load case, there is significant reduction in the damage equivalent moment at the blade root. It should be noted that with the off-axis spar cap ply modification in the blades, it has not been possible to get reduction in the leadwise moment at the blade root.

Table 5.3: Damage equivalent blade root moments calculated for the turbulent wind load case

DE Root Moments (Nm)	m=4 0 degree spar cap	m=4 15 degree spar cap	Ratio of DE root moments
Leadwise moment	205,509	207,498	1.01
Flapwise moment	123,526	112,821	0.91
Torsional moment	3,993	4,054	1.02

Figure 5.11 and Figure 5.12 show the tip displacements towards downwind direction of zero degree GFRP blade and fifteen degree GFRP blade, respectively. For tip displacement of blades, the maximum value is critical since there is a risk for tower collision of blades in wind turbine systems. The maximum tip displacement of the fifteen degree GFRP blade is 7.93 meters and zero degree GFRP blade has 7.64 meters maximum tip displacement for turbulent load case. The difference between the tip displacement of two blade configurations is acceptable and one should remember that the flapwise stiffness of fifteen degree GFRP blade is about %25 lower than zero degree GFRP blade. As seen from

the figures the fluctuation range of the fifteen degree GFRP blade is smaller that is mostly related to DE loads in flapwise direction of the blade.

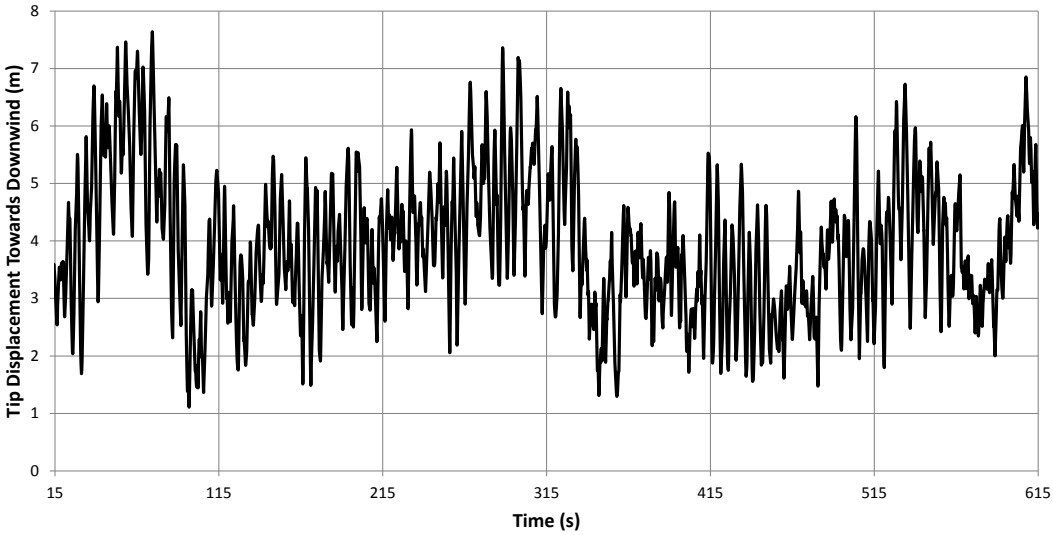

Figure 5.11: Tip displacement of zero degree GFRP spar cap configuration

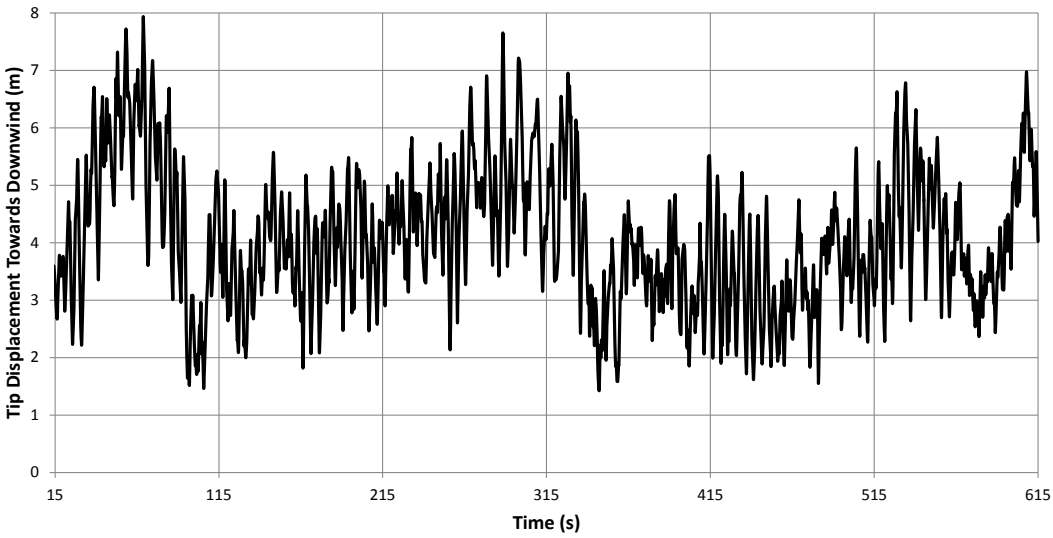

Figure 5.12: Tip displacement of fifteen degree GRPF spar cap configuration

Figures 5.13 and 5.14 show the generated power of the wind turbines having superelement blades with zero and fifteen degree spar cap plies for the turbulent wind load case. It is noted that the generated power in both cases fluctuates around 5MW and there is almost no difference in the generated powers for the

wind turbines with zero and fifteen degree spar cap plies.

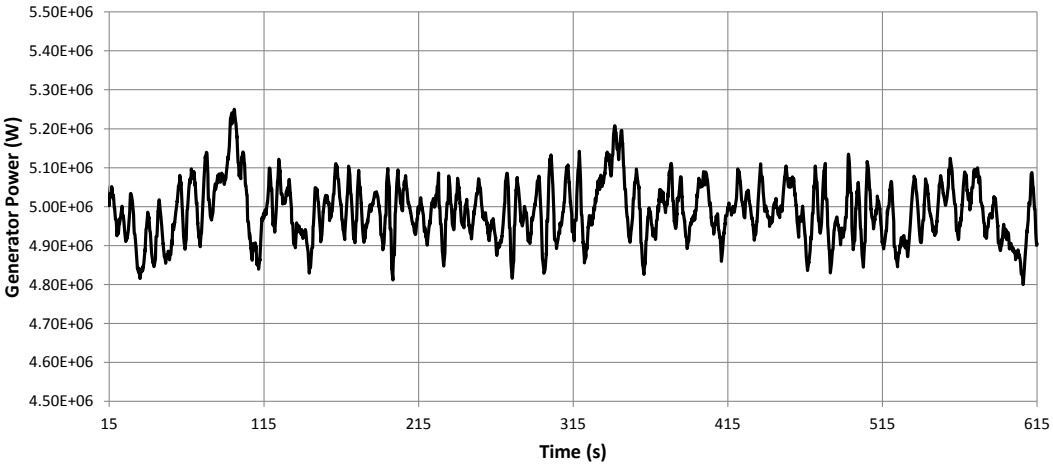

Figure 5.13: Generator power output of zero degree GFRP spar cap configuration

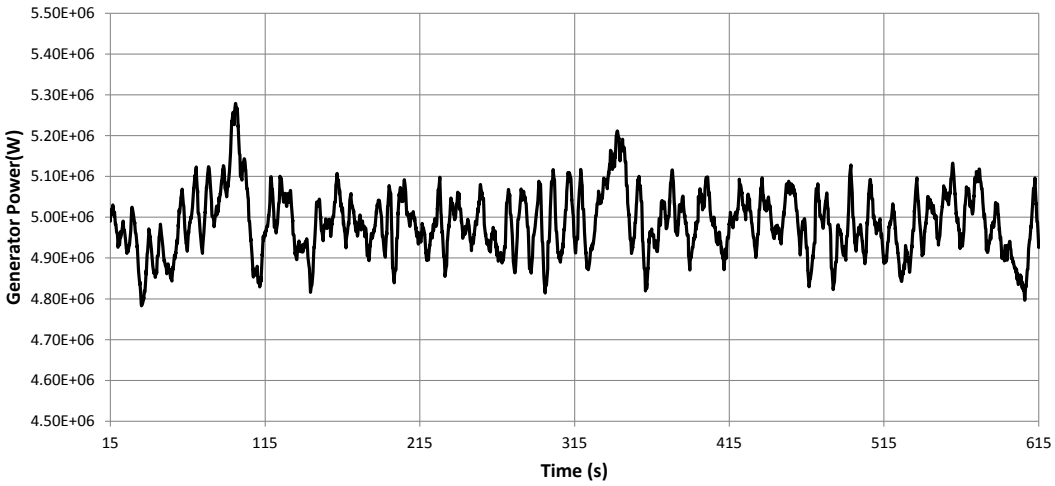

Figure 5.14: Generator power output of fifteen degree GFRP spar cap configuration

Figure 5.15 shows the x , y and z forces acting on the bedplate-tower link for the wind turbine with blades having 0 degree spar cap plies. Forces are calculated with respect to the fixed global model coordinate frame of the wind turbine shown in Figure 4.1. For the wind turbine with blades having 15 degree spar cap ply orientation, x -y-z forces acting on the bedplate-tower connection look very similar to the zero degree case. Figure 5.15 that z-force has the highest mean value which includes the weight of the tower-top systems. However, the

range of the oscillation of the z force is very low similar to the range of the y force which is the lateral force acting on the tower. On the other hand, x force has much higher range value than the y force and the z force. Therefore, it can be concluded that in terms of fatigue damage, x-force, which is the thrust force acting on the wind turbine, is much more critical compared to the y-force or the z-force. To compare the fatigue damage that bedplate-tower link force spectrums cause,damage equivalent forces are calculated with the fatigue exponent 4. Table 5.4 summarizes the damage equivalent bedplate-tower link forces calculated for the turbulent wind load case. In Table 5.4, it can be seen that damage equivalent x-force of tower top forces reduces by %10 in turbine with blades having 15 degree spar cap plies. It is noted that compared to the zero degree spar ply case, damage equivalent y force decreases by %1 and damage equivalent z- force increases by %1 for the 15 degree spar cap ply case. However, fatigue damage due to x-force is much more critical than the fatigue damage due to the y-force or the z-force since the range value of the damage equivalent x-force is much higher than the range values of the damage equivalent y-force and z- force.

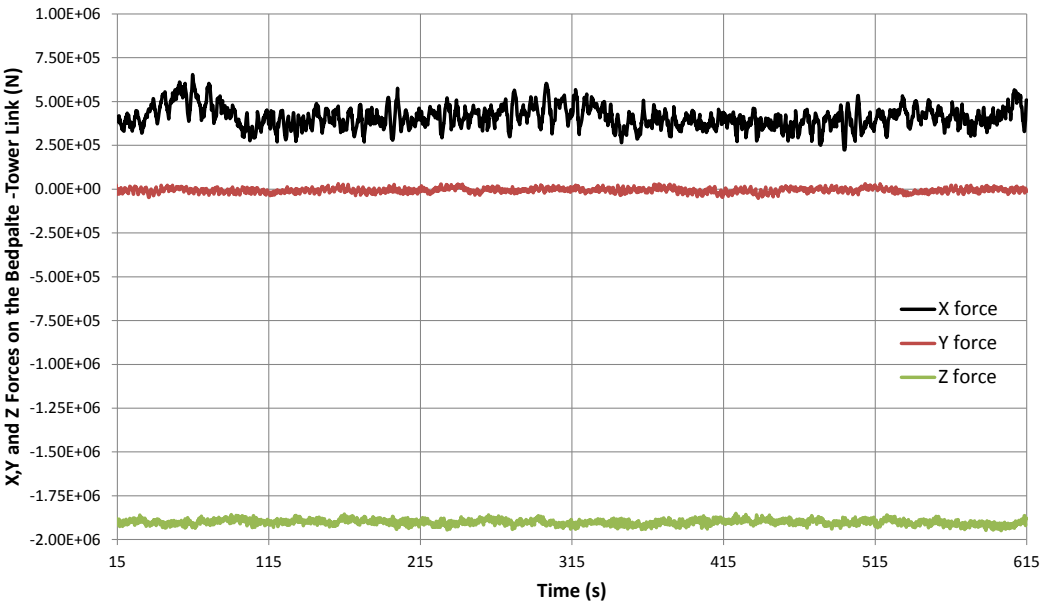

Figure 5.15: X , Y and Z forces acting on the bedplate-tower link for the wind turbine with blades having zero degree spar cap plies

Figure 5.16 shows the x, y and z moments acting on the bedplate-tower link for

Table 5.4: Damage equivalent bedplate-tower link forces calculated for the turbulent wind load case

DE Tower Top Forces (N)	m=4 0 degree spar cap	m=4 15 degree spar cap	Ratio of DE root loads
X Force	5,901	5,247	0.89
Y Force	1,511	1,536	1.02
Z Force	1,856	1,896	1.02

the wind turbine with blades having 0 degree spar cap plies.This time, moments are calculated with respect to the fixed tower foundation coordinate system shown in Figure 4.2. As Figure 5.16 shows, the mean and the range of the y-moment is considerably higher than the mean and the range of the x-moment and the z-moment acting on the bedplate-tower connection link. Table 5.5 the damage equivalent bedplate-tower link moments calculated for the turbulent wind load case. From Table 5.5, it can be seen that in the turbine having blades with 15 degree spar cap plies, damage equivalent x, y and z moments reduce by %5 , %4 and %6 respectively. Examination of Figure 5.16 and Table 5.5 shows that for oscillating loads, if the mean and range values of the load are high then the corresponding damage equivalent load is also high. It is noted that although the z-moment has a lower mean compared to the mean of x-moment, since the range of z-moment is much higher than the range of the x-moment, damage equivalent z-moment is considerably higher than the damage equivalent x-moment.

Table 5.5: Damage equivalent load results of zero degree and fifteen degree GFRP configurations with different m values

DE Tower Top Moments (Nm)	m=4 0 degree spar cap	m=4 15 degree spar cap	Ratio of DE root loads
X Moment	11,921	11,616	0.97
Y Moment	98,659	96,005	0.97
Z Moment	107,908	101,156	0.94

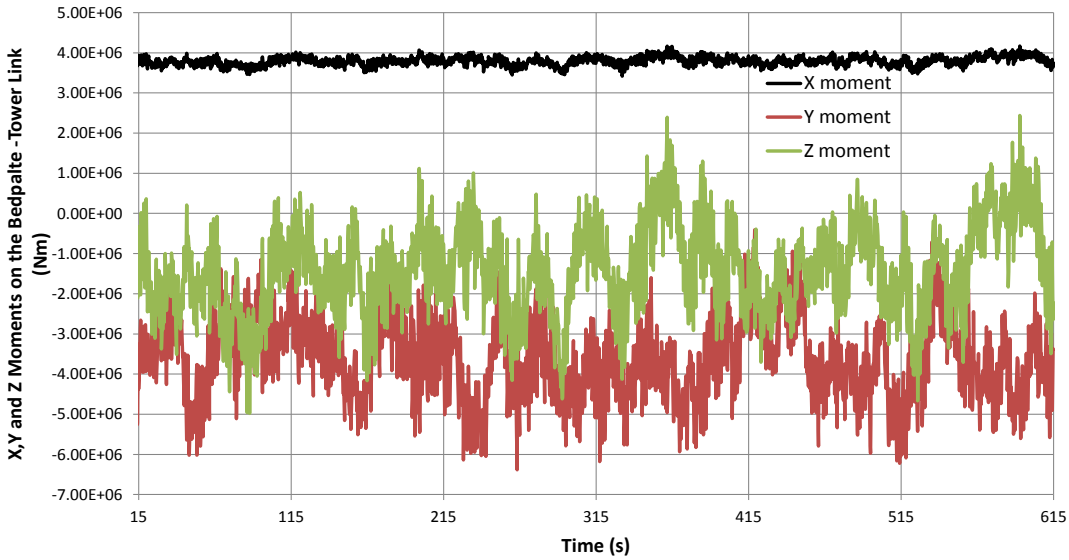

Figure 5.16: X, Y and Z moments acting on the bedplate-tower link for the wind turbine with blades having 0 degree spar cap plies

For the turbulent wind condition, no major difference is observed in the tip displacements for the two blade configurations. After the load case is invoked at 15th second, maximum instantaneous tip displacement for both 0 degree and 15 degree cases is about 7.6m. For the zero degree case, average tip displacement during 15-615 seconds is 3.82 m and for the 15 degree case, average tip displacement is 3.92 m. Slight increase of the average tip displacement is due to the reduction of the bending stiffness of the blades in the outboard section due to the use off axis plies in the main spar caps. For both 15 degree and 0 degree cases, tower surface closest approach is calculated to be about 5 meters.

Figure 5.17 shows the mainshaft-bedplate connection at the main bearing locations 1 and 2. In the drive train model that is set up in SWT, main bearing 1 is the bearing which is closer to the rotor and it takes all the axial force in the direction the main shaft, and main bearing 2 only takes the lateral forces. Forces in the main bearing-bedplate connections points, shown by green dots in Figure 5.17, are calculated with respect to the hub-fixed coordinate system which is parallel to the fixed global model coordinate frame shown in Figure 4.1. The origin of the hub-fixed coordinate system is located at the main shaft-bedplate connection point at the main bearing 1 location, and it does not rotate with the rotor. Table 5.6 gives the damage equivalent main shaft-bedplate connection

forces calculated for the turbulent wind load case. In Table 5.6, X, Y and Z damage equivalent forces calculated are parallel to the global model coordinate frame shown in Figure 4.1 From Table 5.6, it can be seen that $\%4 - \%10$ reductions in damage equivalent forces in main bearings 1 and 2 can be achieved with the use of blades having 15 degree off-axis spar cap plies. Reduction in main bearing forces is very important in terms of decreasing the bearing failures associated with the fatigue loading in the long operation times of the wind turbine system.

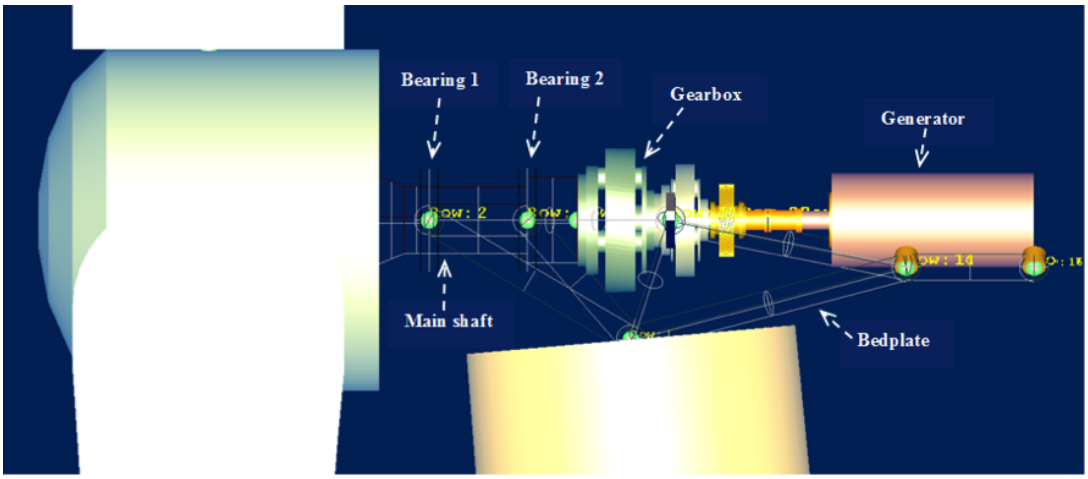

Figure 5.17: Main shaft-bedplate connections: Main bearings 1 and 2

Table 5.6: Damage equivalent main shaft-bedplate connection forces at main bearing loacations 1 and 2

Bearing Locations	Damage Equivalent Forces (N)	m=4 0 degree spar cap	m=4 15 degree spar cap	Ratio of DE root loads
Main Bearing 1	X Moment	5710	5088	0.89
	Y Moment	82819	77532	0.94
	Z Moment	74800	72577	0.97
Main Bearing 2	Y Moment	73732	68910	0.93
	Z Moment	65892	63771	0.97

Figure 5.18 shows the main shaft-gearbox connection point where the forces are calculated with respect to non-rotating global model coordinate frame shown in

Figure 4.1. At this connection, X force is of negligible value since the axial force of the rotor system is taken by the main shaft first bearing. Therefore, damage equivalent load for the X force is not calculated. Table 11 gives the damage equivalent main shaft-gearbox connection forces and moments calculated for the turbulent wind load case. From Table 5.7, it can be seen that with the 15 degree spar cap case, damage equivalent Y and Z forces, which are essentially shear forces acting on the shaft near the gearbox connection point, drop compared to the 0 degree case. Similar reduction is also observed in the damage equivalent Y and Z bending moments. However, damage equivalent X moment increases by %5 for the 15 degree spar cap case. X moment at the hub-blade connection point is essentially same as the X moment at the main shaft-gearbox connection point through which the useful aerodynamic torque flows into the gearbox.

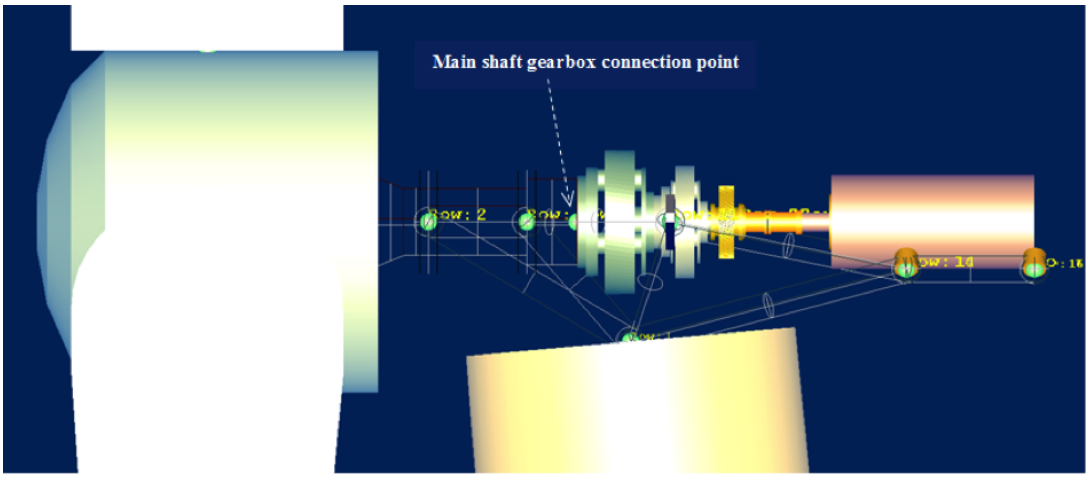

Figure 5.18: Main shaft-gearbox connection point shown in the wind turbine system

Table 5.8 compares the maximum and minimum peak values and average value of the X moments of the blades with 15 degree and 0 degree spar cap plies. Figures 5.19 and 5.20 compare the X moments at the center of the rotor hub for the 0 degree and 15 degree spar cap ply cases, respectively. From Table 5.8 and from the time plots given in Figures 5.19 and 5.20, it is seen that the peak X moment value of the 0 degree case is actually higher than the peak X moment value of the 15 degree case. However, careful comparison of Figures 5.19 and 5.20 reveals that for the 15 degree case, peak values of the X moment is higher. Therefore, damage equivalent X moment of the blade with 15 degree spar cap

Table 5.7: Damage equivalent forces and moments at the main shaft-gearbox connection point

Main Shaft Gearbox Connection	Damage Equivalent Loads	m=4 0 degree spar cap	m=4 15 degree spar cap	Ratio of DE root loads
Forces (N)	Y Force	8920	8446	0.95
	Z Force	8802	8627	0.98
Moments (Nm)	X Moment	5722	6159	1.08
	Y Moment	7233	7121	0.98
	Z Moment	7107	6706	0.94

plies is higher compared to the damage equivalent X moment of the blade with 0 degree spar cap plies. Although the actual reason for the increase of the peak values of the X moment is not well understood, it is considered that it is related to bending-twisting coupling that is induced due to the off-axis spar cap plies.

Table 5.8: Maximum, minimum peak and average values of X moment

	15 degree spar cap	0 degree spar cap
Maximum X Moment (N.m)	4.11E+06	4.12E+06
Minimum X Moment (N.m)	3.86E+06	3.86E+06
Average X Moment (N.m)	3.97E+06	3.97E+06

In this study, damage equivalent shear forces are also calculated at the planet carrier bearings of the two stage planetary and one stage parallel gearbox of the wind turbine system shown in Figure 5.21. As shown in Figure 4.9, planet carrier bearings are the main bearings which support the two stages of planetary gears on the main shaft. Table 5.9 summarizes the damage equivalent shear forces Y and Z, which are calculated in the global model coordinate frame of the wind turbine shown in Figure 4.1, at the rotor and generator side planet carrier bearings of stages 1 and 2. It is seen that for the wind turbine having blades with 15 degree spar cap plies, damage equivalent forces reduce both at the rotor and generator side planet carrier bearings. However, because of the

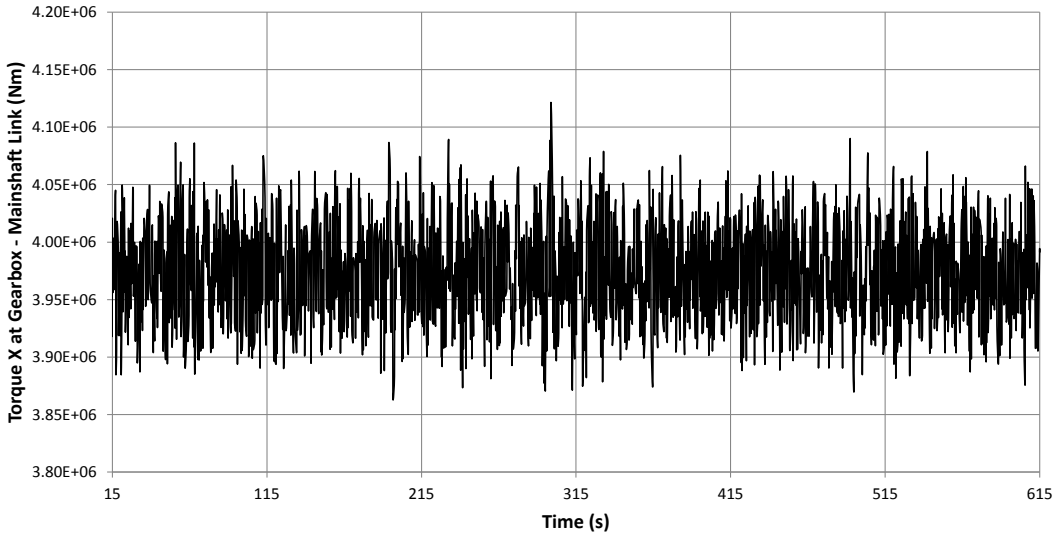

Figure 5.19: X moment acting on the center of the rotor hub wind turbine; blades with 0 degree spar cap plies

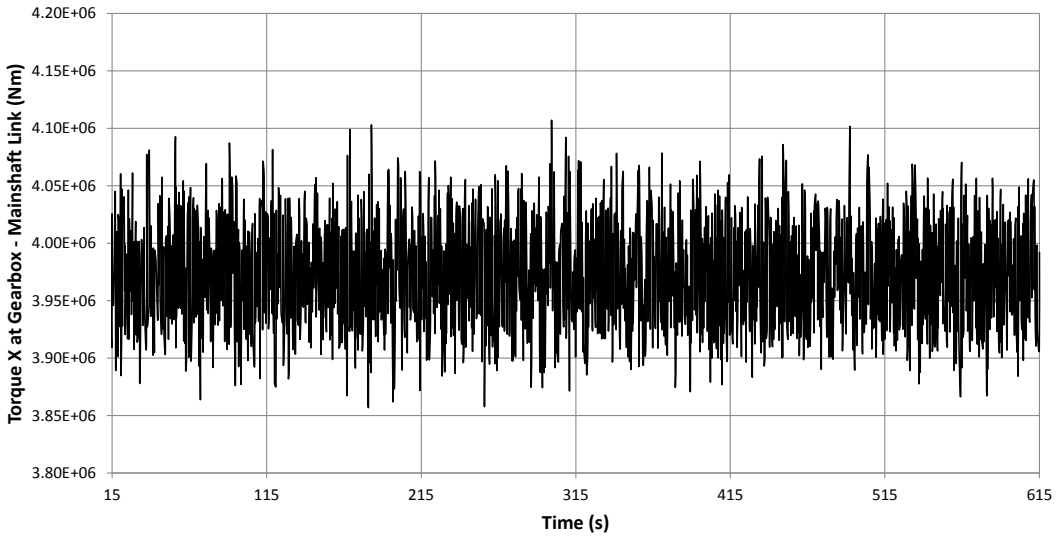

Figure 5.20: X moment acting on the center of the rotor hub wind turbine; blades with 15 degree GFRP spar cap plies

increase of the damage equivalent torque (X moment) at the main shaft-gearbox connection point, damage equivalent gear contact forces increase in the gears. If, with design changes in the spar caps of the blades, damage equivalent main shaft torque can be reduced or at least kept constant, then present study shows that with the introduction of off-axis spar cap plies, it is possible to reduce damage equivalent loads in all of the critical components of the wind turbine system.

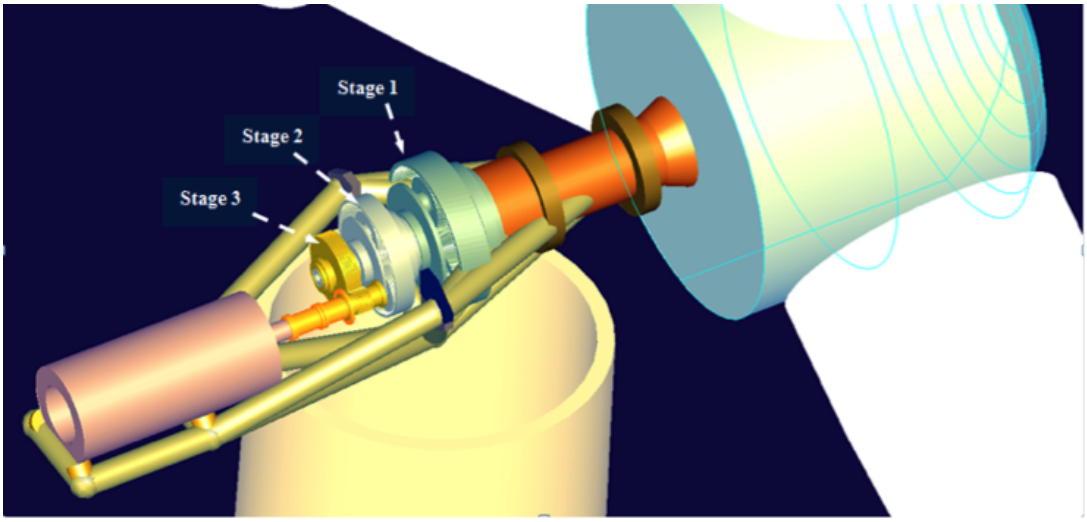

Figure 5.21: Two stage planetary, one stage parallel gear box

Table 5.9: Damage equivalent shear forces at the planet carrier bearings of stages 1 and 2

Stages	Bearing Locations	DE shear Forces	m=4 0 degree spar cap	15 degree spar cap	Ratio of DE shear forces
Stage 1	Rotor Side	Y Force	309	265	0.86
		Z Force	594	595	1.00
	Generator Side	Y Force	7519	7039	0.94
		Z Force	7897	7842	0.99
Stage 2	Rotor Side	Y Force	1923	1897	0.99
		Z Force	1647	1492	0.91
	Generator Side	Y Force	911	825	0.91
		Z Force	826	891	1.08

5.2.2 Results for Wind Turbine System with 15 Degree Off-Axis CFRP Spar cap Plies

For the turbulent wind condition, Table 5.10 compares the damage equivalent loads calculated at the monitor points in the wind turbine system having blades with 15 degree GFRP and CFRP spar cap plies. Table 5.11 compares the ratio of DE loads calculated at the monitor points in the wind turbine system

having blades with 15 degree GFRP and CFRP spar cap plies. Comparisons are made at the monitor points for which results are already presented for the GFRP case in Tables 5.4-5.6 and Table 5.9. From Table 5.11, it can be seen that with the introduction of off-axis CFRP spar cap plies in the blades, higher reductions in the damage equivalent loads can be achieved in the selected monitor points in the wind turbine system. Especially, damage equivalent blade root moments and damage equivalent forces acting at the tower-bedplate connection point are significantly lower compared to the GFRP case. Results show that the bending-twisting coupling effectiveness of the CFRP blade is higher than the GFRP blade. However, at the main shaft-gear box connection, compared to the GFRP case, damage equivalent X moment is seen to increase further for the CFRP case. The detail analyses of the DE X moment at the gear-box main shaft link node is given in Section 5.2.4. The gear box is a very dynamic part of the wind turbine system and from the industrial point of view the DE loads are not critical for this kind of dynamic part. The important criteria for dynamic parts are time at level counting analyses of the transient load results and it is suggested as future work. In time at level counting analyses, the life time of a discretized load levels are calculated. If the dynamic component is exposed higher loads for longer durations then the life of it diminished.

Figure 5.22 shows the tip displacement of the CFRP blade. There is a small improvement at maximum tip displacement of the blades although the flapwise stiffness of the blades are lower than zero degree GFRP blades. The maximum tip displacement of the CFRP blade is 7.41 meter and minimum tip displacement of the blade is 1.23 meters. Similar to the fifteen degree GFRP blade's tip displacement results the fluctuations of the blade tip is lower than the fluctuations of the blade tip of the zero GFRP blade.

Table 5.10: Damage equivalent load results of zero degree, fifteen degree GFRP and fifteen degree CFRP configurations

Monitor Point	**GFRP** 0 degree spar cap	**GFRP** 15 degree spar cap	**CFRP** 15 degree spar cap
Blade root			
Leadwise moment	205509	207498	175578
Flapwise moment	123526	112821	111170
Torsional moment	3993	4054	3588
Bedplate-tower link			
X force	5901	5247	5093
Y force	1511	1536	1547
Z force	1856	1896	1693
X moment	11921	11616	12258
Y moment	98659	96005	97856
Z moment	107908	101156	100693
Main shaft-bedplate link			
Main bearing 1 X force	5710	5088	4930
Main bearing 1 Y force	82819	77532	77058
Main bearing 1 Z force	74800	72577	74055
Main bearing 2 Y force	73732	68910	68329
Main bearing 2 Z force	65892	63771	64961
Main shaft-gear connection			
Y Force	8920	8446	8427
Z Force	8802	8627	8794
X Moment	5722	6159	6885
Y Moment	7233	7121	7245
Z Moment	7107	6706	6669
Planet Carrier Bearings			
Stage 1 Rotor side X force	309	265	230
Stage 1 Rotor side Y force	594	595	572
Stage 1 Generator side X force	7519	7039	6994
Stage 1 Generator side Y force	7897	7842	7967
Stage 2 Rotor side X force	1923	1897	1935
Stage 2 Rotor side Y force	1647	1492	1528
Stage 2 Generator side Y force	911	825	846
Stage 2 Generator side Z force	826	891	999

Table 5.11: Ratio of damage equivalent load results fifteen degree GFRP and fifteen degree CFRP configurations to zero degree GFRP configuration

Monitor Point	**GFRP** 15 degree spar cap	**CFRP** 15 degree spar cap
Blade root		
Leadwise moment	1.01	0.85
Flapwise moment	0.91	0.90
Torsional moment	1.02	0.90
Bedplate-tower link		
X force	0.89	0.86
Y force	1.02	1.02
Z force	1.02	0.91
X moment	0.97	1.03
Y moment	0.97	0.99
Z moment	0.94	0.93
Main shaft-bedplate link		
Main bearing 1 X force	0.89	0.86
Main bearing 1 Y force	0.94	0.93
Main bearing 1 Z force	0.97	0.99
Main bearing 2 Y force	0.93	0.93
Main bearing 2 Z force	0.97	0.99
Main shaft-gear connection		
Y Force	0.95	0.94
Z Force	0.98	1.00
X Moment	1.08	1.20
Y Moment	0.98	1.00
Z Moment	0.94	0.94
Planet Carrier Bearings		
Stage 1 Rotor side X force	0.86	0.74
Stage 1 Rotor side Y force	1.00	0.96
Stage 1 Generator side X force	0.94	0.93
Stage 1 Generator side Y force	0.99	1.01
Stage 2 Rotor side X force	0.99	1.01
Stage 2 Rotor side Y force	0.91	0.93
Stage 2 Generator side Y force	0.91	0.93
Stage 2 Generator side Z force	1.08	1.21

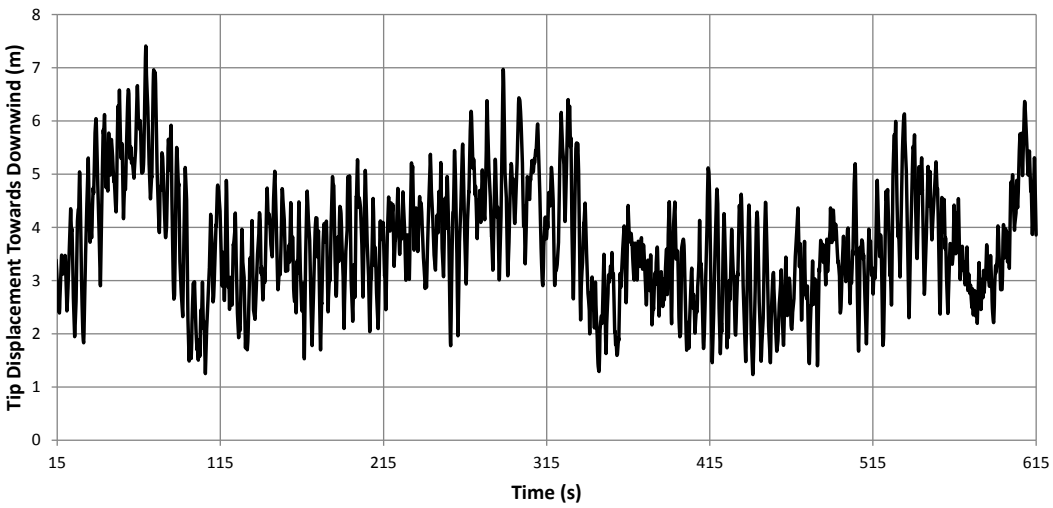

Figure 5.22: Blade tip displacement of CFRP spar cap configuration

5.2.3 Results for Wind Turbine System with Mixed 0 Degree and 15 Degree Off-Axis GFRP Spar cap Plies

To investigate possible ways of reducing the damage equivalent torque entering into the gearbox, a study is conducted on the sensitivity of the flapwise stiffness and the associated bending-twisting coupling and the leadwise bending stiffness on the damage equivalent loads for blades with GFRP spar caps without increasing the weights of the blades. For this purpose, two new blades are designed. In the first blade, certain number of 15^0 spar cap plies are converted into 0^0 such that flapwise stiffness of the blade sections in the outboard 30 m of the blade increased approximately by %12, and bending-twisting coupling stiffness coefficients decreased by $\%25 - \%38$. In the second blade, 15^0 to 0^0 conversion is made such that flapwise stiffness of the blade sections in the outboard 30 m of the blade increased approximately by %18, and bending-twisting coupling stiffness coefficients decreased by $\%38 - \%50$. In both cases, leadwise stiffness of the blades slightly increases due to the increase of the flapwise stiffness. Table 5.12 gives the comparison of the ratio of the damage equivalent loads in the wind turbine with blades having 15^0 spar cap plies to the damage equivalent loads in the turbine with the baseline blade. With the modifications in the outboard sections of the blade, it has been possible to reduce the damage equivalent torque enter-

ing into the gearbox at the cost of lower reductions in the damage equivalent loads at other connection points in the wind turbine system. Preliminary study showed that with careful adjustment of the blade stiffness, reductions in damage equivalent loads in the connection points of the whole wind turbine system, not just in the blades, can be possible. Again, the time at level counting of the X moment load at gear box main shaft link node should be performed for more reliable comparison.

Figure 5.23 and Figure 5.24 show the tip displacements of the GFRP spar cap blades with %12 and %18, respectively. The maximum tip displacements of the blades are 7.51 meters for GFRP spar cap blades with %12 and 7.41 meters for GFRP spar cap blades with %18. There are small improvements in maximum tip displacements compared to zero degree GFRP blade.

Table 5.12: Comparison of the ratio of damage equivalent loads of GFRP blades with 15^0 spar cap ply

Ratio of DE loads for turbine with GFRP blades (blade with 15^0 spar cap/blade with 0^0 spar cap)			
Monitor Point	Original 15^0 GF blade	Flapwise stiffness increased by %12	Flapwise stiffness increased by %18
Blade root			
Leadwise moment	1.01	1.01	1.00
Flapwise moment	0.91	0.94	0.95
Torsional moment	1.02	1.01	1.00
Main Bearing-1			
x-force	0.89	0.92	0.94
y-force	0.94	0.96	0.97
z-force	0.97	0.98	0.98
Gearbox connection			
y-force	0.95	0.97	0.98
z-force	0.98	0.98	0.99
x-moment	1.08	1.05	1.03
y-moment	0.98	0.99	0.99
z-moment	0.94	0.97	0.98

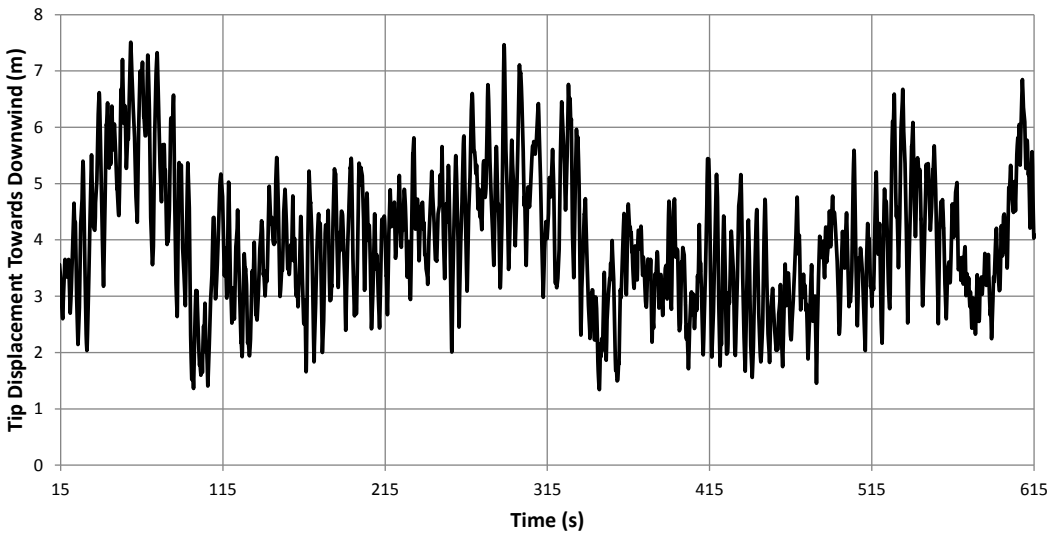

Figure 5.23: Blade tip displacement of GFRP spar cap %12 configuration

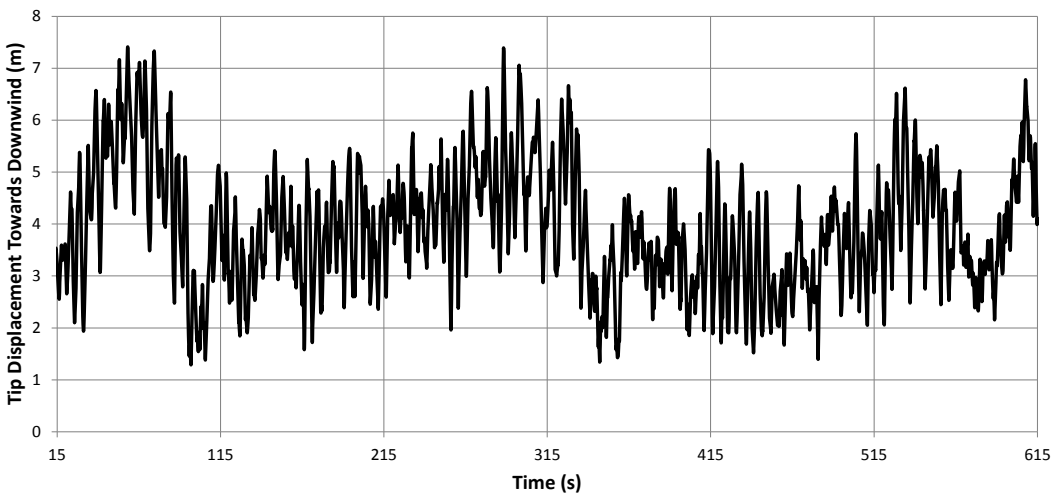

Figure 5.24: Blade tip displacement of GFRP spar cap %18 configuration

5.2.4 Results for Wind Turbine System with Stiff CFRP Blades

The CFRP material is lighter than the GFRP material and this allows to make stiffer blades without adding extra weight to the blade structure. Therefore, to investigate the bending twisting coupling effectiveness of a blade that has almost same flapwise stiffness value with the original zero degree GFRP blade, a new blade with CFRP middle spar cap at tip region is designed. The new

CFRP blade has similar flapwise and edgewise stiffness values as zero GFRP blade however it is more rigid in torsion degree of freedom about %7 - %17 than original GFRP blade. On the other hand, the coupling terms of the new blade is about 100,000 times larger than the original blade. It is a very useful comparison since the main difference between the new and original blade is the coupling term values between bend twist coupling.

Figure 5.25 shows the tip displacement of the new CFRP blade. The maximum tip displacement is decreased more than 1 meter compared to zero GFRP blade and this is a very import improvement.

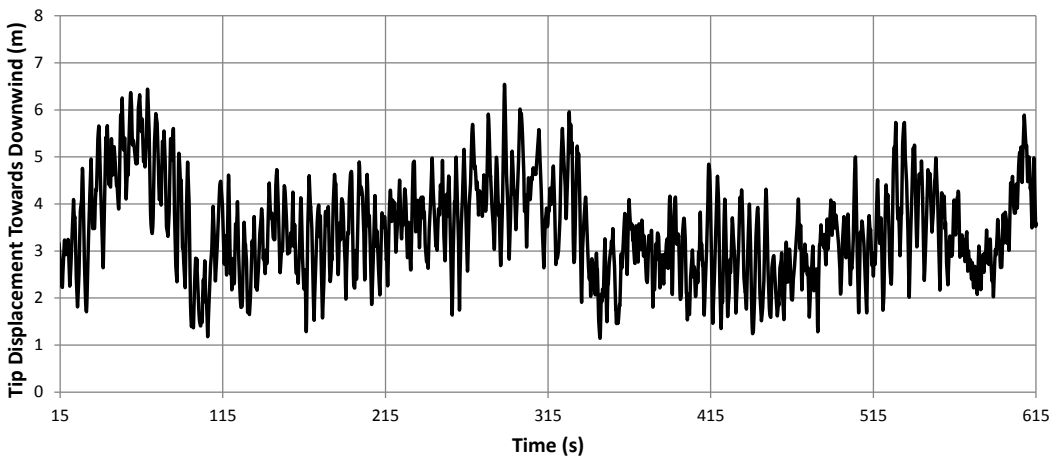

Figure 5.25: Blade tip displacement of stiff CFRP spar cap configuration

Table 5.13 compares the damage equivalent loads calculated at the monitor points in the wind turbine system having blades with 15 degree GFRP and CFRP spar cap plies. Effectiveness of the high coupling terms is clearly seen in the table. Since the main loads on the wind turbine system is coming from the blades it is vital to obtain load alleviation at blade root and the effect of the load alleviation at blade root results with load alleviation at other components of the wind turbine system.

Table 5.13: Comparison of the ratio of damage equivalent loads of GFRP blades with 15^0 spar cap ply

Ratio of DE loads for turbine with GFRP and CFRP blade (blade with 15^0 spar cap/blade with 0^0 spar cap)		
Monitor Point	Original 15^0 GF blade	Flapwise stiffness increased CF blade
Blade root		
Leadwise moment	1.01	0.88
Flapwise moment	0.91	0.91
Torsional moment	1.02	0.92
Main Bearing-1		
x-force	0.89	0.85
y-force	0.94	0.96
z-force	0.97	0.99
Gearbox connection		
y-force	0.95	0.98
z-force	0.98	1.00
x-moment	1.08	1.12
y-moment	0.98	1.00
z-moment	0.94	0.97

CHAPTER 6

CONCLUSION

The demand for higher energy production at lower cost from renewable energy sources has triggered engineering efforts to design bigger wind turbine systems with blades approaching to the border of 100 m. To meet the challenges of future wind turbine systems that will operate in on and off shore sites, any design effort geared towards increasing the fatigue life of the wind turbine components should be exploited. Bending-twisting coupling induced in the wind turbine blades is one of the passive control mechanisms that can be exploited in achieving load alleviation. This thesis presents a study on the effect of off-axis ply placement in the spar caps of the wind turbine blade on the damage equivalent loads in the wind turbine system. Bending-twisting coupling, which is introduced through the placement of off-axis plies in the spar caps of the wind turbine blade, is exploited for load alleviation in the turbine system. Fatigue damage equivalent load is used as the metric to assess the effect of off-axis ply placement in the spar caps of the turbine blade on the load alleviation in the wind turbine system. For the purposes of the study, three dimensional design of the blade of NREL's 5 MW [27] reference turbine is performed following an inverse design process. Dynamic superelement of the wind turbine blade is generated and introduced into the flexible multi-body model of the generic 5 MW wind turbine model created in Samcef Wind Turbine. Multi-body dynamic simulations of the wind turbine system are performed for the power production load case with the constant wind the normal turbulence model as the external wind loadings. For the load case involving the normal turbulence model, transient aeroelastic analyses are performed for 600 seconds as specified by the IEC-61400-1. Time history results

of multi-body simulations are used to calculate damage equivalent loads at the selected monitor points in the turbine system, and the effect of off-axis ply placement in the spar caps of the blades on the load alleviation in the wind turbine system is investigated. It should be noted that in the present study, since superelement of the blade is used in the multi-body model of the wind turbine system, geometric nonlinearity associated with the large deformation of the blade with respect to the blade fixed frame is not taken into account. However, for the purposes of comparing the effect of different off-axis spar cap fiber angle configurations on the load alleviation in the wind turbine system, it is assessed that the use of superelement blades in the multi-body simulation of the wind turbine can provide sufficient information on the effectiveness of off-axis spar cap plies on the load alleviation in the wind turbine system. This study can further be improved with the use of geometrically nonlinear beam elements with fully populated stiffness matrix, including the coupling stiffness, in the multi-body model of the wind turbine system.

Damage equivalent loads are calculated at the critical monitor points selected in the multi-body model of the wind turbine system. Results show that in the overall, with the use of off-axis plies in the main spar caps of the blade, damage equivalent loads associated with the critical force or moment components can be reduced in the wind turbine. In the thesis, the effect of using GFRP and CFRP spar cap plies in off-axis configuration is also compared. It is seen that with the introduction of off-axis CFRP spar cap plies in the blades, higher reductions in the damage equivalent loads can be achieved in the selected monitor points in the wind turbine system. Results presented in the thesis showed that the use of GFRP and CFRP both have certain advantages and disadvantages in reducing damage equivalent loads in the complete wind turbine system. CFRP material is seen to be more effective in reducing the damage equivalent moments at the blade root. However, for damage equivalent drive train loads, no definite advantage of CFRP usage over GFRP usage in the main spar caps is observed. In the current study, it has not been possible to reduce the damage equivalent X moment acting on the shaft, which is essentially the useful rotor torque flowing into the gearbox. Therefore, damage equivalent gear contact forces also increase in the gears with the introduction of off-axis spar cap plies in the blades. However, by

proper design modifications, it may be possible to reduce the damage equivalent main shaft torque to the level of the damage equivalent main shaft torque of the wind turbine that has GFRP baseline blades. On the other hand to obtain a clear view about the effect of bending twisting coupling on the gear box loads, time at level counting analyses should be performed for main shaft torque and gear box loads. It should be noted that this thesis deals with a single angle for the placement of off-axis spar cap plies, and the modification is done in the last 30 meter of the blade. However, there are many design changes that can be performed to induce bending-twisting coupling, each one then has to be investigated in terms of their impact of the damage equivalent loads in the wind turbine system. Some of these design modifications are listed below:

- To determine the optimum spar cap region, both chordwise and spanwise, which will cause maximum load reduction without significantly degrading the performance of the wind turbine structurally and in terms of energy production.

- To investigate the effect of different off-axis angles on the load alleviation and on the overall performance of the wind turbine system. Starting from low angles, different ply orientations can be tried, and best off-axis ply angle can be determined in terms of reducing damage equivalent loads including the damage equivalent main shaft torque.

- The effect of increasing and decreasing the number off-axis spar cap plies on the damage equivalent loads can be investigated.

- The effect leading and trailing edge spar cap plies can also be investigated in terms of their effect on the damage equivalent loads.

Present study shows the potential of achieving load reduction in the wind turbine system, under realistic turbulent wind conditions, by exploiting bending-twisting coupling induced in the turbine blades through the introduction of off-axis spar cap plies. It should be noted that fatigue damage equivalent load is a sign of the degradation of the elements of the sub-structures of the wind turbine system due to material fatigue incurred under cyclic loading, and reduction in the damage

equivalent loads implies increased fatigue life of the structural elements with direct effect on the life time cost of the wind turbine system.
In the future, the following studies need be performed to substantiate the effect of bending-twisting coupling on the load alleviation in wind turbine systems, and on the structural and the energy production performance of wind turbine systems.

- To ascertain the effect of off-axis plies on the degradation of the structural performance of the blades by performing strength and buckling checks of the blades with off-axis spar cap plies. Implementation of off-axis spar caps has to be united with the design of the blade from the very beginning.

- For the bend-twist coupled blade configurations for which substantial reductions in the damage equivalent loads in the complete wind turbine system has been achieved, the differences between the bend-twist coupled blades and the baseline blade in terms of strength, deformation, dynamic characteristics, weight and cost may be quantified. Strength checks of the bend-twist coupled blades and the baseline full GFRP blades may be made by calculating the maximum stress exposure ratio of the Puck failure criteria in sections of the blade at the peak loads.

- To perform technical and economical trade-off studies with blades having full carbon-epoxy, full glass-epoxy (E and S Glass) and hybrid carbon-glass-epoxy off-axis spar cap plies. The effect of using hybrid GFRP/CFRP plies in the main spar caps on the damage equivalent loads in the complete wind turbine system may be investigated in more detail by generating other bend-twist coupled hybrid GRFP-CFRP blade designs. It is considered that with proper adjustment of the sectional stiffness of the blade, higher reductions in damage equivalent loads in the critical connection points of the whole wind turbine system may be achieved.

- To perform similar analysis using geometrically non-linear coupled beam models for the blades in the wind turbine system, and conduct comparative study with superelement blades which essentially behave linearly with respect to the local frame fixed to the blade. For this purpose, an almost

same wind turbine model may be set up in PHATAS and multi-body simulation of the wind turbine system performed by SWT may be replicated by PHATAS utilizing non-linear bend-twist coupled beam blades in the multi body model of the wind turbine system. PHATAS results will allow us to infer conclusions on the effect of geometric non-linearity of the blades on the damage equivalent loads in the wind turbine system. Comparisons may be made with the results obtained by SWT utilizing reduced order superelement blades which essentially behave linearly with respect to the local frame fixed to the blade.

- Different trials may be made on the use of off-axis spar cap plies in different span-wise zones in the main spar caps of the blade. Figure 5.2 shows that lift in the in-board sections of the blade increases due to the decrease in the pitch angle managed by the controller. Controller induced motions induce fluctuations in the loads resulting in increases in damage equivalent loads. In the in-board sections of the blade, if the spar cap plies are placed such that bending-twisting coupling induced causes decrease in the pitch angle, then lift increase may be achieved in the in-board sections of the blade. Thus, pitch controller induced fluctuations may be reduced resulting in decreases in the damage equivalent loads.

- To develop controllers which are actually optimized for the wind turbine systems that have bend-twist coupled blades. It should be noted that in the present study, a standard controller is used to drive the wind turbine system, and minimum intervention is made to the controller. However, controller itself can also be optimized to yield reduction in damage equivalent loads in the overall wind turbine system.

REFERENCES

[1] *Samcef Field User Manual*, last accessed on April 2013.

[2] *Samcef Wind Turbines (SWT) User Help V.3.3 LMS Inc.(2013)*, last acessed on April 2013.

[3] *SAMCEF-Mecano User Manual Version 14.1. http://www.samtech.com Belgium*, last accessed on April 2013.

[4] T. D. Ashwill. Passive load control for large wind turbines. *AIAA, April*, 2010.

[5] S. Aziz, J. Gale, A. Ebrahimpour, and M. P. Schoen. Passive control of a wind turbine blade using composite material. In *ASME 2011 International Mechanical Engineering Congress and Exposition*, pages 467–476. American Society of Mechanical Engineers, 2011.

[6] F. Beer, E. Johnston, and J. DeWolf. Mechanics of materials, 2002.

[7] V. Berdichevskii. Variational asymptotic method for constructing a shell theory. *Prikladnaia Matematika i Mekhanika*, 43:664–687, 1979.

[8] R. Binz, R. Sedano, D. Furey, and D. Mullen. Practicing risk-aware electricity regulation: What every state regulator needs to know. Technical report, Ceres , Boston, MA (US), 2012.

[9] G. S. Bir. Computerized method for preliminary structural design of composite wind turbine blades. *Journal of solar energy engineering*, 123(4):372–381, 2001.

[10] T. Burton, N. Jenkins, D. Sharpe, and E. Bossanyi. *Wind energy handbook*. John Wiley & Sons, 2011.

[11] M. Capellaro. Design limits of bend twist coupled wind turbine blades. In *53rd AIAA/ASME/ASCE/AHS/ASC Structures, Structural Dynamics and Materials Conference 20th AIAA/ASME/AHS Adaptive Structures Conference 14th AIAA*, 2012.

[12] C. E. Cesnik and D. H. Hodges. Stiffness constants for initially twisted and curved composite beams. *ASME AEROSP DIV PUBL AD, ASME, NEW YORK, NY(USA), 1992,*, 30:1–8, 1992.

[13] C. E. Cesnik and D. H. Hodges. Variational-asymptotical analysis of initially curved and twisted composite beams. *Applied Mechanics Reviews*, 46(11S):S211–S220, 1993.

[14] H. Chen and W. Yu. Manual of prevabs. *Utah State University*, last accessed on February 2013.

[15] N. Cosack. *Fatigue load monitoring with standard wind turbine signals.* PhD thesis, Universität Stuttgart, 2010.

[16] W. De Goeij, M. Van Tooren, and A. Beukers. Implementation of bending-torsion coupling in the design of a wind-turbine rotor-blade. *Applied Energy*, 63(3):191–207, 1999.

[17] M. Drela and H. Youngren. Xfoil 6.94 user guide. *Massachusetts Institute of Technology, Cambridge, MA*, 2001.

[18] J. W. Eaton, D. Bateman, and S. Hauberg. *Gnu octave.* Free Software Foundation, 1997.

[19] N. Fichaux, J. Beurskens, P. H. Jensen, J. Wilkes, S. Frandsen, J. Sorensen, P. Eecen, C. Malamatenios, J. Gomez, J. Hemmelmann, et al. Upwind: Design limits and solutions for very large wind turbines. *Sixth Framework Programme*, 2011.

[20] M. H. Hansen, M. Gaunaa, and H. Aagaard Madsen. *A Beddoes-Leishman type dynamic stall model in state-space and indicial formulations.* 2004.

[21] A. Heege, J. Hemmelmann, L. Bastard, J. Sanchez, L. Lens, and M. Omiciuolo. Matching experimental and numerical data of dynamic wind turbine loads by modelling of defects. *SAMTECH, EWEC*, 2009.

[22] J. C. Ho, W. Yu, and D. H. Hodges. Energy transformation to generalized timoshenko form by the variational asymptotic beam sectional analysis. In *Proceedings of the 51st structures, structural dynamics and materials conference, April 12–15, Orlando, Florida*, 2010.

[23] D. H. Hodges, A. R. Atilgan, C. E. Cesnik, and M. V. Fulton. On a simplified strain energy function for geometrically nonlinear behaviour of anisotropic beams. *Composites Engineering*, 2(5):513–526, 1992.

[24] IEC61400-1ThirdEdition2005. *Wind turbines – Part 1: Design requirements.* International Electrotechnical Commission Switzerland, 2005.

[25] B. J. Jonkman. *TurbSim user's guide: Version 1.50.* National Renewable Energy Laboratory Colorado, 2009.

[26] J. M. Jonkman and M. L. Buhl Jr. Fast user's guide. *Golden, CO: National Renewable Energy Laboratory*, 2005.

[27] J. M. Jonkman, S. Butterfield, W. Musial, and G. Scott. *Definition of a 5-MW reference wind turbine for offshore system development*. National Renewable Energy Laboratory Golden, CO, 2009.

[28] D. C. Kammer and M. Baker. Comparison of the craig-bampton and residual flexibility methods of substructure representation. *Journal of Aircraft*, 24(4):262–267, 1987.

[29] N. Karaolis, P. Mussgrove, and G. Jeronimidis. Active and passive aeroelastic power control using asymmetric fibre reinforced laminates for wind turbine blades. In *Proceedings of the 10th British Wind Energy Conference, London*, 1988.

[30] T. Kim, A. M. Hansen, and K. Branner. Development of an anisotropic beam finite element for composite wind turbine blades in multibody system. *Renewable Energy*, 59:172–183, 2013.

[31] H. Kooijman. *Bending-torsion coupling of a wind turbine rotor blade*. Netherlands Energy Research Foundation ECN, 1996.

[32] R. K. Kovvali and D. H. Hodges. Verification of the variational-asymptotic sectional analysis for initially curved and twisted beams. *Journal of Aircraft*, 49(3):861–869, 2012.

[33] L. I. Lago, F. L. Ponta, and A. D. Otero. Analysis of alternative adaptive geometrical configurations for the nrel-5 mw wind turbine blade. *Renewable Energy*, 59:13–22, 2013.

[34] H.-J. Lin and W.-M. Lai. A study of elastic coupling to the wind turbine blade by combined analytical and finite element beam model. *Journal of composite materials*, 44(23):2643–2665, 2010.

[35] G. Lloyd. Guideline for the certification of offshore wind turbines, 2005.

[36] D. Lobitz, P. Veers, P. Migliore, et al. Enhanced performance of hawts using adaptive blades. *Wind energy*, 96:41–45, 1996.

[37] D. W. Lobitz and P. S. Veers. Load mitigation with bending/twist-coupled blades on rotors using modern control strategies. *Wind Energy*, 6(2):105–117, 2003.

[38] D. W. Lobitz, P. S. Veers, and D. J. Laino. Performance of twist-coupled blades on variable speed rotors. Technical report, Sandia National Labs., Albuquerque, NM (US); Sandia National Labs., Livermore, CA (US), 1999.

[39] J. Locke, U. Valencia, and K. Ishikawa. Design studies for twist-coupled wind turbine blades. In *ASME 2003 Wind Energy Symposium*, pages 324–331. American Society of Mechanical Engineers, 2003.

[40] M. Luczak, S. Manzato, B. Peeters, K. Branner, P. Berring, and M. Kahsin. Dynamic investigation of twist-bend coupling in a wind turbine blade. *Journal of Theoretical and Applied Mechanics*, 49:765–789, 2011.

[41] G. Lutz and V. K.-u. Getriebebau. The puck theory of failure in laminates in the context of the new guideline vdi 2014 part 3. In *Conference on damage in composite materials*, 2006.

[42] B. P. McNiff and R. L. Errichello. New guidelines promise reliable wind-turbine gearboxes: What they mandate. *Motion System Design*, 1997.

[43] T. Philippidis, A. Vassilopoulos, K. Katopis, and S. Voutsinas. Thin/probream: A software for fatigue design and analysis of composite rotor blades. *WIND ENGINEERING-LONDON-*, 20:349–362, 1996.

[44] A. Puck, J. Kopp, and M. Knops. Guidelines for the determination of the parameters in puck's action plane strength criterion. *Composites Science and Technology*, 62(3):371–378, 2002.

[45] S. Samtech. Samcef user manuals, 1999.

[46] G. van Kuik. Ple1. 2 are wind turbines growing too fast? In *EWEC-CONFERENCE-*, pages 69–72, 2001.

[47] J. Young. Primer on the craig-bampton method. *Finite Element Modeling Continuous Improvement, NASA*, 2000.

[48] W. Yu. Vabs manual for users. *Utah State University: Logan, Utah*, last accessed on February 2013.

[49] W. Yu, V. V. Volovoi, D. H. Hodges, and X. Hong. Validation of the variational asymptotic beam sectional analysis. *AIAA journal*, 40(10):2105–2112, 2002.

[50] X. Y. Zhou, L. Q. An, and Z. Q. Wang. Twist-bend coupling analysis for 5mw wind turbine blades. *Applied Mechanics and Materials*, 152:703–708, 2012.

APPENDIX A

TRANSITION AIRFOILS

There are two transition airfoils which are created by XFoil [17] computer program. XFoil is able to generate a new airfoil with desired thichness ratio by using two airfoil data. In initial phase of the inverse design process two transition airfoils are generated by circle and first airfoil of the blade (DU40 A17). First transition section has %95 and second one has %72 thickness ratio. First transition airfoil coordinates are given in Table A.1 and seond transition airfoil coordinates are given in Table A.2.

Table A.1: First transition airfoil coordinates

x coordinate	y coordinate	x coordinate	y coordinate
1.000000	0.002105	0.000020	0.006256
0.989504	0.024643	0.000059	-0.003920
0.975897	0.050581	0.000467	-0.014083
0.963219	0.072167	0.001239	-0.024240
0.950788	0.091410	0.002373	-0.034399
0.938250	0.109231	0.003871	-0.044566
0.925411	0.126120	0.005736	-0.054748
0.912200	0.142297	0.007973	-0.064948
0.898605	0.157847	0.010591	-0.075171
0.884615	0.172821	0.013601	-0.085421
0.870216	0.187258	0.017017	-0.095699
0.855385	0.201194	0.020857	-0.106006
0.840145	0.214633	0.025141	-0.116344
0.824528	0.227542	0.029893	-0.126711
0.808501	0.239934	0.035132	-0.137115
0.792073	0.251830	0.040871	-0.147564
0.775299	0.263203	0.047117	-0.158055
0.758227	0.274006	0.053863	-0.168574
0.740821	0.284238	0.061101	-0.179084
0.723104	0.293958	0.068829	-0.189546
0.705238	0.303026	0.077054	-0.199931
0.687067	0.311526	0.085790	-0.210228
0.668782	0.319434	0.095046	-0.220427
0.650405	0.326682	0.104816	-0.230508
0.631894	0.333293	0.115087	-0.240437
0.613280	0.339298	0.125839	-0.250176
0.594658	0.344675	0.137061	-0.259688
0.576024	0.349399	0.148755	-0.268945
0.557412	0.353518	0.160922	-0.277936
0.520335	0.359802	0.186577	-0.295031
0.501871	0.362022	0.199997	-0.303067
0.483491	0.363634	0.213772	-0.310708
0.465217	0.364641	0.227921	-0.317942
0.447070	0.365051	0.242417	-0.324793
0.429063	0.364884	0.257132	-0.331183
0.411275	0.364143	0.272140	-0.337077
0.393642	0.362800	0.287410	-0.342539
0.376207	0.360928	0.302828	-0.347507
0.359016	0.358499	0.318395	-0.351946
0.342051	0.355541	0.334120	-0.355857
0.325376	0.352090	0.349990	-0.359250
0.309032	0.348140	0.365960	-0.362127
0.293013	0.343682	0.381996	-0.364457
0.277282	0.338733	0.398137	-0.366232
0.261871	0.333362	0.414347	-0.367488
0.246901	0.327584	0.430604	-0.368164
0.232287	0.321347	0.446979	-0.368283
0.218044	0.314747	0.463430	-0.367851
0.204267	0.307801	0.479967	-0.366850
0.190929	0.300495	0.496592	-0.365277
0.178023	0.292853	0.513306	-0.363125
0.165562	0.284903	0.530107	-0.360383
0.153557	0.276670	0.547001	-0.357051
0.142019	0.268170	0.563945	-0.353097
0.130949	0.259415	0.581046	-0.348480
0.120335	0.250413	0.598258	-0.343233
0.110174	0.241191	0.615609	-0.337292
0.100475	0.231780	0.633125	-0.330670
0.091251	0.222203	0.650737	-0.323376
0.082500	0.212475	0.668416	-0.315366
0.074220	0.202610	0.686211	-0.306587
0.066409	0.192624	0.704149	-0.297064
0.059065	0.182533	0.722042	-0.286832
0.052184	0.172354	0.740047	-0.275759
0.045761	0.162098	0.758012	-0.263977
0.039790	0.151772	0.775912	-0.251396
0.034263	0.141384	0.793798	-0.237984
0.029175	0.130943	0.811623	-0.223761
0.020296	0.109950	0.846981	-0.192759
0.016495	0.099436	0.864568	-0.175882
0.013110	0.088934	0.882043	-0.158081
0.010131	0.078458	0.899428	-0.139289
0.007550	0.068018	0.916716	-0.119464
0.005357	0.057620	0.933851	-0.098590
0.003547	0.047265	0.950861	-0.076454
0.002111	0.036955	0.968110	-0.052303
0.001047	0.026687	0.986391	-0.024514
0.000350	0.016456	1.000000	-0.002105

Table A.2: Second transition airfoil coordinates

x coordinate	y coordinate	x coordinate	y coordinate
1.000000	0.002778	0.000131	0.010916
0.987299	0.020759	-0.000015	0.002561
0.970016	0.043503	0.000135	-0.005778
0.953733	0.063340	0.000579	-0.014104
0.937822	0.081411	0.001313	-0.022424
0.921907	0.098338	0.002336	-0.030743
0.905794	0.114453	0.003647	-0.039064
0.889432	0.129883	0.005248	-0.047392
0.872815	0.144670	0.007144	-0.055730
0.855927	0.158849	0.009340	-0.064080
0.838738	0.172461	0.011843	-0.072446
0.821268	0.185515	0.014663	-0.080830
0.803543	0.197984	0.017814	-0.089234
0.785525	0.209900	0.021308	-0.097658
0.767247	0.221271	0.025165	-0.106105
0.748773	0.232061	0.029406	-0.114573
0.730116	0.242243	0.034055	-0.123067
0.711230	0.251881	0.039127	-0.131600
0.692311	0.260880	0.044638	-0.140181
0.673212	0.269288	0.050594	-0.148812
0.654112	0.277097	0.056993	-0.157484
0.635037	0.284252	0.063827	-0.166171
0.615952	0.290781	0.071094	-0.174836
0.596903	0.296707	0.078802	-0.183454
0.577969	0.302006	0.086972	-0.192013
0.559114	0.306689	0.095620	-0.200515
0.521850	0.314217	0.114360	-0.217295
0.503391	0.317092	0.124428	-0.225514
0.485071	0.319389	0.134948	-0.233577
0.466909	0.321118	0.145918	-0.241455
0.448914	0.322288	0.157340	-0.249128
0.431097	0.322916	0.169208	-0.256580
0.413515	0.323020	0.181502	-0.263789
0.396151	0.322568	0.194189	-0.270729
0.378994	0.321623	0.207236	-0.277362
0.362112	0.320176	0.220615	-0.283652
0.329163	0.315859	0.248360	-0.295173
0.313187	0.313028	0.262586	-0.300350
0.297556	0.309743	0.277065	-0.305091
0.282241	0.306022	0.291761	-0.309437
0.267257	0.301919	0.306574	-0.313342
0.252708	0.297462	0.321497	-0.316777
0.238546	0.292609	0.336528	-0.319738
0.224757	0.287429	0.351653	-0.322231
0.211422	0.281952	0.366837	-0.324255
0.198528	0.276170	0.382056	-0.325789
0.186065	0.270101	0.397345	-0.326822
0.174036	0.263767	0.412689	-0.327384
0.162446	0.257189	0.428064	-0.327431
0.151297	0.250382	0.443543	-0.326972
0.140586	0.243359	0.459101	-0.326012
0.130306	0.236129	0.474755	-0.324533
0.120448	0.228710	0.490524	-0.322529
0.111009	0.221125	0.506416	-0.319993
0.101995	0.213393	0.522440	-0.316908
0.093408	0.205532	0.538620	-0.313264
0.085244	0.197553	0.554935	-0.309034
0.077498	0.189468	0.571489	-0.304159
0.070164	0.181286	0.588284	-0.298654
0.063237	0.173020	0.605369	-0.292450
0.056712	0.164680	0.622799	-0.285536
0.050580	0.156276	0.640538	-0.277906
0.044835	0.147813	0.658585	-0.269497
0.039469	0.139298	0.677028	-0.260233
0.034475	0.130734	0.695874	-0.250136
0.029848	0.122130	0.715049	-0.239120
0.025582	0.113492	0.734716	-0.227131
0.021671	0.104832	0.754734	-0.214152
0.018111	0.096166	0.775284	-0.200013
0.014892	0.087507	0.796441	-0.184624
0.012007	0.078868	0.818313	-0.167814
0.009448	0.070255	0.841218	-0.149256
0.007207	0.061673	0.865465	-0.128632
0.005278	0.053126	0.891532	-0.105459
0.003654	0.044616	0.919868	-0.079260
0.002331	0.036142	0.951066	-0.049713
0.001304	0.027702	0.981819	-0.020298
0.000571	0.019295	1.000000	-0.002778

APPENDIX B

DAMAGE EQUIVALENT LOAD

The allowable number of cycles N for a straight S-N line on log-log scale is given by:

$$N = k \cdot S_r^{-m} \tag{B.1}$$

In which S_r is the range of a load cycle and $-1/m$ is the slope of the S-N line on log-log scale. The damage caused by a load spectrum of n cycles with ranges $S_{r,i}$:

$$D = \sum_{i=1}^{n} \frac{1}{k \cdot S_{r,i}^{-m}} \tag{B.2}$$

The damage caused by N_{eq} (constant amplitude) cycles with range $S_{r,eq}$ has to equal the damage of the above load spectrum:

$$\frac{N_{eq}}{k \cdot S_{r,eq}^{-m}} = \sum_{i=1}^{n} \frac{1}{k \cdot S_{r,i}^{-m}} \tag{B.3}$$

$$S_{r,eq} = \left(\sum_{i=1}^{n} \frac{S_{r,i}^{m}}{N_{eq}} \right)^{1/m} \tag{B.4}$$

APPENDIX C

SAMCEF WIND TURBINE VERIFICATION

The verification is performed in two ways; one is aerodynamic verification and the other one is the structural verification. In the aerodynamic verification, the aerodynamic results of Samcef Wind Turbine and Bladed (an aeroleastic code of GL) are compared for same turbine model. Both of the code use BEM solver. For structural verification, a 6 meters cantilever beam tip deflection calculated by hand calculation and Samcef Wind Turbine are compared. At the tip of the beam, a concentrated 1 MN force is applied and the rigidity (EI) of the beam is 50e9 Nm^2. The hand calculation and the code give the same result, 1.44 mm tip deflection. The below equation is used for hand calculation. The results of the aerodynamic analysis is given below.

Table C.1: Integrated rotor torque [N.m], power [W] and power coefficient [-] in both models

	Bladed	**SWT**
Torque [N.m]	2.45E+06	2.45E+06
Power [W]	3.85E+06	3.85E+06
Power coefficient [-]	0.156	0.156

$$\delta_{tip,cantilever} = \frac{PL^3}{3EI} \tag{C.1}$$